

LEWIS GRANT  
N-32-CR  
147

P132



# Constitutive Parameter De-embedding Using Inhomogeneously-Filled Rectangular Waveguides with Longitudinal Section Modes

A. Park and A. Dominek

The Ohio State University  
**ElectroScience Laboratory**

Department of Electrical Engineering  
Columbus, Ohio 43212

Final Report 721837-2  
Grant NAG 3-1000  
October 1990

National Aeronautics and Space Administration  
Lewis Research Center  
21000 Brookpark Road  
Cleveland, Ohio 44135

(NASA-CR-187990) CONSTITUTIVE PARAMETER  
DE-EMBEDDING USING INHOMOGENEOUSLY-FILLED  
RECTANGULAR WAVEGUIDES WITH LONGITUDINAL  
SECTION MODES Final Report (Ohio State  
Univ.) 132 p

N91-18341

Unclas  
0000147

CSCL 20N G3/32

## NOTICES

When Government drawings, specifications, or other data are used for any purpose other than in connection with a definitely related Government procurement operation, the United States Government thereby incurs no responsibility nor any obligation whatsoever, and the fact that the Government may have formulated, furnished, or in any way supplied the said drawings, specifications, or other data, is not to be regarded by implication or otherwise as in any manner licensing the holder or any other person or corporation, or conveying any rights or permission to manufacture, use, or sell any patented invention that may in any way be related thereto.

<b>REPORT DOCUMENTATION PAGE</b>	<b>1. REPORT NO.</b>	<b>2.</b>	<b>3. Recipient's Accession No.</b>
<b>4. Title and Subtitle</b> Constitutive Parameter De-embedding Using Inhomogeneously-Filled Rectangular Waveguides with Longitudinal Section Modes			<b>5. Report Date</b> October 1990
<b>7. Author(s)</b> A. Park and A. Dominek			<b>6.</b>
<b>9. Performing Organization Name and Address</b> The Ohio State University ElectroScience Laboratory 1320 Kinnear Road Columbus, OH 43212			<b>8. Performing Org. Rept. No.</b> 721837-2
<b>13. Sponsoring Organization Name and Address</b> National Aeronautics and Space Administration Lewis Research Center 21000 Brookpark Road, Cleveland, OH 44135			<b>10. Project/Task/Work Unit No.</b>
			<b>11. Contract(C) or Grant(G) No.</b> (C) (G) NAG 3-1000
			<b>13. Report Type/Period Covered</b> Final Report
<b>15. Supplementary Notes</b>			<b>14.</b>
<b>16. Abstract (Limit: 200 words)</b>  The purpose of this report is to investigate constitutive parameter extraction from S parameter data using a rectangular waveguide whose cross section is partially filled with a material sample as opposed to being completely filled. One reason for studying a partially-filled geometry is to analyze the effect of air gaps between the sample and fixture for the extraction of constitutive parameters. Air gaps can occur in high temperature parameter measurements when the sample was prepared at room temperature. Single-port and two-port measurement approaches to parameter extraction are also discussed.			
<b>17. Document Analysis a. Descriptors</b> DIELECTRIC MEASUREMENT MOMENT METHOD b. Identifiers/Open-Ended Terms  c. COSATI Field/Group			
<b>18. Availability Statement</b> A. Approved for public release; Distribution is unlimited.		<b>19. Security Class (This Report)</b> Unclassified	<b>21. No. of Pages</b> 132
		<b>20. Security Class (This Page)</b> Unclassified	<b>22. Price</b>



# Contents

<b>List of Figures</b>	<b>v</b>
<b>1 Introduction</b>	<b>1</b>
<b>2 Material Parameter Extraction Using Waveguides</b>	<b>4</b>
<b>3 Partially-Filled Waveguides</b>	<b>17</b>
I Field Expansions—Geometry A . . . . .	20
II Field Expansions—Geometry B . . . . .	23
III Calculations . . . . .	24
III.1 Geometry A . . . . .	24
III.2 Geometry B . . . . .	34
<b>4 Parameter Extraction</b>	<b>44</b>
I Two-Port Approach . . . . .	59
II Single-Port Approach . . . . .	70
<b>5 Conclusions</b>	<b>86</b>
<b>A The Self-Consistent Technique</b>	<b>89</b>
I Two-Port Formulation . . . . .	90

II	Single-Port Formulation . . . . .	91
B	Scattering Matrix Formulation for Geometry A	95
C	Scattering Matrix Formulation for Geometry B	100
D	Determination of Gamma Constants	109
	Bibliography	120

# List of Figures

2.1	Normalized error for $\epsilon$ when $S_{11}$ has a position error of .001" (solid) and .003" (dashed). The sample parameters are $\epsilon_r = (4.0, -j.20)$ and $\mu_r = (1.2, -j.12)$ with $d = .3"$ . Coaxial airline fixture. . . . .	9
2.2	Normalized error for $\mu$ when $S_{11}$ has a position error of .001" (solid) and .003" (dashed). The sample parameters are $\epsilon_r = (4.0, -j.20)$ and $\mu_r = (1.2, -j.12)$ with $d = .3"$ . Coaxial airline fixture. . . . .	10
2.3	Normalized error for $\epsilon$ when $S_{11}$ has a position error of .001" (solid) and .003" (dashed). The sample parameters are $\epsilon_r = (4.0, -j.20)$ and $\mu_r = (1.2, -j.12)$ with $d = .3"$ . Rectangular waveguide fixture. . . . .	11
2.4	Normalized error for $\mu$ when $S_{11}$ has a position error of .001" (solid) and .003" (dashed). The sample parameters are $\epsilon_r = (4.0, -j.20)$ and $\mu_r = (1.2, -j.12)$ with $d = .3"$ . Rectangular waveguide fixture. . . . .	12
2.5	Normalized error for $\epsilon$ when $S_{11}$ has a sample length error of +.002" (solid) and -.002" (dashed). The sample parameters are $\epsilon_r = (4.0, -j.20)$ and $\mu_r = (1.2, -j.12)$ with assumed $d = .3"$ . Coaxial airline fixture. . . . .	13
2.6	Normalized error for $\mu$ when $S_{11}$ has a sample length error of +.002" (solid) and -.002" (dashed). The sample parameters are $\epsilon_r = (4.0, -j.20)$ and $\mu_r = (1.2, -j.12)$ with assumed $d = .3"$ . Coaxial airline fixture. . . . .	14

2.7	Normalized error for $\epsilon$ when $S_{11}$ has a sample length error of $+0.002''$ (solid) and $-0.002''$ (dashed). The sample parameters are $\epsilon_r = (4.0, -j.20)$ and $\mu_r = (1.2, -j.12)$ with assumed $d = .3''$ . Rectangular waveguide fixture. . . . .	15
2.8	Normalized error for $\mu$ when $S_{11}$ has a sample length error of $+0.002''$ (solid) and $-0.002''$ (dashed). The sample parameters are $\epsilon_r = (4.0, -j.20)$ and $\mu_r = (1.2, -j.12)$ with assumed $d = .3''$ . Rectangular waveguide fixture. . . . .	16
3.1	Partially-filled waveguide geometries. . . . .	18
3.2	Waveguide regions. . . . .	21
3.3	Calculated $S_{11}$ for $t = .2'', .5'', .7'',$ and $.9''$ in an X-band fixture ( $.4'' \times .9''$ ) when $\epsilon_r = (4.0, -j.20)$ , $\mu_r = (1.2, -j.12)$ and $d = .3''$ . Geometry A. . . . .	26
3.4	Calculated $S_{21}$ for $t = .2'', .5'', .7'',$ and $.9''$ in an X-band fixture ( $.4'' \times .9''$ ) when $\epsilon_r = (4.0, -j.20)$ , $\mu_r = (1.2, -j.12)$ and $d = .3''$ . Geometry A. . . . .	27
3.5	Calculated $S_{11}$ for $\epsilon_r = 2, 5, 8, 11,$ and $14$ in an X-band fixture ( $.4'' \times .9''$ ) when $\mu_r = (1., -j0.)$ , $t = .1''$ and $d = .3''$ . Geometry A. . . . .	28
3.6	Calculated $S_{21}$ for $\epsilon_r = 2, 5, 8, 11,$ and $14$ in an X-band fixture ( $.4'' \times .9''$ ) when $\mu_r = (1., -j0.)$ , $t = .1''$ and $d = .3''$ . Geometry A. . . . .	29
3.7	Normalized error in $\epsilon$ for an $.002''$ air gap along the short wall for a rectangular guide with $\epsilon_r = (4.0, -j.20)$ , $\mu_r = (1.2, -j.12)$ and $d = .156''$ . Geometry A but assumed completely filled. . . . .	30
3.8	Normalized error in $\mu$ for an $.002''$ air gap along the short wall for a rectangular guide with $\epsilon_r = (4.0, -j.20)$ , $\mu_r = (1.2, -j.12)$ and $d = .156''$ . Geometry A but assumed completely filled. . . . .	31
3.9	Normalized error in $\epsilon$ for an additional $.002''$ air gap along the short wall for a rectangular guide with $\epsilon_r = (4.0, -j.20)$ , $\mu_r = (1.2, -j.12)$ , $d = .156''$ and assumed $t = .490''$ . Geometry A. . . . .	32



3.10	Normalized error in $\mu$ for an additional .002" air gap along the short wall for a rectangular guide with $\epsilon_r = (4.0, -j.20)$ , $\mu_r = (1.2, -j.12)$ , $d = .156''$ and assumed $t = .490''$ . Geometry A. . . . .	33
3.11	Calculated $S_{11}$ for $t = .05'', .1'', .2'', .3''$ and $.4''$ in an X-band fixture (.4" $\times$ .9") when $\epsilon_r = (4.0, -j.20)$ , $\mu_r = (1.2, -j.12)$ and $d = .3''$ . Geometry B. . . . .	35
3.12	Calculated $S_{21}$ for $t = .05'', .1'', .2'', .3''$ and $.4''$ in an X-band fixture (.4" $\times$ .9") when $\epsilon_r = (4.0, -j.20)$ , $\mu_r = (1.2, -j.12)$ and $d = .3''$ . Geometry B. . . . .	36
3.13	Calculated $S_{11}$ for $\epsilon_r = 2, 5, 8, 11,$ and $14$ in an X-band fixture (.4" $\times$ .9") when $\mu_r = (1., -j0.)$ , $t = .1''$ and $d = .5''$ . Geometry B. . . . .	38
3.14	Calculated $S_{21}$ for $\epsilon_r = 2, 5, 8, 11,$ and $14$ in an X-band fixture (.4" $\times$ .9") when $\mu_r = (1., -j0.)$ , $t = .1''$ and $d = .5''$ . Geometry B. . . . .	39
3.15	Normalized error in $\epsilon$ for an .002" air gap along the short wall for a rectangular guide with $\epsilon_r = (4.0, -j.20)$ , $\mu_r = (1.2, -j.12)$ and $d = .165''$ . Geometry B but assumed completely filled. . . . .	40
3.16	Normalized error in $\mu$ for an .002" air gap along the long wall for a rectangular guide with $\epsilon_r = (4.0, -j.20)$ , $\mu_r = (1.2, -j.12)$ and $d = .156''$ . Geometry B but assumed completely filled. . . . .	41
3.17	Normalized error in $\epsilon$ for an additional .002" air gap along the long wall for a rectangular guide with $\epsilon_r = (4.0, -j.20)$ , $\mu_r = (1.2, -j.12)$ , $d = .156''$ and assumed $t = .300''$ . Geometry B. . . . .	42
3.18	Normalized error in $\mu$ for an additional .002" air gap along the long wall for a rectangular guide with $\epsilon_r = (4.0, -j.20)$ , $\mu_r = (1.2, -j.12)$ , $d = .156''$ and assumed $t = .300''$ . Geometry B. . . . .	43
4.1	Calculated $S_{11}$ (solid) and $S_{21}$ (dashed) for varying $t$ with $\epsilon_r = (4.0, -j.20)$ , $\mu_r = (1.2, -j.12)$ , $d = .3''$ and $f = 10$ GHz. Geometry A. . . . .	46

4.2	Calculated $S_{11}$ (solid) and $S_{21}$ (dashed) for varying $d$ with $\epsilon_r = (4.0, -j.20)$ , $\mu_r = (1.2, -j.12)$ , $t = .5''$ and $f = 10$ GHz. Geometry A. . . . .	47
4.3	Calculated $S_{11}$ (solid) and $S_{21}$ (dashed) for varying $t$ with $\epsilon_r = (4.0, -j.20)$ , $\mu_r = (1.2, -j.12)$ , $d = .3''$ and $f = 10$ GHz. Geometry B. . . . .	48
4.4	Calculated $S_{11}$ (solid) and $S_{21}$ (dashed) for varying $d$ with $\epsilon_r = (4.0, -j.20)$ , $\mu_r = (1.2, -j.12)$ , $t = .2''$ and $f = 10$ GHz. Geometry B. . . . .	49
4.5	$\epsilon_r$ values using a coaxial airline fixture. . . . .	51
4.6	$\mu_r$ values using a coaxial airline fixture. . . . .	52
4.7	Illustration of X-band fixture used for material measurement. . . . .	53
4.8	Normalized error in extracted permittivity vs. error level added to S parameters. Geometry A with $\epsilon_r = (4.0, -j.20)$ , $\mu_r = (1.2, -j.12)$ , $t = .490''$ , $d = .156''$ and $f = 10$ GHz in an X-band fixture. . . . .	55
4.9	Normalized error in extracted permeability vs. error level added to S parameters. Geometry A with $\epsilon_r = (4.0, -j.20)$ , $\mu_r = (1.2, -j.12)$ , $t = .490''$ , $d = .156''$ and $f = 10$ GHz in an X-band fixture. . . . .	56
4.10	Normalized error in extracted permittivity vs. error level added to S parameters. Geometry B with $\epsilon_r = (4.0, -j.20)$ , $\mu_r = (1.2, -j.12)$ , $t = .3''$ , $d = .156''$ and $f = 10$ GHz in an X-band fixture. . . . .	57
4.11	Normalized error in extracted permeability vs. error level added to S parameters. Geometry B with $\epsilon_r = (4.0, -j.20)$ , $\mu_r = (1.2, -j.12)$ , $t = .3''$ , $d = .156''$ and $f = 10$ GHz in an X-band fixture. . . . .	58
4.12	Measured (solid) and calculated (dashed) $S_{11}$ for $t = .490''$ and $d = .156''$ in an X-band fixture (.4"x.9"). Calculations use $\epsilon_r = (4.0, -j.20)$ and $\mu_r = (1.2, -j.12)$ . Geometry A. . .	62
4.13	Measured (solid) and calculated (dashed) $S_{21}$ for $t = .490''$ and $d = .156''$ in an X-band fixture (.4"x.9"). Calculations use $\epsilon_r = (4.0, -j.20)$ and $\mu_r = (1.2, -j.12)$ . Geometry A. . .	63

4.14	Measured (solid) and calculated (dashed) $S_{11}$ for $t = .300''$ and $d = .156''$ in an X-band fixture (.4"x.9"). Calculations use $\epsilon_r = (4.0, -j.20)$ and $\mu_r = (1.2, -j.12)$ . Geometry B. . .	64
4.15	Measured (solid) and calculated (dashed) $S_{21}$ for $t = .300''$ and $d = .156''$ in an X-band fixture (.4"x.9"). Calculations use $\epsilon_r = (4.0, -j.20)$ and $\mu_r = (1.2, -j.12)$ . Geometry B. . .	65
4.16	Extracted $\epsilon_r$ for Geometry A with $t = .490''$ and $d = .156''$ in an X-band fixture (.4"x.9"). . . . .	66
4.17	Extracted $\mu_r$ for Geometry A with $t = .490''$ and $d = .156''$ in an X-band fixture (.4"x.9"). . . . .	67
4.18	Extracted $\epsilon_r$ for Geometry B with $t = .300''$ and $d = .156''$ in an X-band fixture (.4"x.9"). . . . .	68
4.19	Extracted $\mu_r$ for Geometry B with $t = .300''$ and $d = .156''$ in an X-band fixture (.4"x.9"). . . . .	69
4.20	Single-port fixture geometry. . . . .	70
4.21	Time domain plot for a one-port measurement. Completely filled X band fixture with $d = .156''$ . . . . .	72
4.22	Recovered $S_{11}$ from a measured one-port file (solid) compared with $S_{11}$ from a two-port measurement (dashed). Completely-filled cross-section with $d = .156''$ in an X-band fixture. . .	74
4.23	Recovered $S_{21}$ from a measured one-port file (solid) compared with $S_{21}$ from a two-port measurement (dashed). Completely-filled cross-section with $d = .156''$ in an X-band fixture. . .	75
4.24	Recovered $S_{11}$ from a measured one-port file (solid) compared with $S_{11}$ from a two-port measurement (dashed). Geometry A with $t = .490''$ and $d = .156''$ in an X-band fixture. . .	76
4.25	Recovered $S_{21}$ from a measured one-port file (solid) compared with $S_{21}$ from a two-port measurement (dashed). Geometry A with $t = .490''$ and $d = .156''$ in an X-band fixture. . .	77
4.26	Recovered $S_{11}$ from a measured one-port file (solid) compared with $S_{11}$ from a two-port measurement (dashed). Geometry B with $t = .300''$ and $d = .156''$ in an X-band fixture. . .	78

4.27	Recovered $S_{21}$ from a measured one-port file (solid) compared with $S_{21}$ from a two-port measurement (dashed). Geometry B with $t = .300''$ and $d = .156''$ in an X-band fixture.	79
4.28	Extracted $\epsilon_r$ from a one-port file for a completely-filled waveguide with $d = .156''$ in an X-band fixture. . . . .	80
4.29	Extracted $\mu_r$ from a one-port file for a completely-filled waveguide with $d = .156''$ in an X-band fixture. . . . .	81
4.30	Extracted $\epsilon_r$ from a one-port file. Geometry A with $t = .490''$ and $d = .156''$ in an X-band fixture. . . . .	82
4.31	Extracted $\mu_r$ from a one-port file. Geometry A with $t = .490''$ and $d = .156''$ in an X-band fixture. . . . .	83
4.32	Extracted $\epsilon_r$ from a one-port file. Geometry B with $t = .300''$ and $d = .156''$ in an X-band fixture. . . . .	84
4.33	Extracted $\mu_r$ from a one-port file. Geometry B with $t = .300''$ and $d = .156''$ in an X-band fixture. . . . .	85
A.1	Waveguide regions for the two-port approach. . . . .	90
A.2	Waveguide regions for the one-port approach. . . . .	93
B.1	Matrix solution for the first column of the $s_{11}$ and $s_{21}$ scattering matrices. Geometry A. . . . .	98
B.2	Complete matrix solution for all four scattering matrices. Geometry A. . . . .	99
C.1	Matrix solution for the first column of the $s_{11}$ and $s_{21}$ scattering matrices. Geometry B. . . . .	107
C.2	Complete matrix solution for all four scattering matrices. Geometry B. . . . .	108
D.1	Plot of alpha vs. beta from $t = 0$ to $t = a$ where $\gamma = \alpha + j\beta$ . Geometry A in an X-band fixture (.4''x.9'') with $\epsilon_r = (4.0, -j.20)$ , $\mu_r = (1.2, -j.12)$ , $d = 0.3''$ and $f = 10$ GHz. .	112

D.2	Plot of alpha vs. beta for $TM_y$ modes from $t = 0$ to $t = b$ where $\gamma = \alpha + j\beta$ . Geometry B in an X-band fixture (.4"x.9") with $\epsilon_r = (4.0, -j.20)$ , $\mu_r = (1.2, -j.12)$ , $d = 0.3''$ and $f = 10$ GHz. . . . .	113
D.3	Plot of alpha vs. beta for $TE_y$ modes from $t = 0$ to $t = b$ where $\gamma = \alpha + j\beta$ . Geometry B in an X-band fixture (.4"x.9") with $\epsilon_r = (4.0, -j.20)$ , $\mu_r = (1.2, -j.12)$ , $d = 0.3''$ and $f = 10$ GHz. . . . .	114
D.4	Plot of alpha vs. beta from $f = 8$ GHz to $f = 12$ GHz where $\gamma = \alpha + j\beta$ . Geometry A in an X-band fixture (.4"x.9") with $\epsilon_r = (4.0, -j.20)$ , $\mu_r = (1.2, -j.12)$ , $d = 0.3''$ and $t = 0.6''$ . . . . .	115
D.5	$S_{11}$ vs. number of modes used in calculations. Geometry A with $t = .514''$ , $d = .3''$ and $f = 10$ GHz. . . . .	116
D.6	$S_{21}$ vs. number of modes used in calculations. Geometry A with $t = .514''$ , $d = .3''$ and $f = 10$ GHz. . . . .	117
D.7	$S_{11}$ vs. number of modes used in calculations. Geometry B with $t = .3''$ , $d = .3''$ and $f = 10$ GHz. . . . .	118
D.8	$S_{21}$ vs. number of modes used in calculations. Geometry B with $t = .3''$ , $d = .3''$ and $f = 10$ GHz. . . . .	119



# Chapter 1

## Introduction

The objective of determining the constitutive parameters of a material placed in a fixture can be accomplished by S parameter measurements conducted by broadband network analyzers [1]. A common piece of apparatus used in the measurements is a waveguide fixture. Traditionally when a waveguide is used, its cross section is completely filled with a fixed length of the material to be measured. A method of parameter determination is now desired where the technique used yields results which is not significantly affected when the fixture is subjected to a high temperature environment. Such an environment is likely to introduce error to a completely filled wave-guide due to temperature expansion of the material and the waveguide itself causing air gaps between the fixture and material. Accuracy may even be diminished when undesired air gaps already exist or when there is not a sufficiently tight fit between the waveguide walls and the material. Error correction formulas compensating for the air gaps have appeared previously [2,3,4]. However, one is valid only for low loss dielectrics and the other is merely an empirical formula.

An alternate method is investigated for the rectangular waveguide where a known air gap exists between the waveguide walls and material sam-

ple [5,6,7]. The goal is to minimize the errors which occur due to limitations in the accuracy of the dimensions of the material and change in the dimensions caused by thermal expansion. Two different geometries are considered. The first geometry has the air gap oriented parallel to the shorter wall. The other has the gap running parallel to the longer wall. The main disadvantage of these alternate geometries is the increased complexity they add to their S parameter expressions, thereby increasing the amount of time in extraction of the proper set of constitutive parameters.

This report will first discuss the traditional method of extracting  $\epsilon$  and  $\mu$  from S parameter measurements using fixtures with their sample region completely filled [8]. This direct method does not work when the cross-sectional region is not completely filled due to the presence of higher order modes. An alternative approach is presented to accomplish the  $\epsilon$  and  $\mu$  parameter extraction process. Unlike the former approach, explicit relationships between the material parameters and the S parameters are not possible. The latter approach is dependent upon an iterative technique (Newton-Raphson) to acquire the material parameters from the S parameters through the use of an analytical model.

The presence of partially-filled cross-section requires a detailed field analysis. Such a field analysis is described first for two rectangular waveguide samples geometries followed by a parameter study for the S parameters. Next, the actual iteration technique is discussed to obtain the constitutive parameters from the measured S parameter data. This technique is applied and demonstrated for two different measurement fixture configurations, i.e., a one port and two port fixture. The measured S parameters for the different fixture configurations are examined and compared to expected values based upon independent extracted values for  $\epsilon$  and  $\mu$ . This is followed by



a display of extracted parameter values using the developed techniques. Finally, the conclusions of these methods for parameter determination and suggestions for further exploration are given.

## Chapter 2

# Material Parameter Extraction Using Waveguides

A common approach for parameter determination is to obtain reflection and transmission measurements for a fixed length of material in a waveguide fixture (coaxial or rectangular) with the fixture cross section completely filled. The parameters extracted from such an approach are subject to error from sample condition (homogeneity, dimensions and shape distortions) and measurement hardware calibration. Examples of error magnitude will be presented for some of the errors. The error which occurs from a partially-filled fixture cross section is presented in the following chapter. The basic equations used for such parameter extraction are presented here.

The S parameters  $S_{11}$  and  $S_{21}$  can be measured by automated broadband network analyzers in the frequency range where only the dominant mode is able to propagate in the unfilled sections of the waveguide. These measurements can be related to the reflection ( $s_{11}$ ) and transmission ( $P$ ) coefficients of a material junction of semi-infinite length. The relationships are

$$S_{11} = \frac{(1 - P^2(\epsilon, \mu))s_{11}(\epsilon, \mu)}{1 - P^2(\epsilon, \mu)s_{11}^2(\epsilon, \mu)} \quad (2.1)$$

and

$$S_{21} = \frac{(1 - s_{11}^2(\epsilon, \mu))P(\epsilon, \mu)}{1 - P^2(\epsilon, \mu)s_{11}^2(\epsilon, \mu)}. \quad (2.2)$$

The previous expressions can be rewritten to express  $s_{11}$  and  $P$  in terms of  $S_{11}$  and  $S_{21}$ . These expressions are

$$P = \frac{S_{11} + S_{21} - s_{11}}{1 - (S_{11} + S_{21})s_{11}} \quad (2.3)$$

and

$$s_{11} = K \pm \sqrt{K^2 - 1} \quad (2.4)$$

where

$$K = \frac{S_{11}^2 - S_{21}^2 + 1}{2S_{11}}. \quad (2.5)$$

The sign in Equation (2.4) is chosen to insure  $|s_{11}| \leq 1$ .

These new characteristics,  $s_{11}$  and  $P$ , can be related to the material parameters. The relationships for a coaxial waveguide fixture are

$$P = e^{-j\frac{\omega}{c}\sqrt{\epsilon_r\mu_r}d} \quad (2.6)$$

and

$$s_{11} = \frac{\sqrt{\frac{\mu_r}{\epsilon_r}} - 1}{\sqrt{\frac{\mu_r}{\epsilon_r}} + 1}. \quad (2.7)$$

Note that  $\epsilon = \epsilon_r\epsilon_0$  and  $\mu = \mu_r\mu_0$  where the subscript notation refers to relative and free space values.

The corresponding relationships for a rectangular waveguide fixture are

$$P = e^{-j\frac{\omega}{c}X_1\sqrt{\epsilon_r\mu_r}d} \quad (2.8)$$

and

$$s_{11} = \frac{\sqrt{\frac{\mu_r}{\epsilon_r} \frac{X_o}{X_1} - 1}}{\sqrt{\frac{\mu_r}{\epsilon_r} \frac{X_o}{X_1} + 1}} \quad (2.9)$$

where  $X_o = \sqrt{1 - (\frac{\lambda_o}{2a})^2}$  and  $X_1 = \sqrt{1 - (\frac{\lambda_o}{2a\sqrt{\epsilon_r\mu_r}})^2}$  with  $\lambda_o$  being the free space wavelength,  $c$  the speed of light and  $a$  is the width of the rectangular guide.

The final expressions for the constitutive parameters using a coaxial waveguide are given by

$$\mu_r = \sqrt{xy} \quad (2.10)$$

and

$$\epsilon_r = \sqrt{\frac{y}{x}} \quad (2.11)$$

where

$$x = \left(\frac{1 + s_{11}}{1 - s_{11}}\right)^2 \quad (2.12)$$

and

$$y = -\left\{\frac{c}{\omega d} \ln\left(\frac{1}{P}\right)\right\}^2 \quad (2.13)$$

The final expressions for the constitutive parameters using a rectangular waveguide are given by

$$\mu_r = \frac{1 + s_{11} \lambda_o}{1 - s_{11} \Lambda X_o} \quad (2.14)$$

and

$$\epsilon_r = \left( \frac{1}{\Lambda^2} + \frac{1}{(2a)^2} \right) \frac{\lambda_o^2}{\mu_r} \quad (2.15)$$

where

$$\frac{1}{\Lambda^2} = - \left[ \frac{1}{2\pi d} \ln \frac{1}{P} \right]^2 \quad (2.16)$$

Note that  $\ln \frac{1}{P}$  is modulo  $j2\pi n$  where  $n$  is the integer of  $\frac{d}{\lambda_g}$ . The proper value of  $n$  can be estimated with the integer value of

$$n = \text{Int} \left[ \frac{f \Phi'}{2\pi} \right] \quad (2.17)$$

where  $\Phi'$  is the derivative (slope) of the phase for the transmission coefficient  $P$  with respect to frequency and  $f$  is frequency.

An important aspect in parameter determination is the error occurring from calibration and sample dimensions. The following examples are for coaxial and rectangular waveguide fixtures with sample parameters of  $\epsilon_r = (4.0, -j.20)$  and  $\mu_r = (1.2, -j.12)$  and a length of  $d=.3''$ . Figures 2.1 through 2.4 illustrate error from the phase reference plane position for phase offsets in  $S_{11}$  corresponding to distances of  $.001''$  and  $.003''$ . The error is defined as

$$\% \text{ Error} = \frac{\text{Extracted Value} - \text{Exact Value}}{\text{Exact Value}} \times 100\%. \quad (2.18)$$

The phase offset error (position) results in a comparable amount of error for both fixture types with the imaginary component of  $\epsilon$  being very sensitive

to the position of the reference plane. Similar results also occur for the  $\mu$  parameter.

Figures 2.5 through 2.8 illustrate the error when the sample length is assumed to be .3" but is actually .302" for the solid curves and .298" for the dashed curves. The fixtures perform differently in this case with the coaxial fixture yielding error which remains essentially constant with varying frequency. The rectangular waveguide fixture has error which decreases as frequency is increased. For both fixtures the error in extracting constitutive parameters is not very sensitive to inaccurate sample lengths.

Other sources of error arise from other discontinuities occurring in the measurement system. The best solution so far to eliminate or minimize these errors lies in a calibration technique [9]. It is also advisable to use a fixture with sufficient length to separate the returns due to the fixture junctions from the sample return in the interior region of the fixture and to insure that only the dominant mode is incident on the sample.

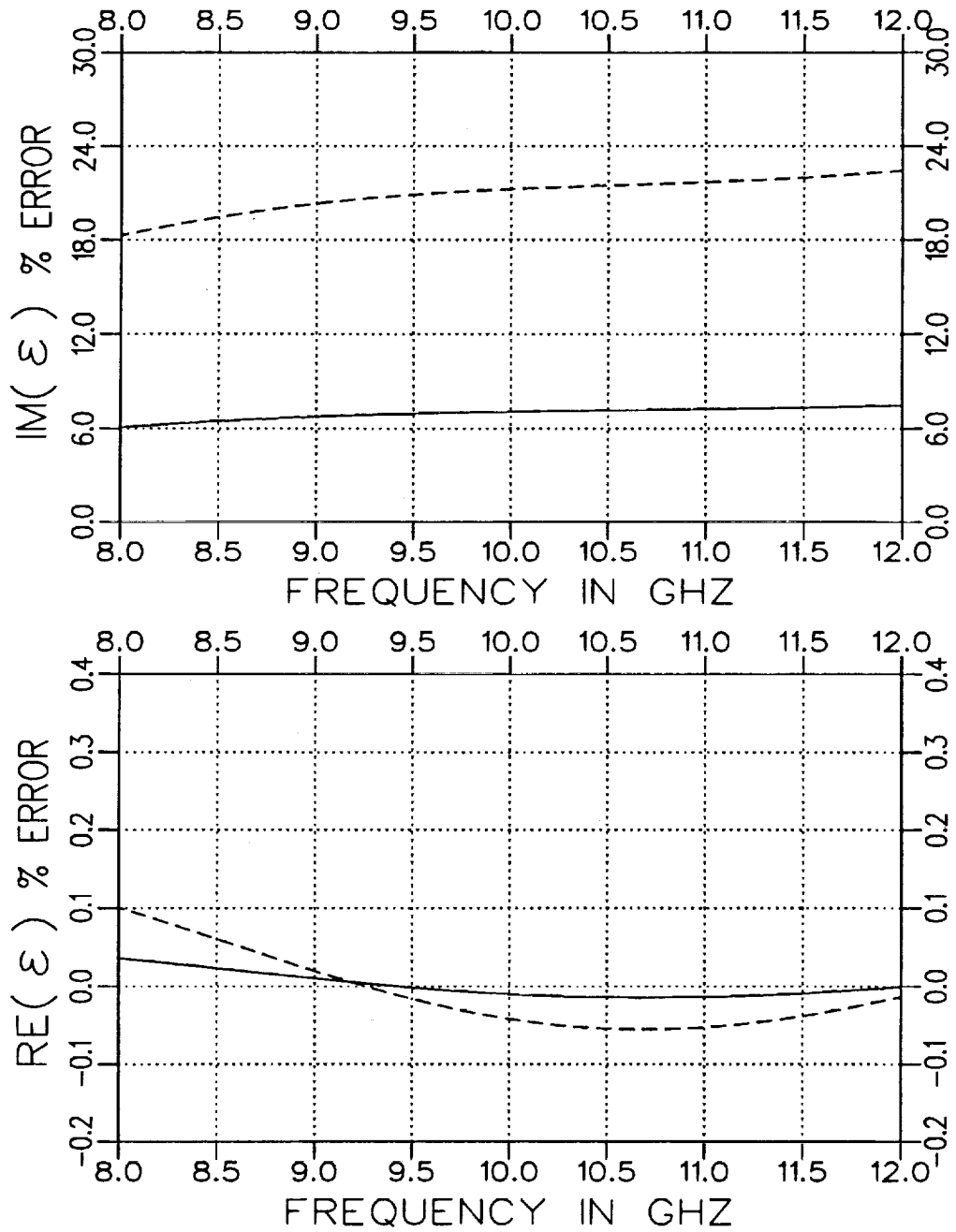


Figure 2.1: Normalized error for  $\epsilon$  when  $S_{11}$  has a position error of .001" (solid) and .003" (dashed). The sample parameters are  $\epsilon_r = (4.0, -j.20)$  and  $\mu_r = (1.2, -j.12)$  with  $d = .3"$ . Coaxial airline fixture.

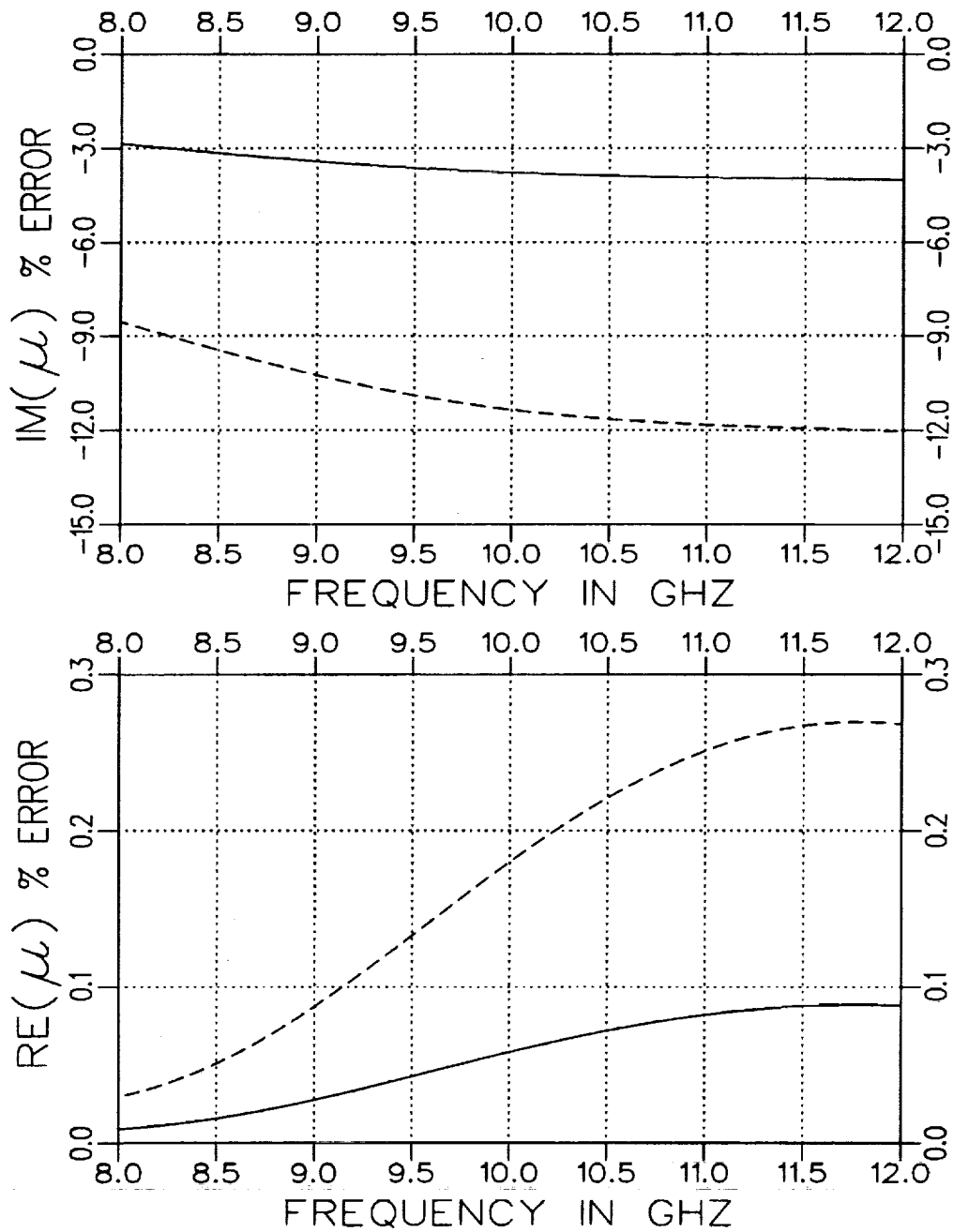


Figure 2.2: Normalized error for  $\mu$  when  $S_{11}$  has a position error of .001" (solid) and .003" (dashed). The sample parameters are  $\epsilon_r = (4.0, -j.20)$  and  $\mu_r = (1.2, -j.12)$  with  $d = .3$ ". Coaxial airline fixture.



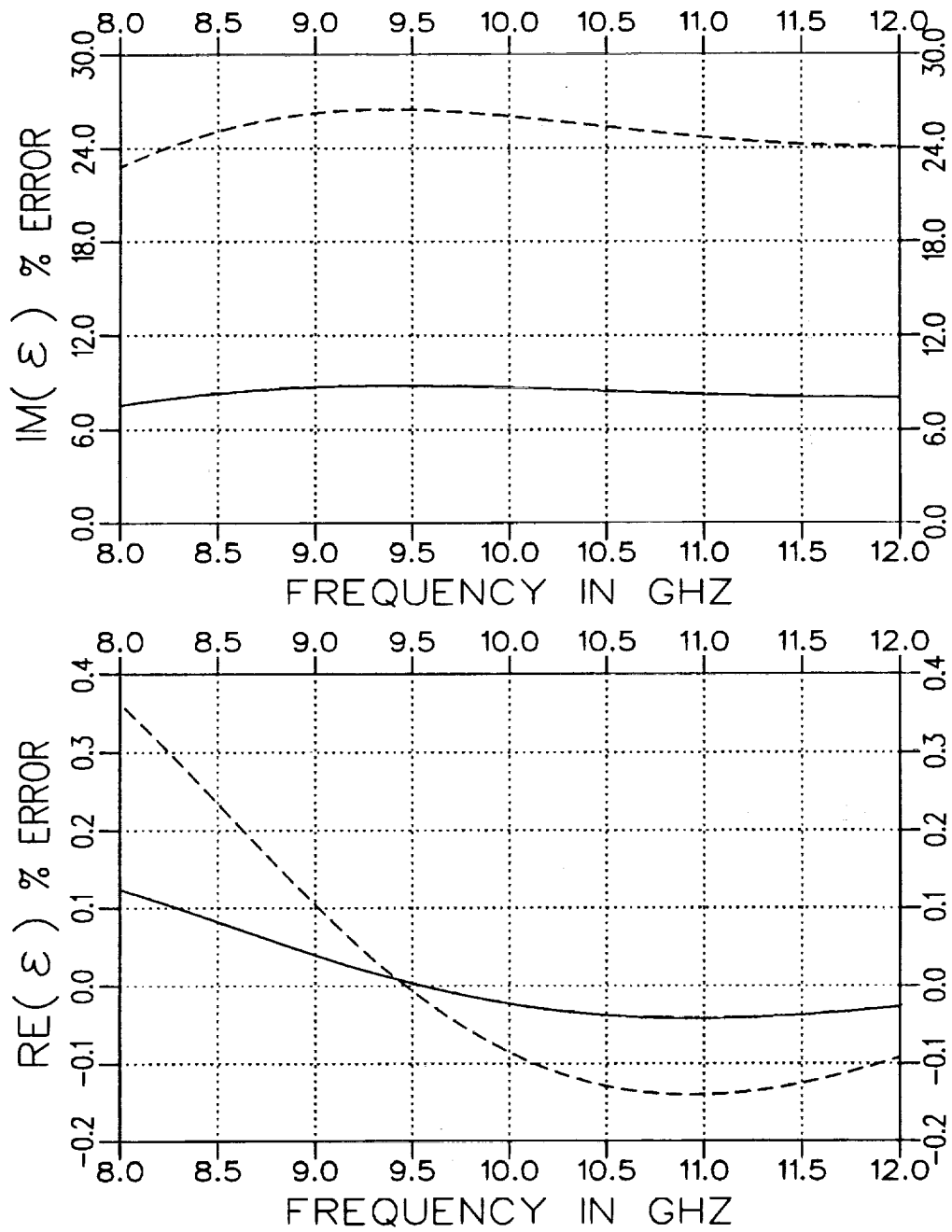


Figure 2.3: Normalized error for  $\epsilon$  when  $S_{11}$  has a position error of .001" (solid) and .003" (dashed). The sample parameters are  $\epsilon_r = (4.0, -j.20)$  and  $\mu_r = (1.2, -j.12)$  with  $d = .3"$ . Rectangular waveguide fixture.

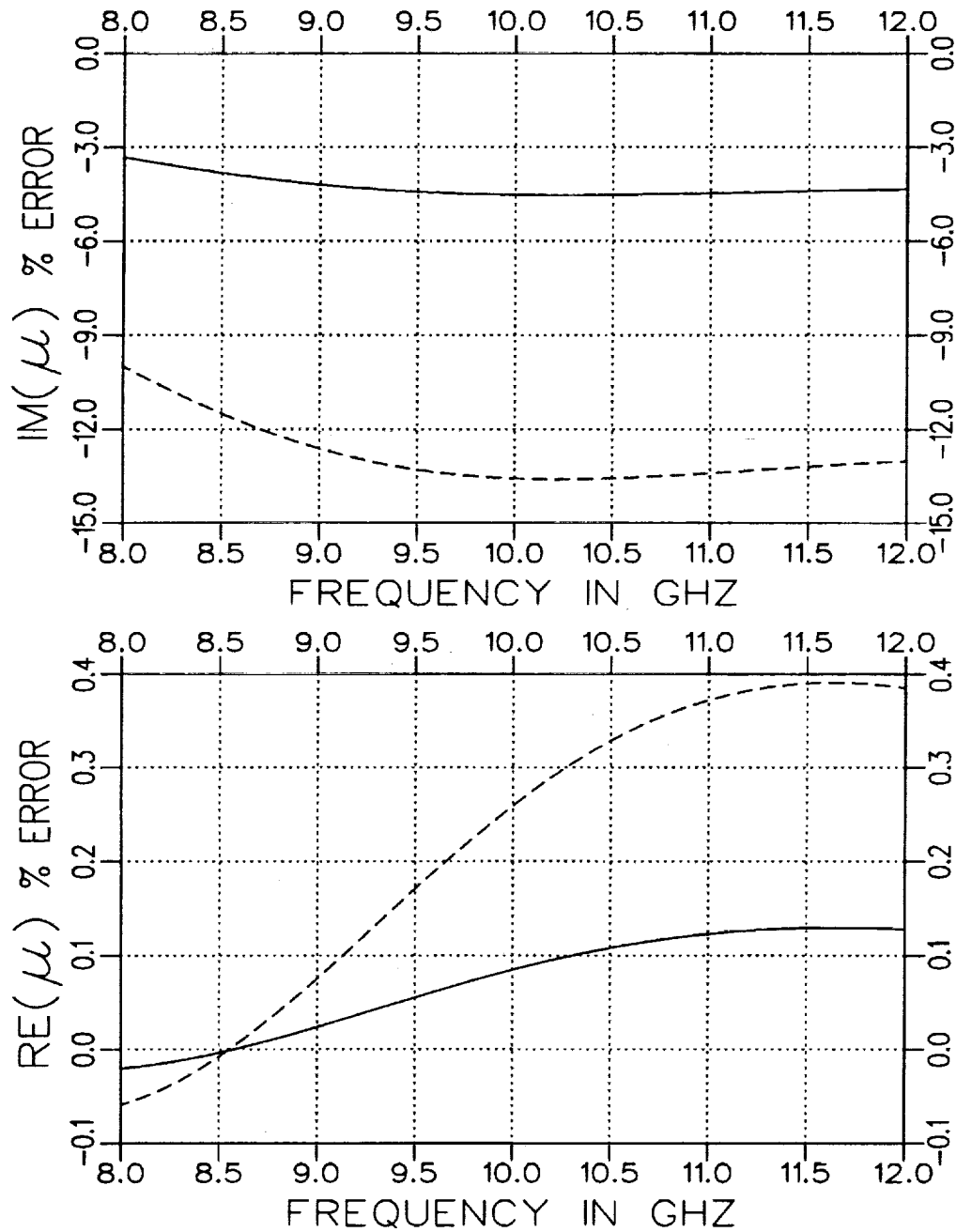


Figure 2.4: Normalized error for  $\mu$  when  $S_{11}$  has a position error of .001" (solid) and .003" (dashed). The sample parameters are  $\epsilon_r = (4.0, -j.20)$  and  $\mu_r = (1.2, -j.12)$  with  $d = .3''$ . Rectangular waveguide fixture.

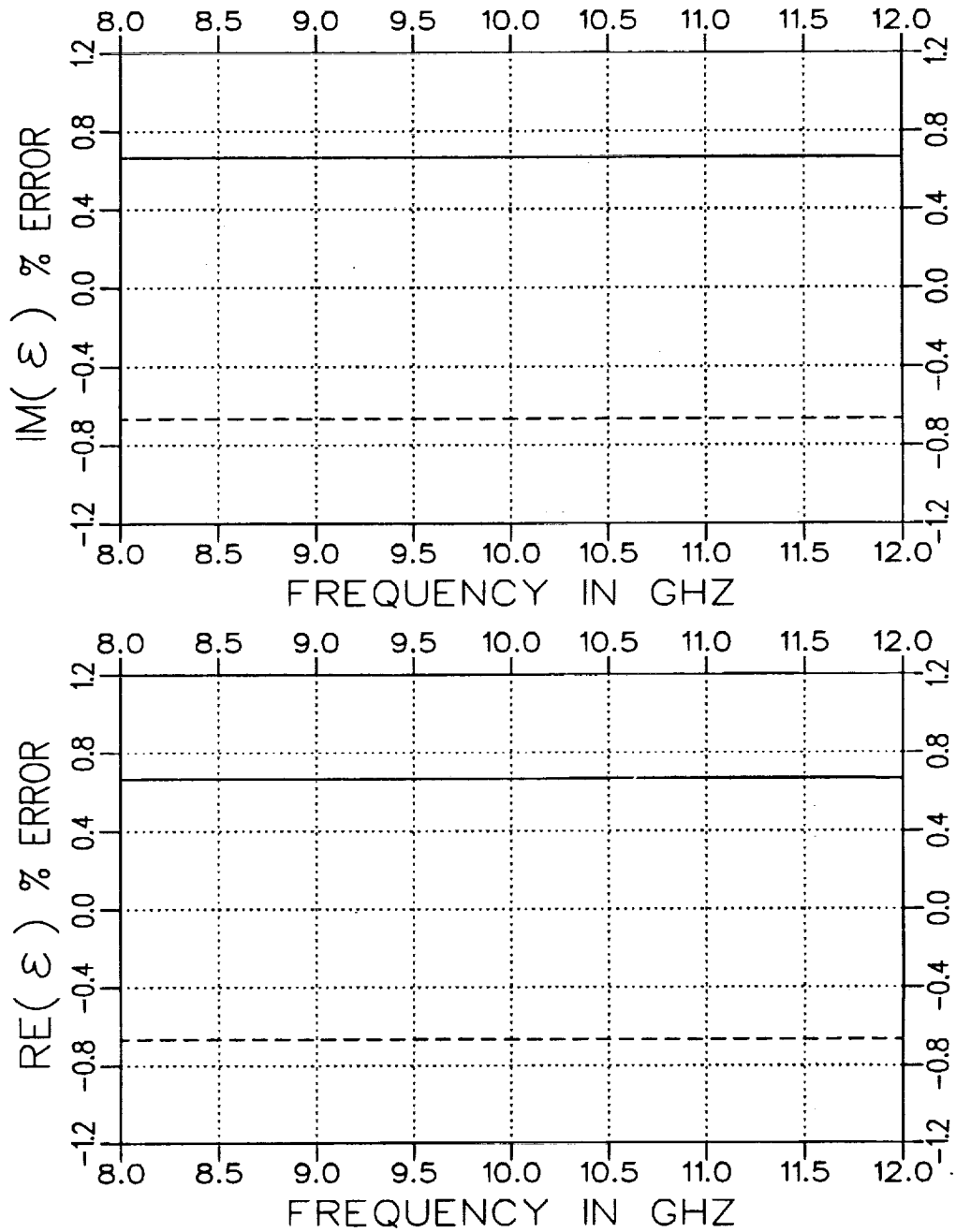


Figure 2.5: Normalized error for  $\epsilon$  when  $S_{11}$  has a sample length error of  $+.002''$  (solid) and  $-.002''$  (dashed). The sample parameters are  $\epsilon_r = (4.0, -j.20)$  and  $\mu_r = (1.2, -j.12)$  with assumed  $d = .3''$ . Coaxial airline fixture.

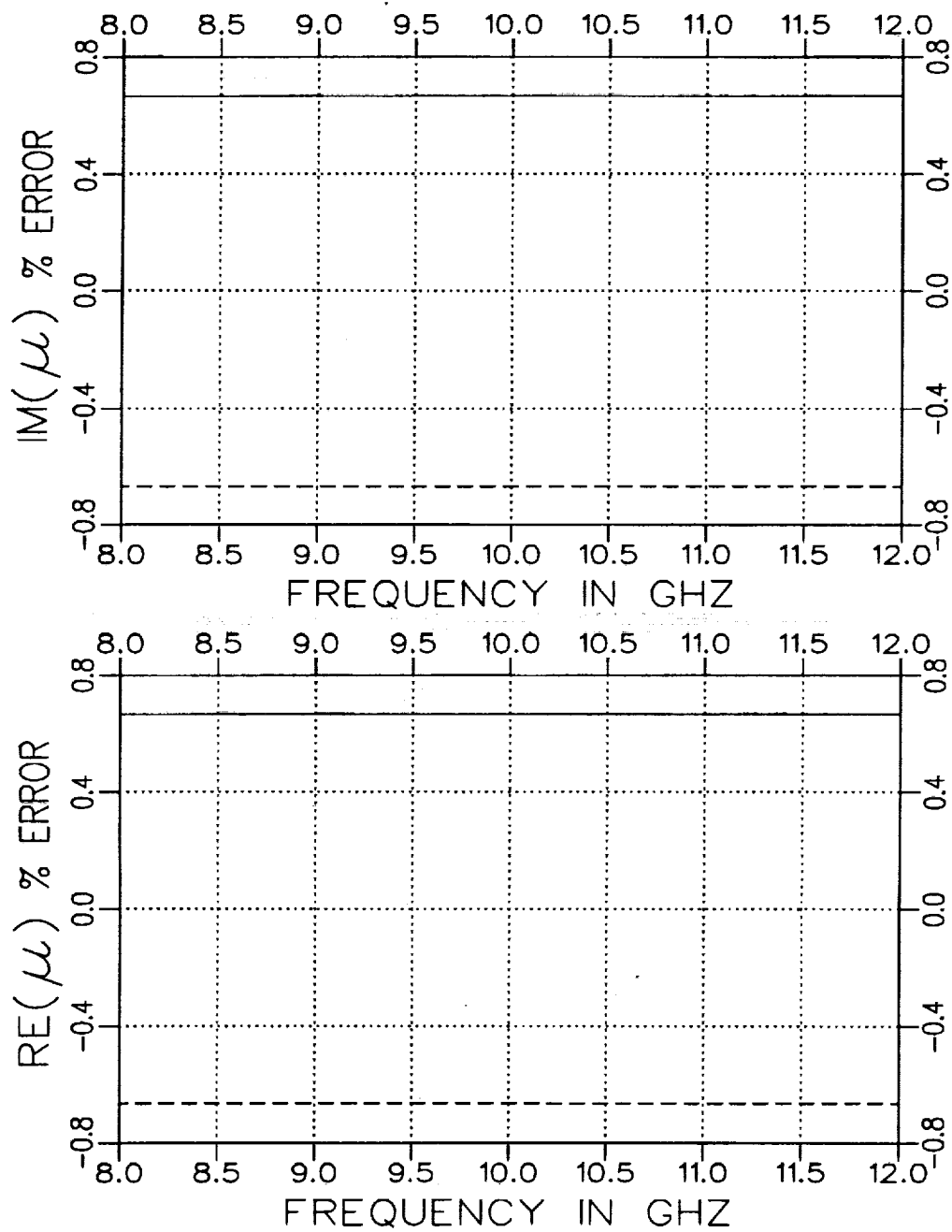


Figure 2.6: Normalized error for  $\mu$  when  $S_{11}$  has a sample length error of  $+.002''$  (solid) and  $-.002''$  (dashed). The sample parameters are  $\epsilon_r = (4.0, -j.20)$  and  $\mu_r = (1.2, -j.12)$  with assumed  $d = .3''$ . Coaxial airline fixture.

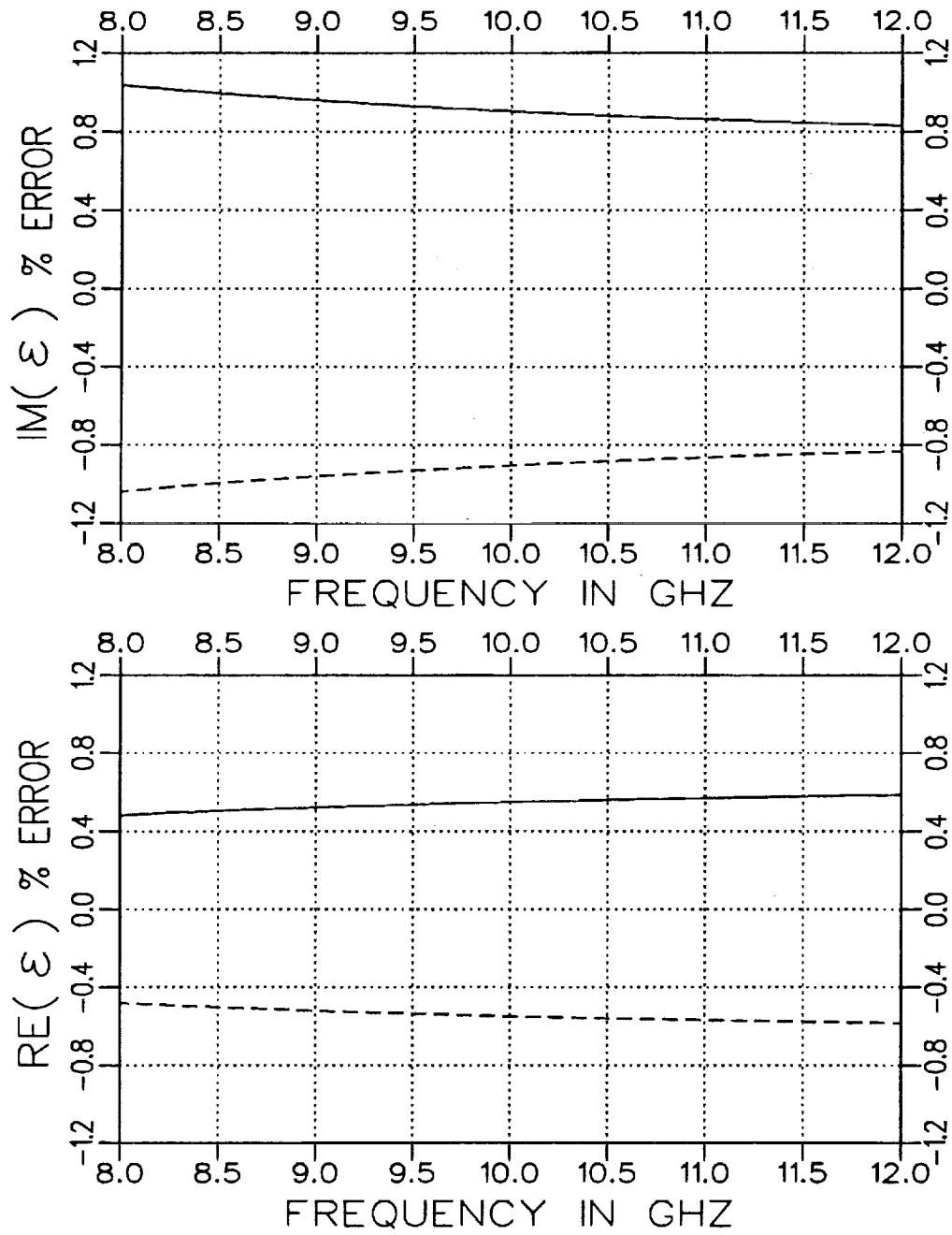


Figure 2.7: Normalized error for  $\epsilon$  when  $S_{11}$  has a sample length error of  $+.002''$  (solid) and  $-.002''$  (dashed). The sample parameters are  $\epsilon_r = (4.0, -j.20)$  and  $\mu_r = (1.2, -j.12)$  with assumed  $d = .3''$ . Rectangular waveguide fixture.

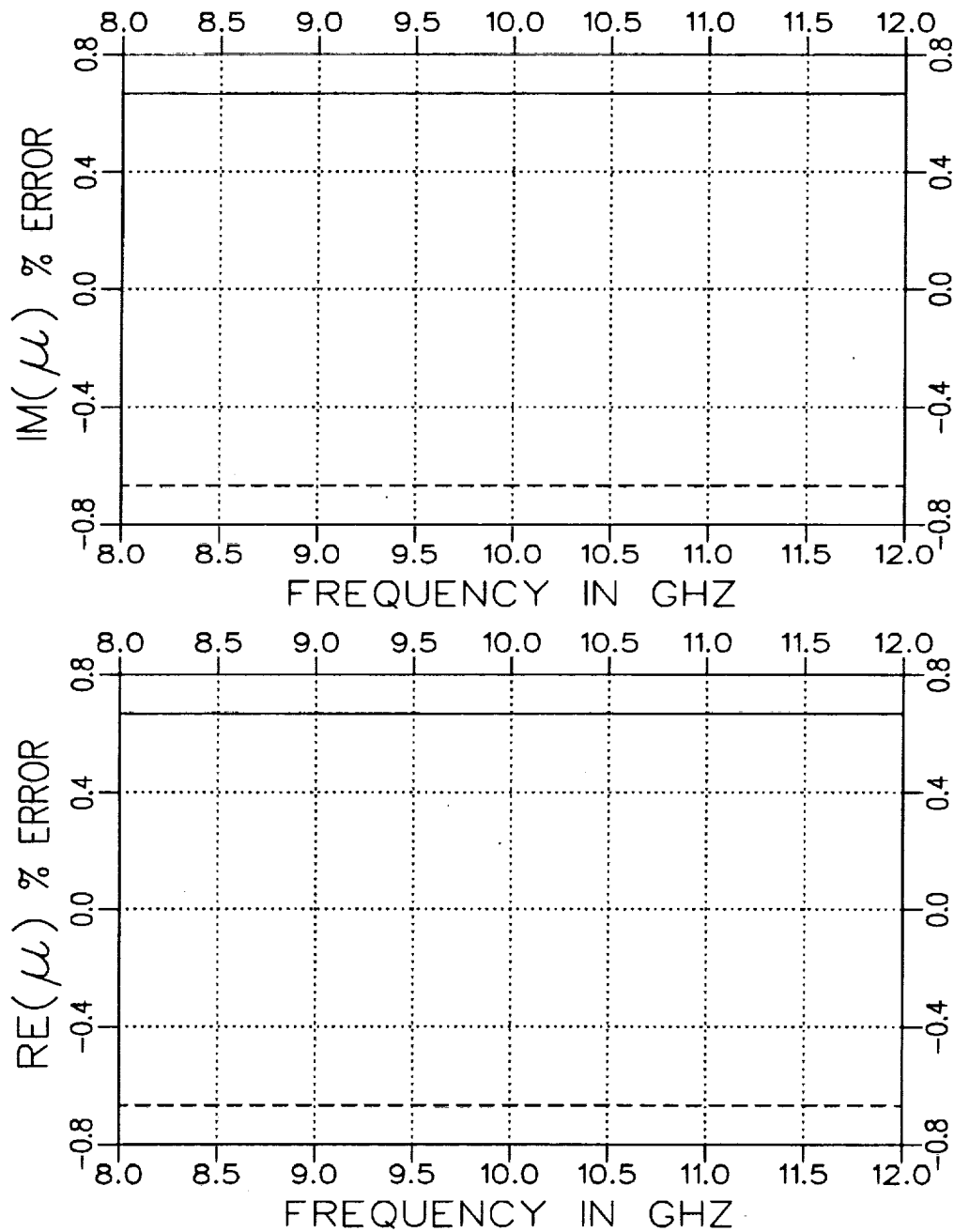


Figure 2.8: Normalized error for  $\mu$  when  $S_{11}$  has a sample length error of  $+.002''$  (solid) and  $-.002''$  (dashed). The sample parameters are  $\epsilon_r = (4.0, -j.20)$  and  $\mu_r = (1.2, -j.12)$  with assumed  $d = .3''$ . Rectangular waveguide fixture.

## Chapter 3

# Partially-Filled Waveguides

Obtaining accurate  $\epsilon$  and  $\mu$  values from S parameter measurements using a completely-filled waveguide geometry requires a tight fit between the dielectric material and the walls of the waveguide. Alternate sample geometries will now be explored where a known air gap is introduced between the material sample and one of the walls of the rectangular waveguide. Two different sample geometries for the dielectric sample are shown in Figure 3.1 which are of interest. The main motivation for considering these geometries arises from a potentially less sensitive S parameter quantity. This sensitivity could introduce error in the desired material parameters and would primarily be due to air gaps between the sample and fixture walls. These air gaps arise from errors in sample dimensions and thermal expansion. Reducing the sensitivity of the S parameter measurements should facilitate the process of extracting accurate values for the constitutive parameters. Another motivation is the potential of increased flexibility in sample sizes these alternate sample geometries may provide. A greater choice of measurements exists because of the variety of material sample thicknesses possible.

Compared with the completely-filled case, the numerical acquisition of the S parameters requires a significantly greater amount of numerical calcu-

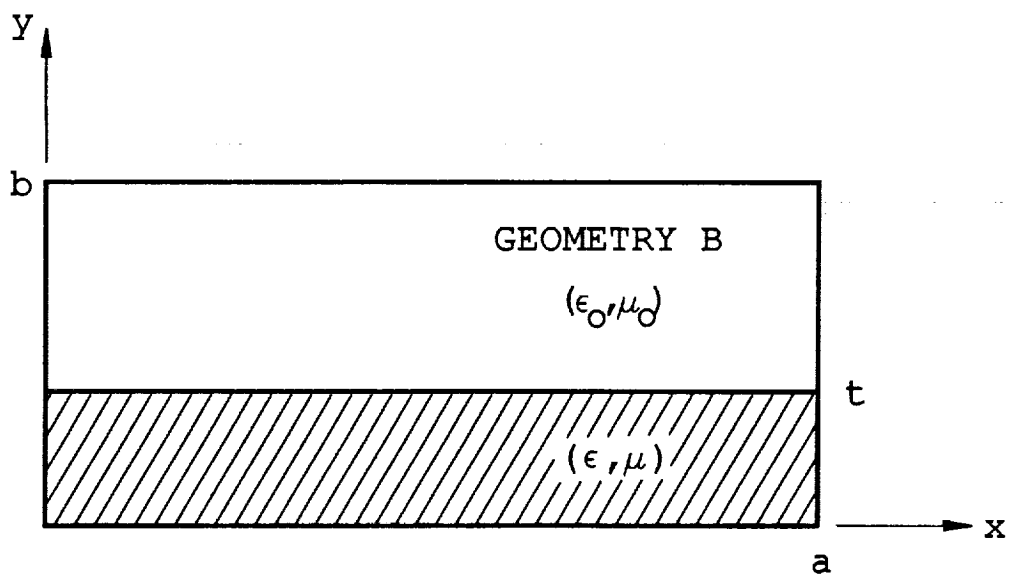
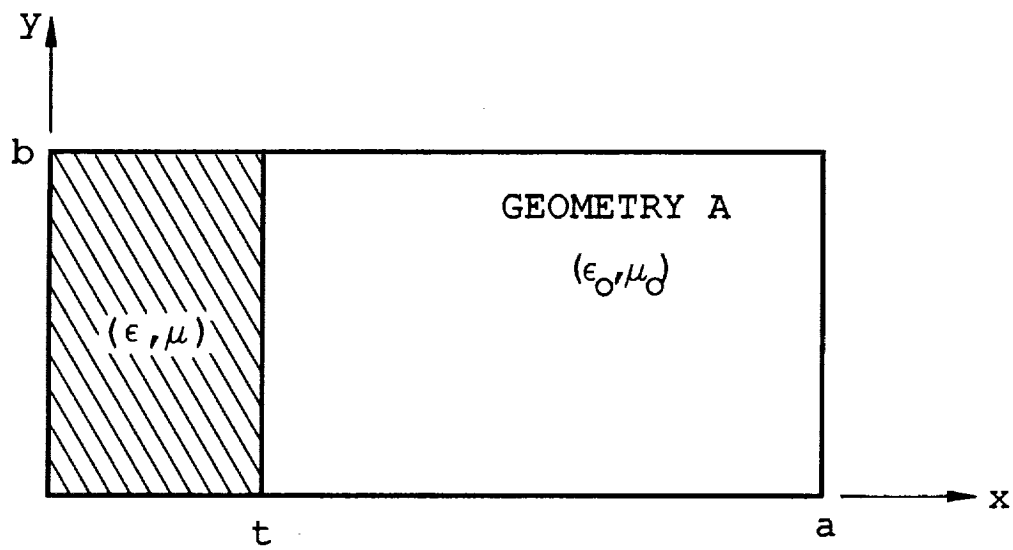


Figure 3.1: Partially-filled waveguide geometries.



lation. Because explicit relationships between the constitutive parameters and S parameters are not available, an iterative Newton-Raphson search is used to extract  $\epsilon$  and  $\mu$  from a set of S parameter data. The search involves iterating on  $\epsilon$  and  $\mu$  until the following two functionals are driven to zero:

$$F_1 = S_{11}^{cal} - S_{11}^{meas} \quad (3.1)$$

and

$$F_2 = S_{21}^{cal} - S_{21}^{meas}. \quad (3.2)$$

The calculation of the S parameters themselves involves a modal expansion of the  $E$  and  $H$  field quantities in all three regions of the waveguide and then matching the tangential field components at each material junction ( $z=0$  and  $z=d$ ). The matching process is essentially a three dimensional method of moments solution using entire basis functions.

The problem can be reduced to matching the fields at only one material junction ( $z=0$ ) if a self-consistent technique is employed (see Appendix A). That is, the problem can be simplified to the semi-infinite case depicted in Figure 3.2 [10]. The expressions for the S parameters of a two-port system are then given by

$$S_{11} = [s_{11}] + [s_{12}][P][s_{22}][P] (I - [s_{22}][P][s_{22}][P])^{-1} [s_{21}] \quad (3.3)$$

and

$$S_{21} = [s_{12}][P] (I - [s_{22}][P][s_{22}][P])^{-1} [s_{21}]. \quad (3.4)$$

The variables  $s_{ij}$  are the modal scattering matrices for the semi-infinite geometry and  $[P]$  is the modal propagation matrix corresponding to length  $d$ .

For the one-port case, the self-consistent expression for  $S_{11}$  is

$$S_{11} = [s_{11}] + [s_{12}][M'] \{I - [s_{22}][M']\}^{-1} [s_{21}] \quad (3.5)$$

where

$$\begin{aligned} [M'] = [P_1] \{ & [s_{22}] - [s_{21}][P_2][P_2] \\ & \cdot (I + [s_{11}][P_2][P_2])^{-1} [s_{12}] \} [P_1]. \end{aligned} \quad (3.6)$$

The variables  $[P_1]$  and  $[P_2]$  are the modal propagation matrices corresponding to the lengths  $d$  and  $\ell$ , respectively.

## I Field Expansions—Geometry A

The required elements for the scattering matrices  $[s_{ij}]$  are obtained through a modal matching technique for the field expansions in both regions. The tangential field matching yields expansion coefficients for the expansion modes. The expansion modes (TE<sub>x</sub>) for Geometry A in a rectangular fixture are given below.

Region I

$$E_y = (e^{-\Gamma_1 z} + a_1 e^{\Gamma_1 z})\Phi_1 + \sum_{n=2}^{\infty} a_n \Phi_n e^{\Gamma_n z} \quad (3.7)$$

and

$$H_x = -Y_1(e^{-\Gamma_1 z} - a_1 e^{\Gamma_1 z})\Phi_1 + \sum_{n=2}^{\infty} a_n Y_n \Phi_n e^{\Gamma_n z} \quad (3.8)$$

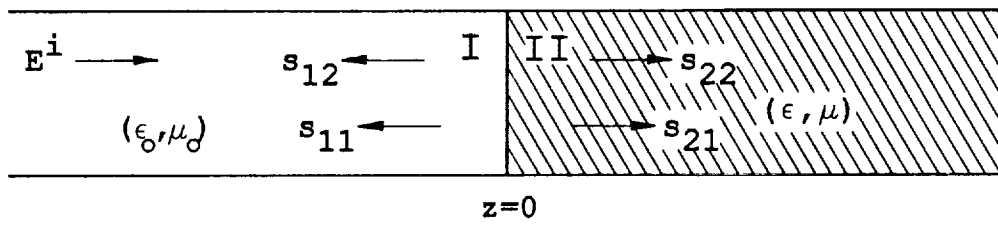
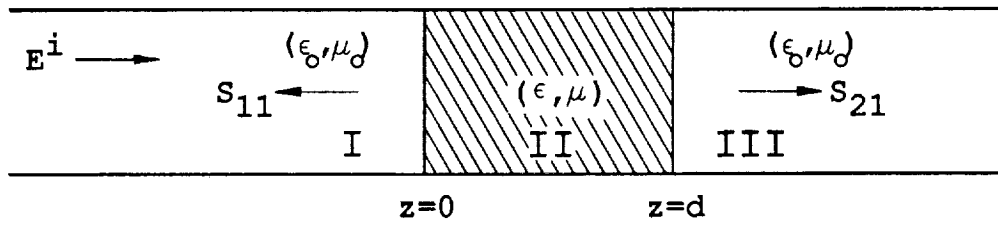


Figure 3.2: Waveguide regions.

where

$$\Phi_n = \sqrt{\frac{2}{a}} \sin \frac{n\pi}{a} x, \quad (3.9)$$

$$\Gamma_n^2 = \left(\frac{n\pi}{a}\right)^2 - k_o^2 \text{ and} \quad (3.10)$$

$$Y_n = \frac{\Gamma_n}{jZ_o k_o}. \quad (3.11)$$

Region II

$$E_y = \sum_{n=1}^{\infty} b_n \Psi_n e^{-\gamma_n z} \quad (3.12)$$

and

$$H_x = - \sum_{n=1}^{\infty} b_n Y_{in} \Psi_n e^{-\gamma_n z} \quad (3.13)$$

where

$$\begin{aligned} \Psi_n &= C \sin k_{x_{1n}} x && \text{for } 0 \leq x \leq t, \\ \Psi_n &= C \frac{\sin k_{x_{1n}} t}{\sin k_{x_{0n}} (a-t)} \sin k_{x_{0n}} (a-x) && \text{for } t \leq x \leq a, \\ \gamma_n^2 &= k_{x_{1n}}^2 - k_o^2 \epsilon_r \mu_r = k_{x_{0n}}^2 - k_o^2, && (3.14) \\ Y_{1n} &= \frac{\gamma_n}{jZ_o k_o \mu_r} && \text{for } 0 \leq x \leq t, \\ Y_{0n} &= \frac{\gamma_n}{jZ_o k_o} && \text{for } t \leq x \leq a \end{aligned}$$

and  $C$  is a normalization constant. The constants  $k_{x_{1n}}$  and  $k_{x_{0n}}$  are found using an iterative Newton-Raphson technique and satisfy the following transcendental equation [5]

$$-k_{x_{1n}} \cos k_{x_{1n}} t \sin k_{x_{0n}} (a-t) = \mu_r k_{x_{0n}} \sin k_{x_{1n}} t \cos k_{x_{0n}} (a-t). \quad (3.15)$$

Continuity of the field components is now imposed at the junction  $z=0$ . Next the equations are multiplied by  $\Phi_q$  ( $q = 1, 2, \dots, N$ ) and integrated from  $x=0$  to  $x=a$ . The final matrix form of the solution is given in Appendix B.

## II Field Expansions—Geometry B

For geometry B, because both TE<sub>y</sub> and TM<sub>y</sub> modes are excited, the expansion modes for both tangential field components,  $y$  and  $x$ , are needed to solve for the expansion coefficients. Below are the field expansions for this particular geometry. See Appendix C for the definitions of the functions and constants.

Region I

$$E_y = (e^{-\Gamma_0 z} + a_0^M e^{\Gamma_0 z}) A_0 Z_0^M \Phi_0^I + \sum_{n=1}^{\infty} a_n^M e^{\Gamma_n z} A_n Z_n^M \Phi_n^I, \quad (3.16)$$

$$E_x = \sum_{n=1}^{\infty} (a_n^M B_n + a_n^E C_n Z_n^E) \Phi_n^{\Pi} e^{\Gamma_n z}, \quad (3.17)$$

$$H_x = (-e^{-\Gamma_0 z} + a_0^M e^{\Gamma_0 z}) A_0 \Phi_0^I + \sum_{n=1}^{\infty} (a_n^M A_n + a_n^E B_n) \Phi_n^I e^{\Gamma_n z}, \quad (3.18)$$

$$H_y = -\sum_{n=1}^{\infty} a_n^E C_n \Phi_n^{\Pi} e^{\Gamma_n z}. \quad (3.19)$$

Region II

$$E_y = \sum_{n=0}^{\infty} b_n^M A_n^M Z_n^{Mi} \Psi_n^{IM} e^{-\gamma_n^M z}, \quad (3.20)$$

$$E_x = \sum_{n=1}^{\infty} (b_n^M B_n^M \Psi_n^{\Pi M} e^{-\gamma_n^M z} + b_n^E C_n^E Z_n^{E1} \Psi_n^{\Pi E} e^{-\gamma_n^E z}), \quad (3.21)$$

$$H_x = -b_0^M A_0^M \Psi_0^{IM} e^{-\gamma_0^M z} \quad (3.22)$$

$$- \sum_{n=1}^{\infty} (b_n^M A_n^M \Psi_n^{IM} e^{-\gamma_n^M z} + b_n^E B_n^E \Psi_n^{IE} e^{-\gamma_n^E z}), \quad (3.23)$$

$$H_y = \sum_{n=1}^{\infty} b_n^E C_n^E \frac{\mu_1}{\mu_i} \Psi_n^{IE} e^{-\gamma_n^E z}. \quad (3.24)$$

The constants  $k_{y_{1n}}^M$  and  $k_{y_{0n}}^M$  satisfy the following transcendental equation [5] and are found using an iterative Newton-Raphson technique:

$$-k_{y_{1n}}^M \sin k_{y_{1n}}^M t \cos k_{y_{0n}}^M (b-t) = \epsilon_r k_{y_{0n}}^M \cos k_{y_{1n}}^M t \sin k_{y_{0n}}^M (b-t). \quad (3.25)$$

The constants  $k_{y_{1n}}^E$  and  $k_{y_{0n}}^E$  satisfy the following:

$$-k_{y_{1n}}^E \cos k_{y_{1n}}^E t \sin k_{y_{0n}}^E (b-t) = \mu_r k_{y_{0n}}^E \sin k_{y_{1n}}^E t \cos k_{y_{0n}}^E (b-t). \quad (3.26)$$

As before, the continuity of the field quantities is imposed across the junction  $z=0$ . The first and third equations are multiplied by  $\Phi_q^I$  ( $q = 0, 1, \dots, N$ ) and the second and fourth equations by  $\Phi_q^{II}$  ( $q = 1, 2, \dots, N$ ). Next the equations are integrated from  $y=0$  to  $y=b$ . The final matrix form of the equations is given in Appendix C.

### III Calculations

Computer software was generated to calculate  $S_{11}$  and  $S_{21}$  for the discussed sample geometries, A and B. The following plots demonstrate the sensitivities for  $S_{11}$  and  $S_{21}$  for various gap dimensions and material constants. Additional plots are provided to demonstrate the error in extracting  $\epsilon$  and  $\mu$  when a gap is present in the S parameter data and processing this data as if no gap were present.

The accuracy of the S parameters, of course, depends on the number of terms or modes kept in the field expansions. The number of modes needed to insure convergence is discussed in Appendix D.

#### III.1 Geometry A

Figures 3.3 and 3.4 illustrate  $S_{11}$  and  $S_{21}$  for  $t = .2'', .5'', .7'',$  and  $.9''$  in an X-band fixture ( $.4'' \times .9''$ ) when  $\epsilon_r = (4.0, -j.20)$ ,  $\mu_r = (1.2, -j.12)$  and  $d = .3''$ . The variation of  $S_{11}$  and  $S_{21}$  decreases rapidly as the guide becomes

completely filled which indicates a small air gap to the short wall may not be that critical.

Figures 3.5 and 3.6 illustrate  $S_{11}$  and  $S_{21}$  for  $\epsilon_r = 2, 5, 8, 11,$  and  $14$  in an X-band fixture (.4"x.9") when  $\mu_r = (1., -j0.)$ ,  $t=.1''$  and  $d=.3''$ . The variation of  $S_{11}$  is quite sensitive for any loading and  $S_{21}$  would show more variation if loss was present in the sample.

Figures 3.7 and 3.8 illustrate the error in extracting the material parameters assuming the cross section of the waveguide is completely filled but actually having an air gap along the short wall. The air gap is .002". As anticipated, the error is very small or essentially zero since the electric field in the air gap is polarized parallel to a conducting boundary and hence is very small.

Figures 3.9 and 3.10 illustrate the error in extracting the parameters assuming the dimension  $t = .490''$  for Geometry A but actually having an additional air gap of .002". The actual thickness of the material cross-section is  $t = .488''$ . The error here is greater compared to when the guide is nearly completely filled. The amount of error is more significant in the imaginary components of the material parameters with  $\epsilon$  reaching a maximum of about 7%. The error in the real components remains under 1%.

Note that, in general, error in the extracted parameters is increased where nulls occur in the S parameter data.

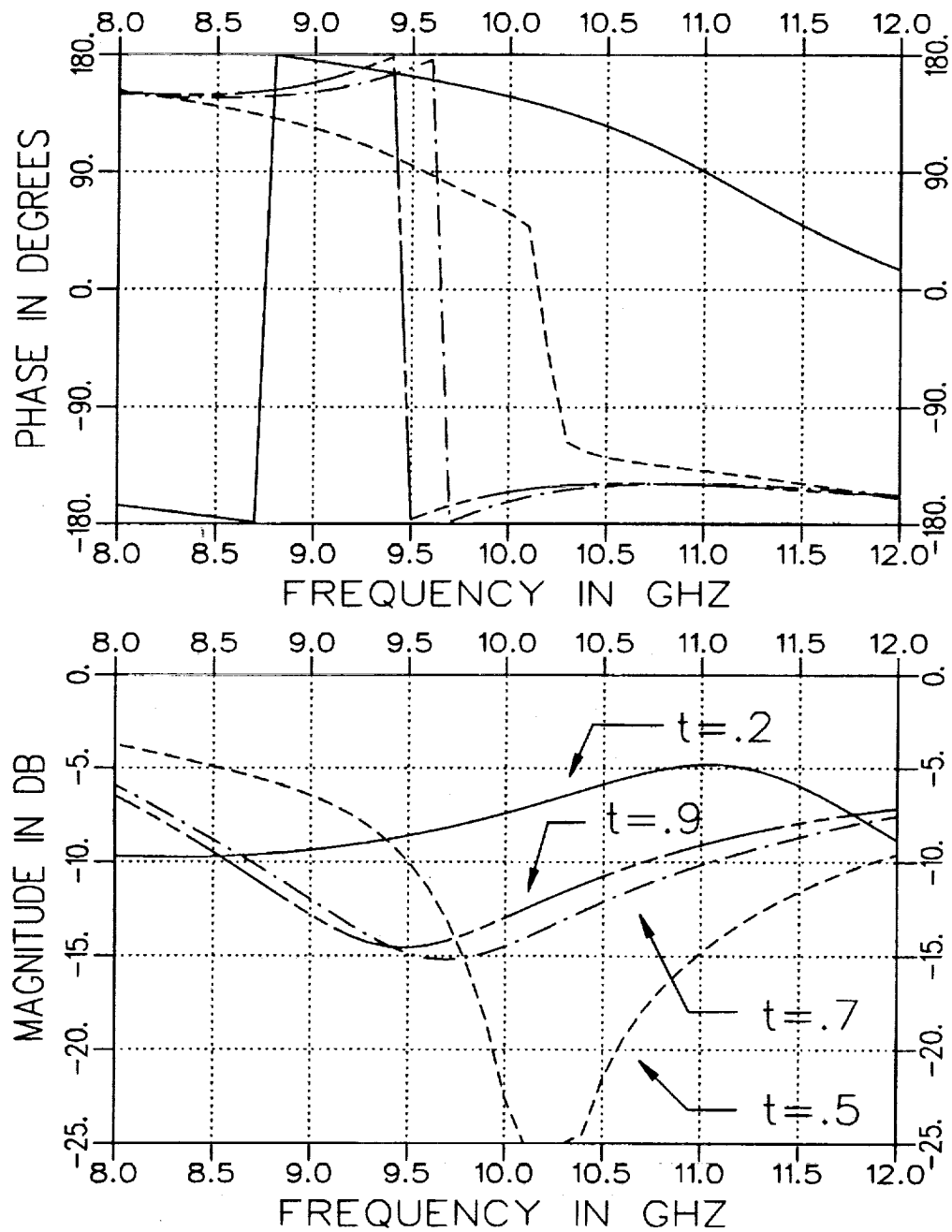


Figure 3.3: Calculated  $S_{11}$  for  $t = .2''$ ,  $.5''$ ,  $.7''$ , and  $.9''$  in an X-band fixture ( $.4'' \times .9''$ ) when  $\epsilon_r = (4.0, -j.20)$ ,  $\mu_r = (1.2, -j.12)$  and  $d = .3''$ . Geometry A.



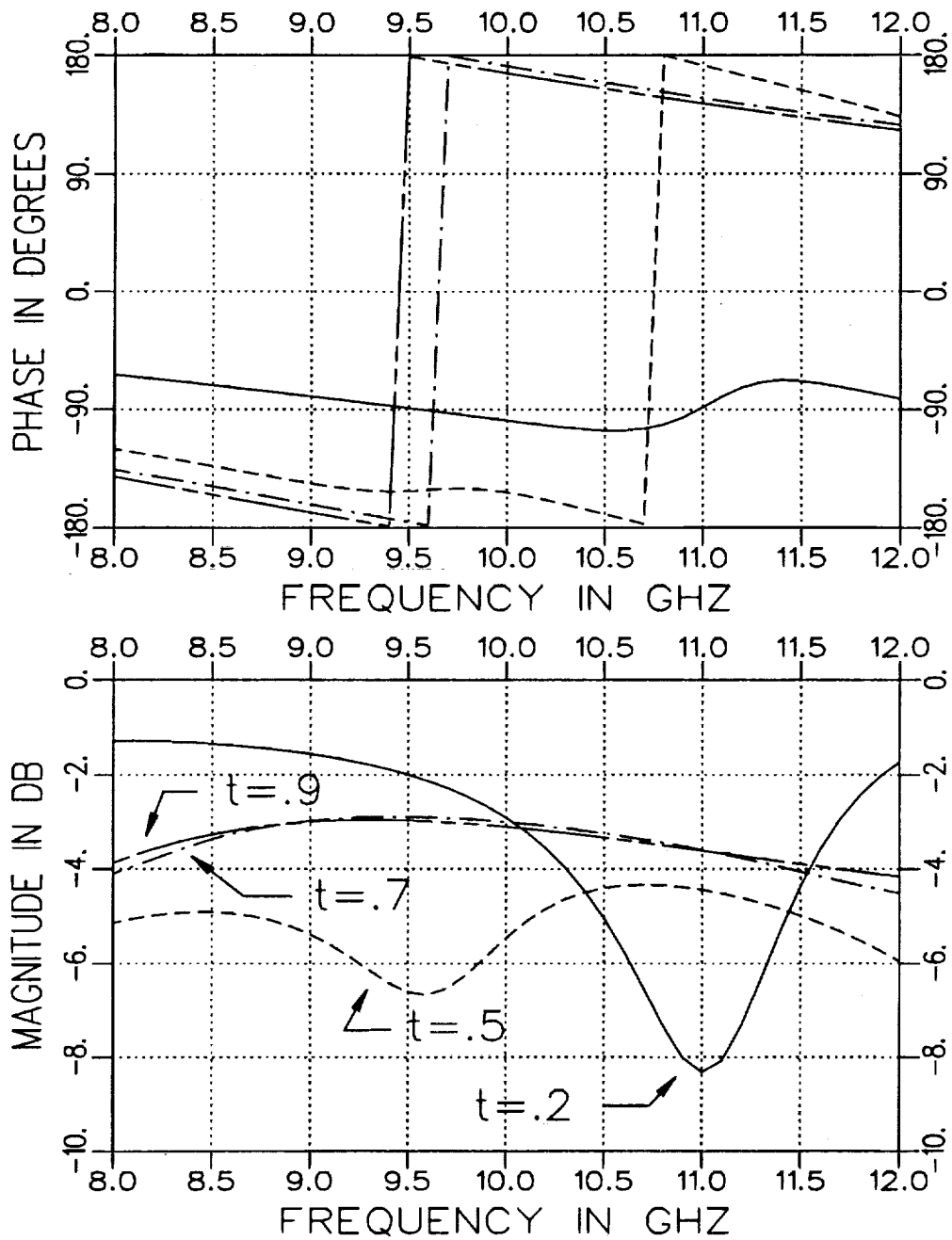


Figure 3.4: Calculated  $S_{21}$  for  $t = .2''$ ,  $.5''$ ,  $.7''$ , and  $.9''$  in an X-band fixture ( $.4'' \times .9''$ ) when  $\epsilon_r = (4.0, -j.20)$ ,  $\mu_r = (1.2, -j.12)$  and  $d = .3''$ . Geometry A.

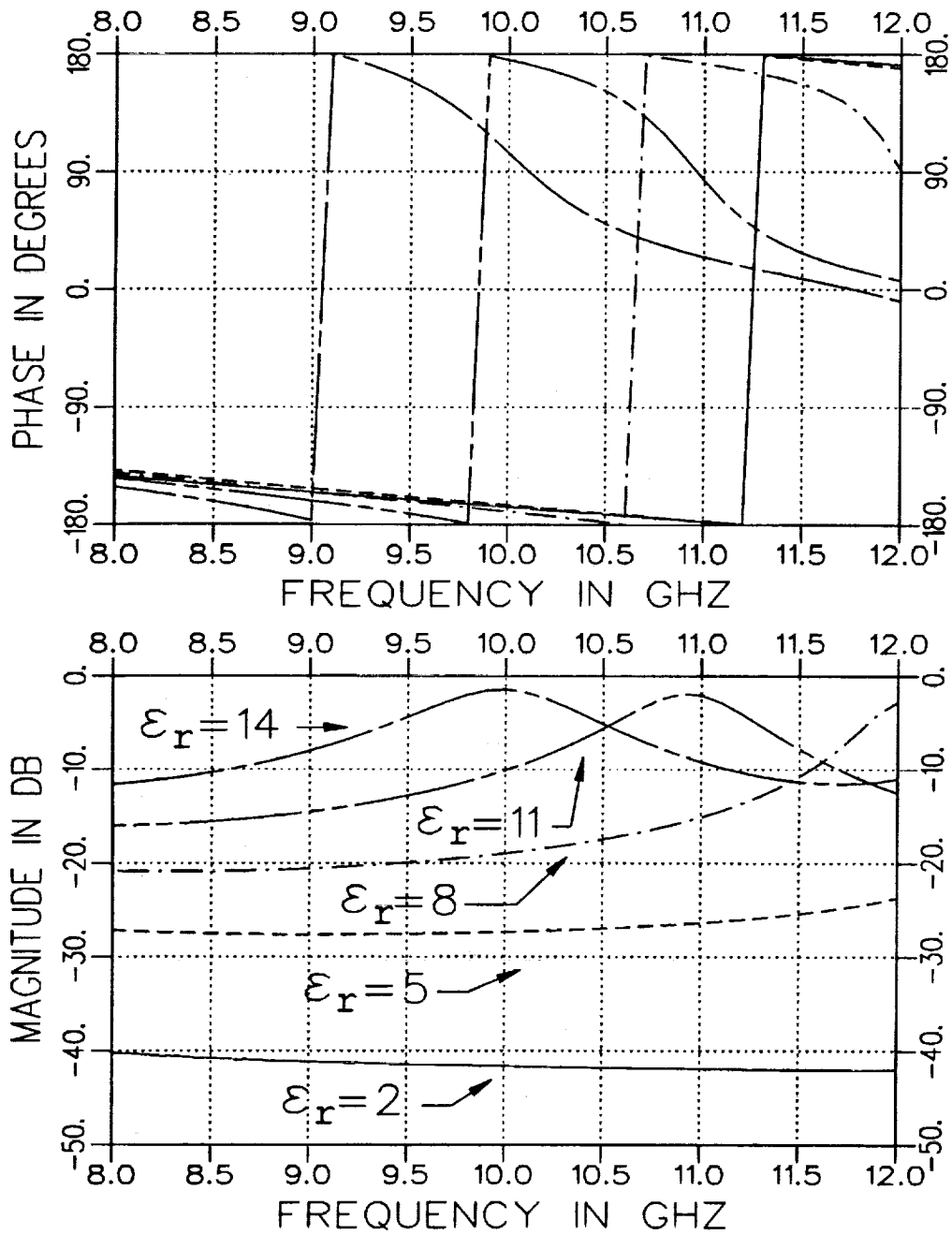


Figure 3.5: Calculated  $S_{11}$  for  $\epsilon_r = 2, 5, 8, 11,$  and  $14$  in an X-band fixture ( $.4'' \times .9''$ ) when  $\mu_r = (1., -j0.)$ ,  $t = .1''$  and  $d = .3''$ . Geometry A.

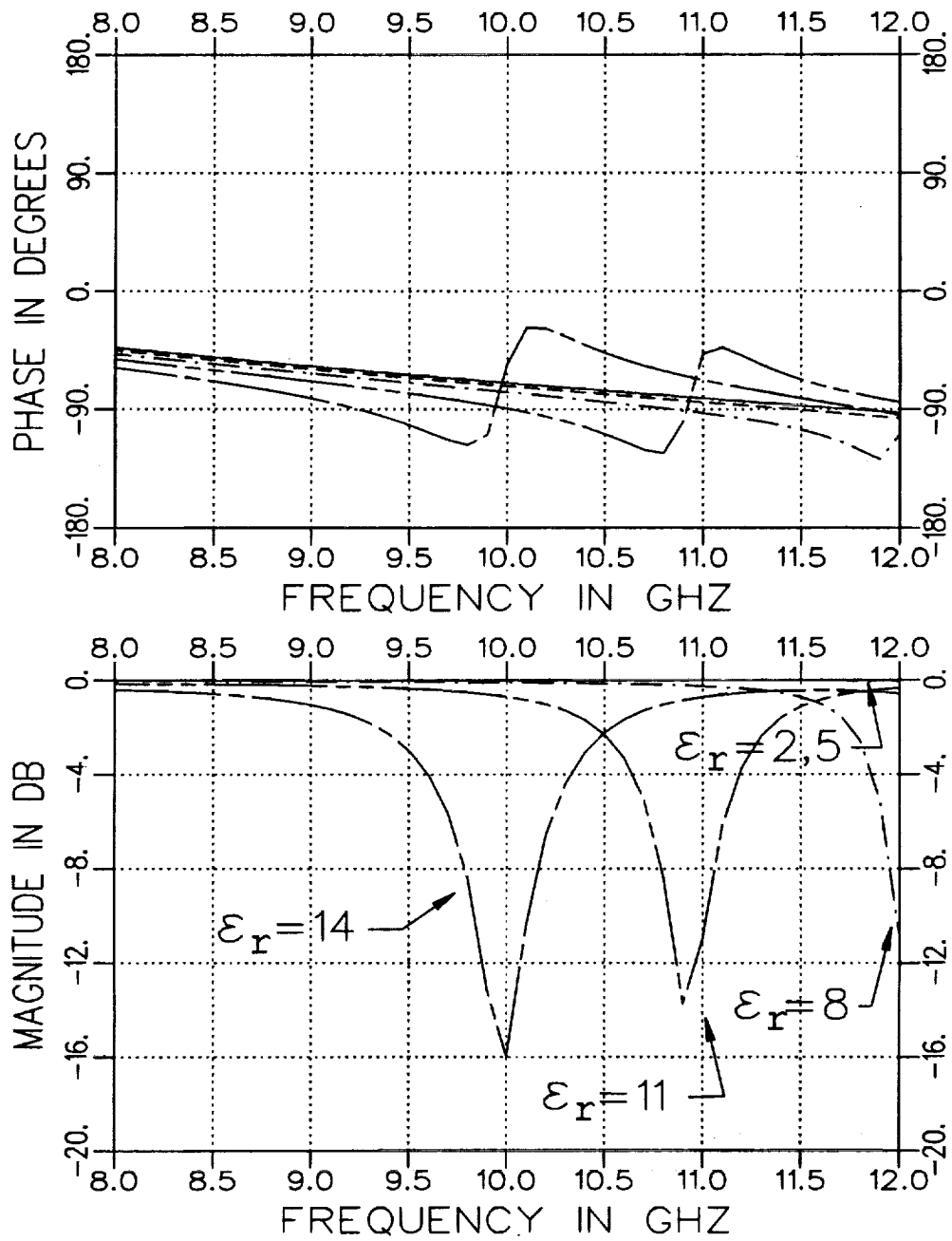


Figure 3.6: Calculated  $S_{21}$  for  $\epsilon_r = 2, 5, 8, 11,$  and  $14$  in an X-band fixture ( $.4'' \times .9''$ ) when  $\mu_r = (1., -j0.)$ ,  $t = .1''$  and  $d = .3''$ . Geometry A.

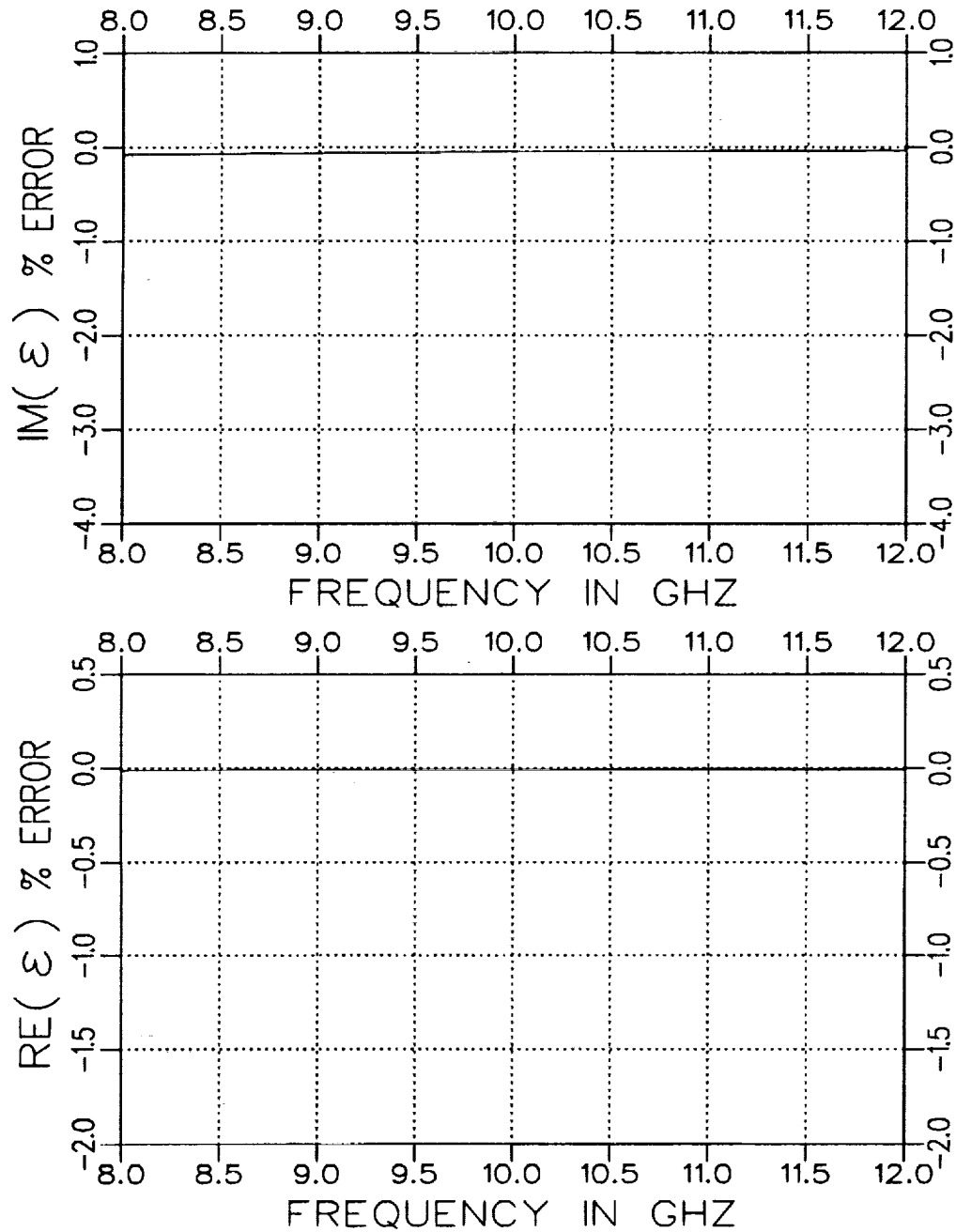


Figure 3.7: Normalized error in  $\epsilon$  for an .002" air gap along the short wall for a rectangular guide with  $\epsilon_r = (4.0, -j.20)$ ,  $\mu_r = (1.2, -j.12)$  and  $d = .156''$ . Geometry A but assumed completely filled.

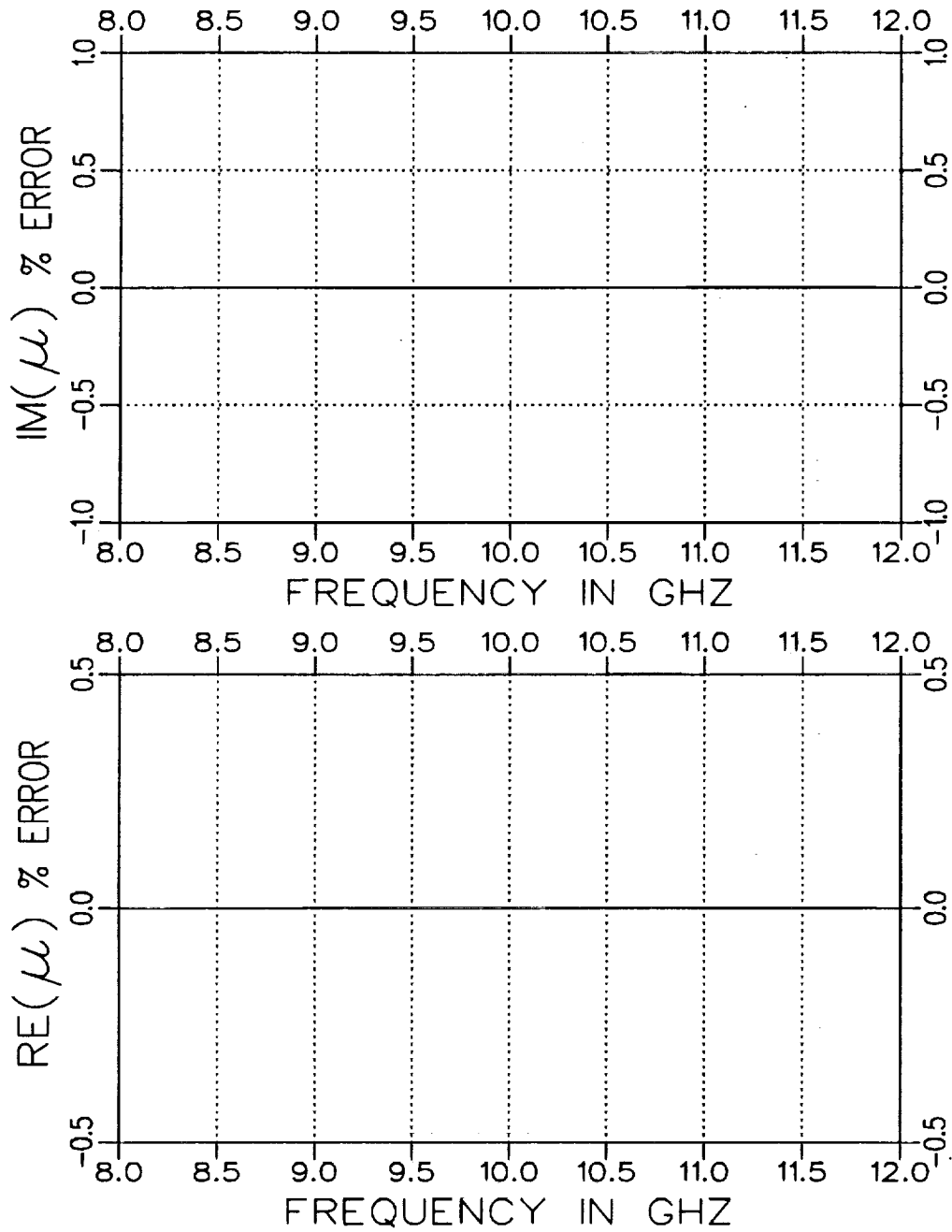


Figure 3.8: Normalized error in  $\mu$  for an .002" air gap along the short wall for a rectangular guide with  $\epsilon_r = (4.0, -j.20)$ ,  $\mu_r = (1.2, -j.12)$  and  $d = .156''$ . Geometry A but assumed completely filled.

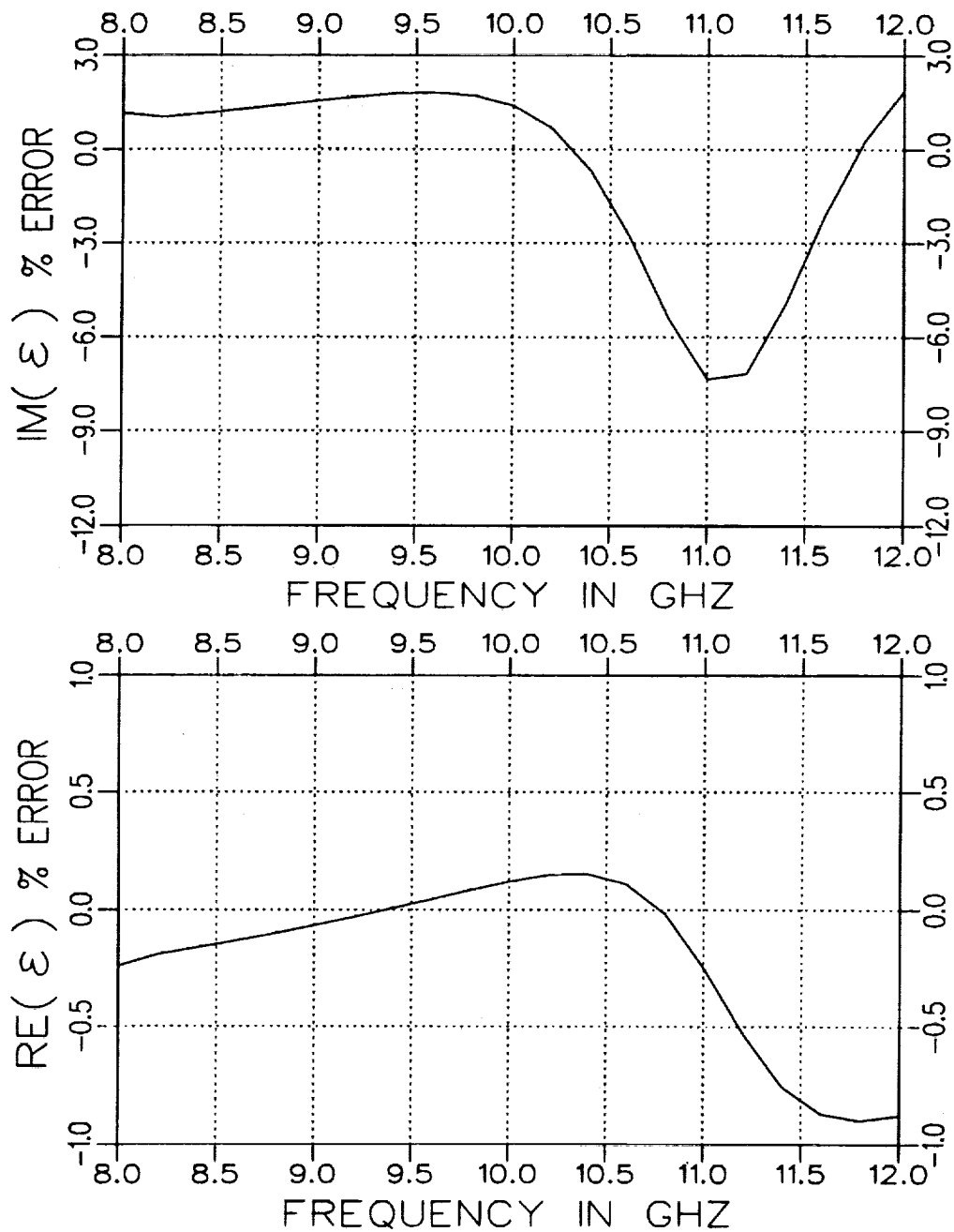


Figure 3.9: Normalized error in  $\epsilon$  for an additional .002" air gap along the short wall for a rectangular guide with  $\epsilon_r = (4.0, -j.20)$ ,  $\mu_r = (1.2, -j.12)$ ,  $d = .156''$  and assumed  $t = .490''$ . Geometry A.

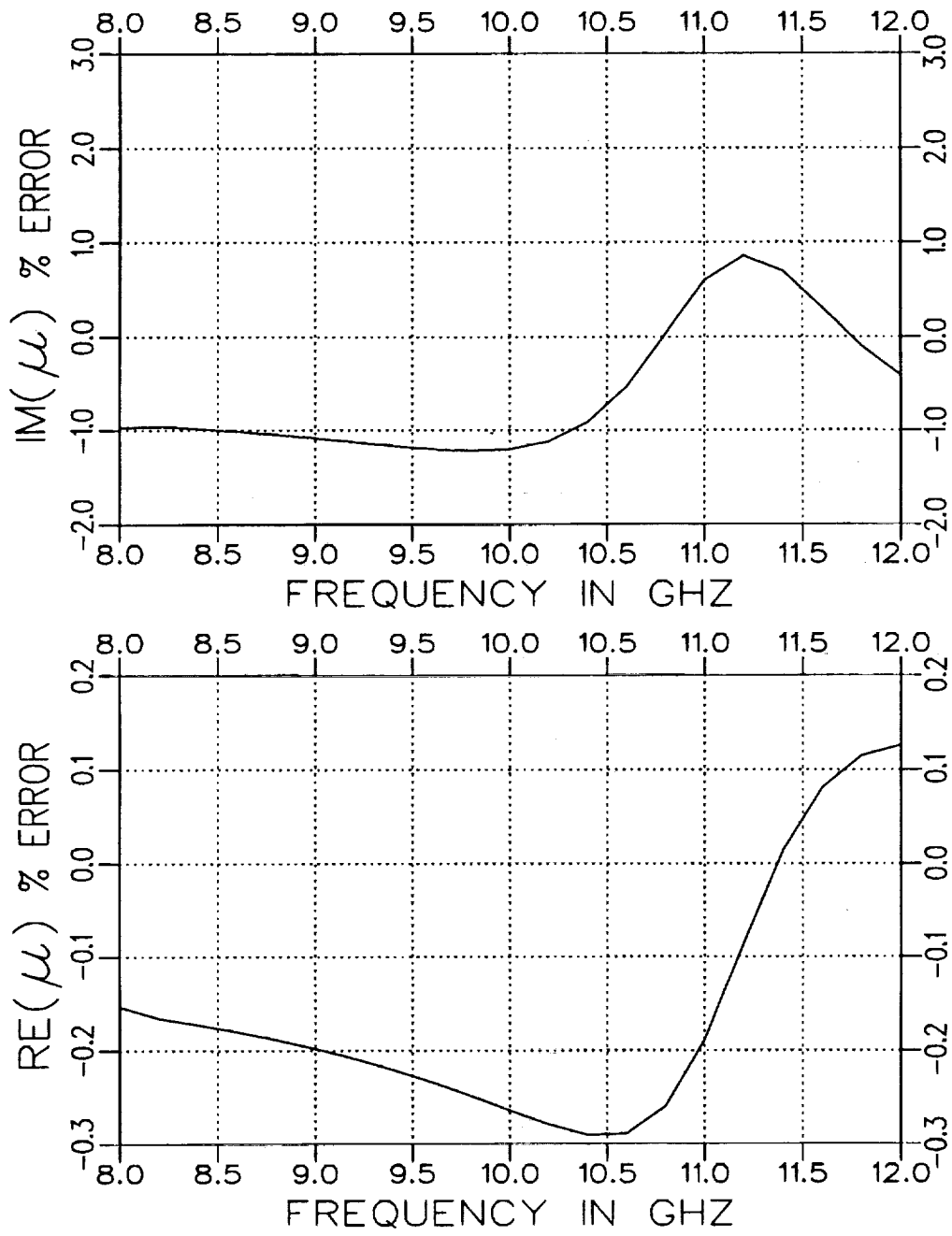


Figure 3.10: Normalized error in  $\mu$  for an additional .002" air gap along the short wall for a rectangular guide with  $\epsilon_r = (4.0, -j.20)$ ,  $\mu_r = (1.2, -j.12)$ ,  $d = .156$ " and assumed  $t = .490$ ". Geometry A.

### III.2 Geometry B

In this section Geometry B will now be considered. Figures 3.11 and 3.12 illustrate  $S_{11}$  and  $S_{21}$  for  $t = .05''$ ,  $.1''$ ,  $.2''$ ,  $.3''$  and  $.4''$  in an X-band fixture ( $.4'' \times .9''$ ) when  $\epsilon_r = (4.0, -j.20)$ ,  $\mu_r = (1.2, -j.12)$  and  $d = .3''$ . In contrast to Geometry A, the variation in  $S_{11}$  and  $S_{21}$  remains somewhat sensitive as the guide becomes completely filled. This indicates that a small air gap along the long wall may still be critical.

Figures 3.13 and 3.14 illustrate  $S_{11}$  and  $S_{21}$  for  $\epsilon_r = 2, 5, 8, 11$ , and  $14$  in an X-band fixture ( $.4'' \times .9''$ ) when  $\mu_r = (1., -j0.)$ ,  $t = .1''$  and  $d = .5''$ . The variation of the S parameters for Geometry B is similar to that of Geometry A.  $S_{11}$  is very sensitive to any loading and  $S_{21}$  would vary more if loss were present in the sample.

Figures 3.15 and 3.16 illustrate the error in extracting the material parameters assuming the cross section of the waveguide is completely filled but actually having an air gap along the long wall. The air gap is  $.002''$ . It is seen that the error is significantly larger than if the air gap is along the shorter wall. Whereas the error for an air gap along the shorter wall is essentially zero (see Figures 3.7 and 3.8), the air gap along the long wall for this case creates a maximum error of 3.5% in  $\text{Im}(\epsilon)$ . This is significant in that when one desires to make measurements with a completely-filled guide, a small unintended air gap along the long wall will alter the expected S parameter measurements which increases the difficulty in extracting accurate constitutive parameters.

Figures 3.17 and 3.18 illustrate the error in extracting the parameters assuming  $t = .300''$  but actually having an additional air gap of  $.002''$  along



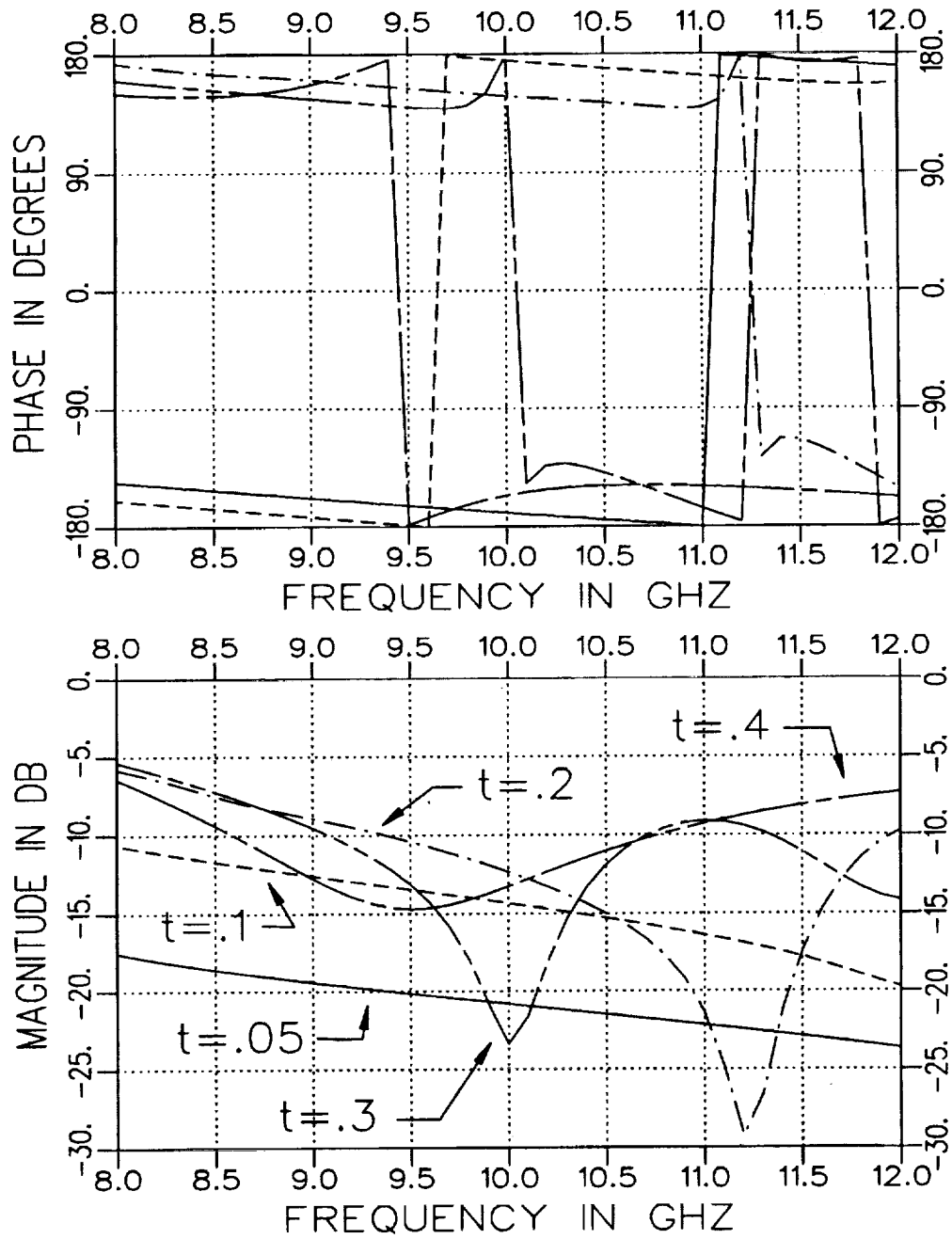


Figure 3.11: Calculated  $S_{11}$  for  $t = .05''$ ,  $.1''$ ,  $.2''$ ,  $.3''$  and  $.4''$  in an X-band fixture ( $.4'' \times .9''$ ) when  $\epsilon_r = (4.0, -j.20)$ ,  $\mu_r = (1.2, -j.12)$  and  $d = .3''$ . Geometry B.

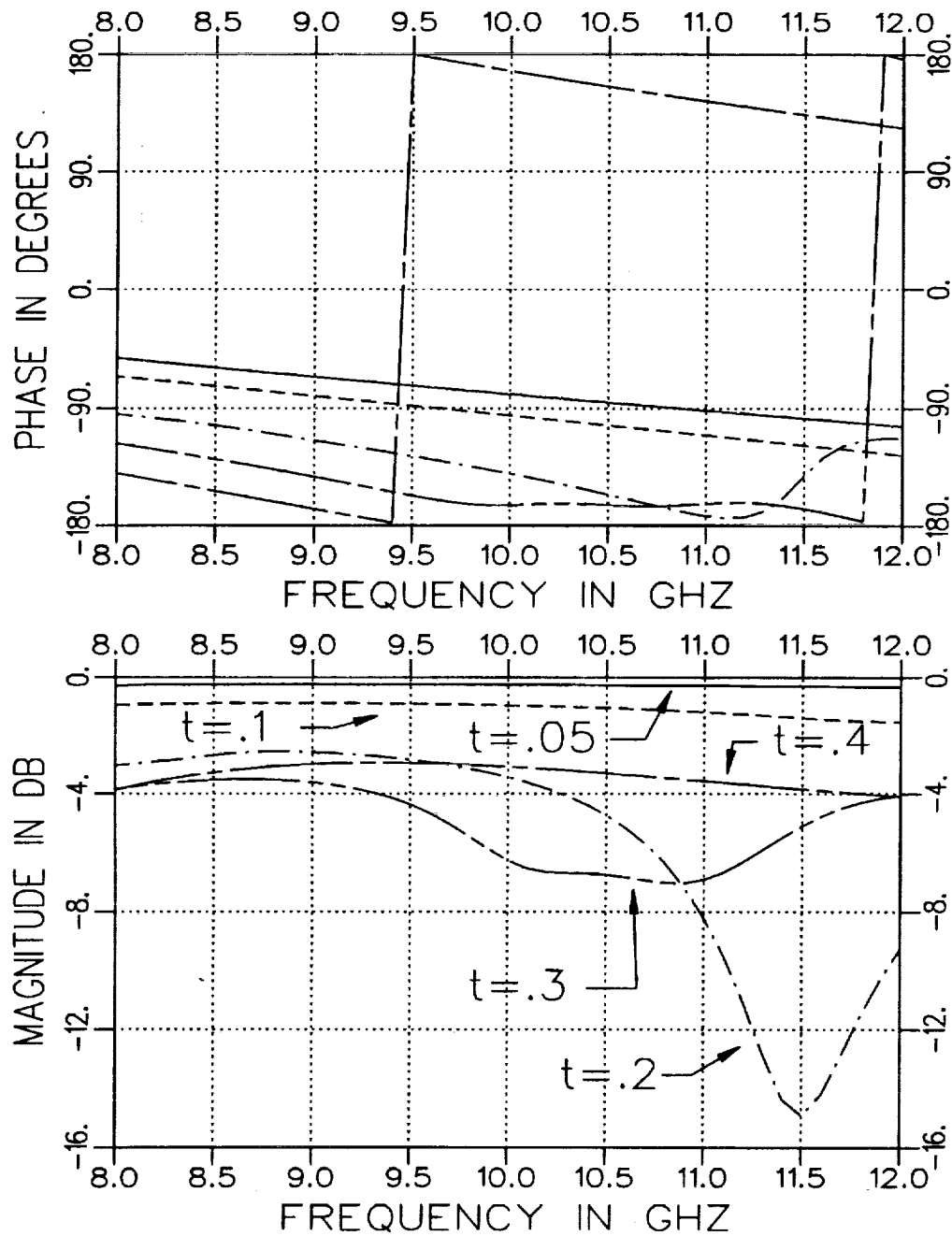


Figure 3.12: Calculated  $S_{21}$  for  $t = .05''$ ,  $.1''$ ,  $.2''$ ,  $.3''$  and  $.4''$  in an X-band fixture ( $.4'' \times .9''$ ) when  $\epsilon_r = (4.0, -j.20)$ ,  $\mu_r = (1.2, -j.12)$  and  $d = .3''$ . Geometry B.

the long wall. The actual thickness of the material was  $t = .298''$ . It is seen that the error can be very large for both the extracted  $\epsilon$  and  $\mu$  parameters, particularly in the imaginary components. In the lower end of the frequency band (under 10 GHz), the error in  $\text{Re}(\epsilon)$  is slightly less than the error when the guide is nearly filled while the error in  $\mu$  remained about the same. It is anticipated that the most accurate parameter extraction for a partially-filled waveguide occurs when the thickness of the sample along the shorter wall is chosen such that the S parameters have the smallest dependency upon  $t$  while keeping the dimension of the sample along the longer wall as large as possible. In this case, the sample thickness was not chosen to minimize the extraction error.

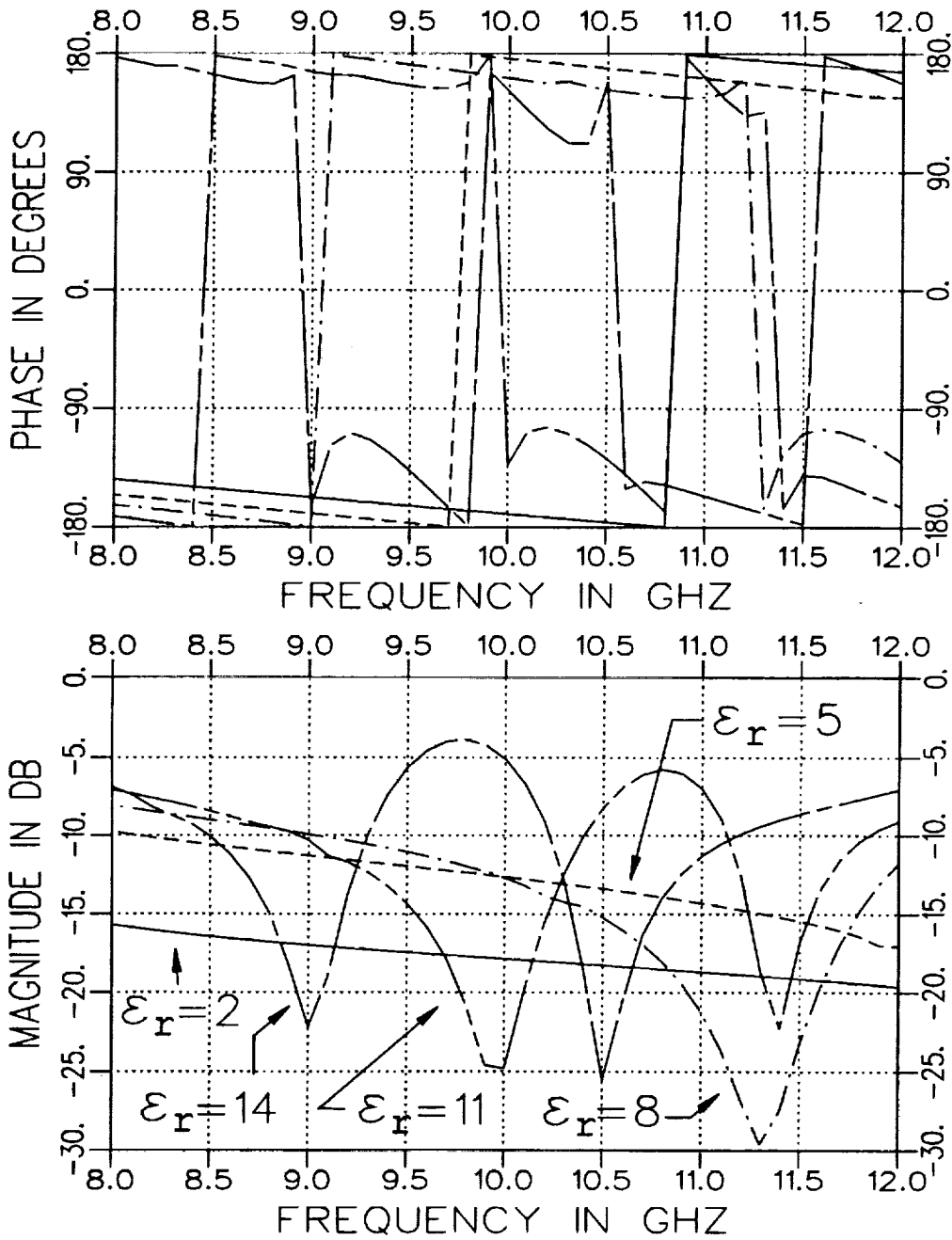


Figure 3.13: Calculated  $S_{11}$  for  $\epsilon_r = 2, 5, 8, 11,$  and  $14$  in an X-band fixture ( $.4'' \times .9''$ ) when  $\mu_r = (1., -j0.), t = .1''$  and  $d = .5''$ . Geometry B.

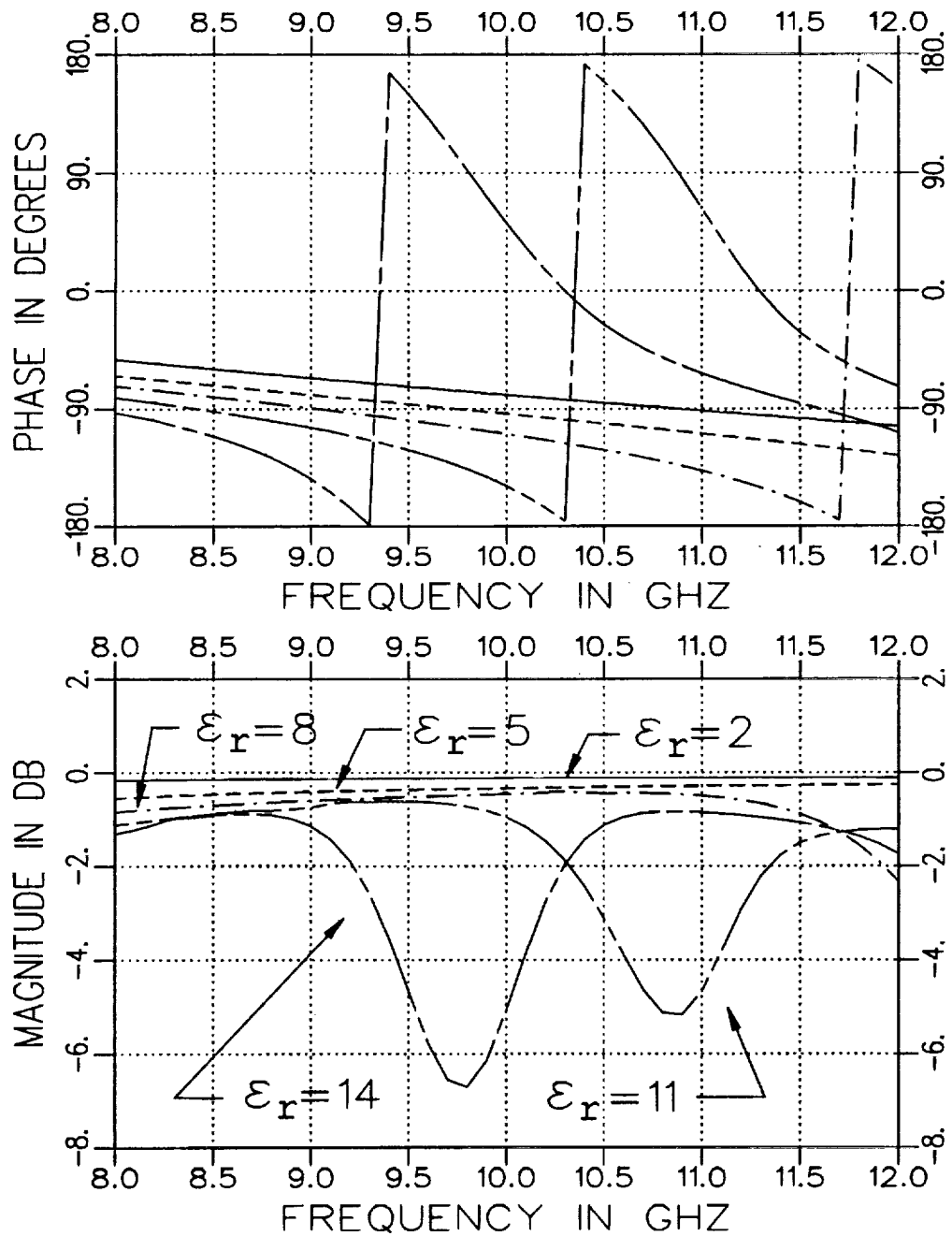


Figure 3.14: Calculated  $S_{21}$  for  $\epsilon_r = 2, 5, 8, 11,$  and  $14$  in an X-band fixture ( $.4'' \times .9''$ ) when  $\mu_r = (1., -j0.)$ ,  $t = .1''$  and  $d = .5''$ . Geometry B.

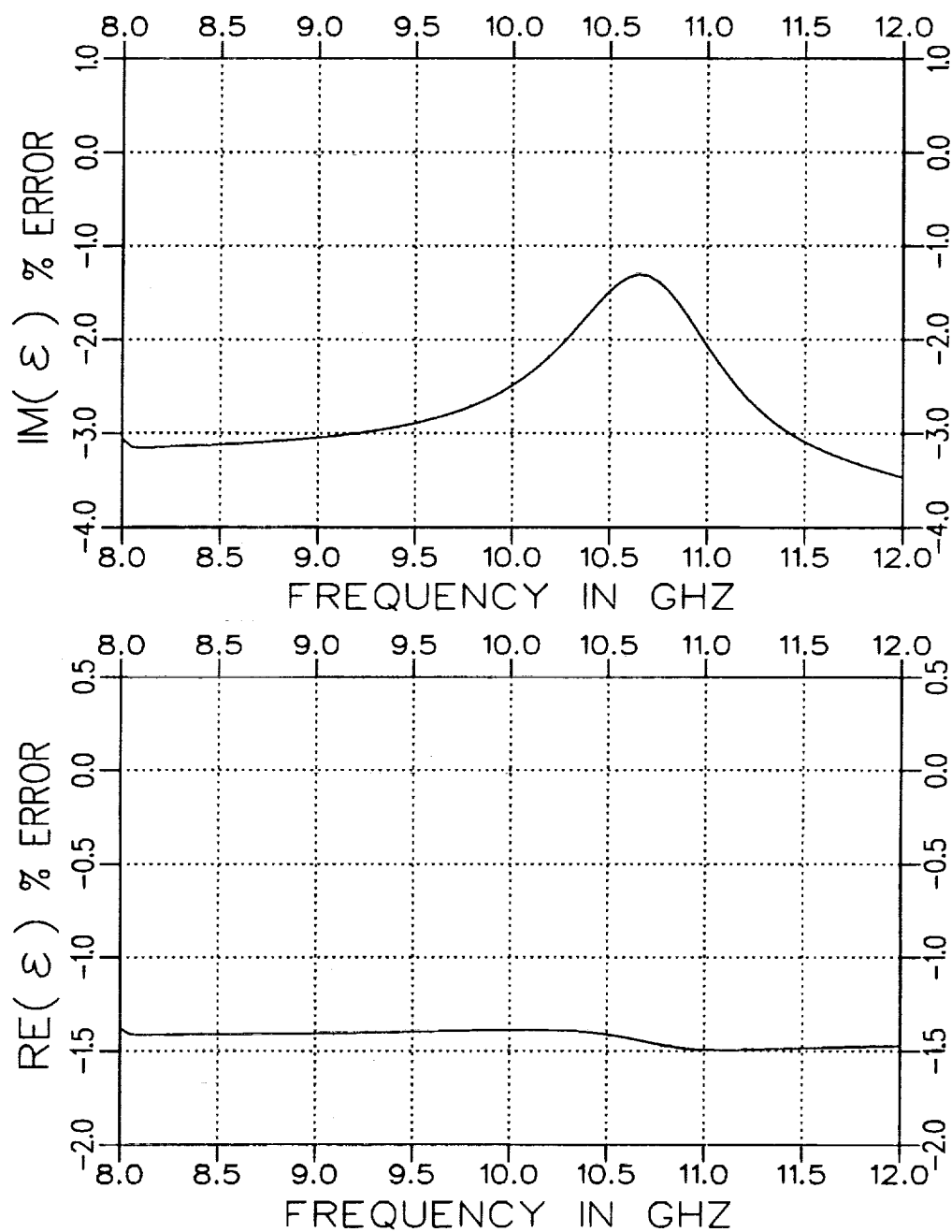


Figure 3.15: Normalized error in  $\epsilon$  for an .002" air gap along the short wall for a rectangular guide with  $\epsilon_r = (4.0, -j.20)$ ,  $\mu_r = (1.2, -j.12)$  and  $d = .165"$ . Geometry B but assumed completely filled.

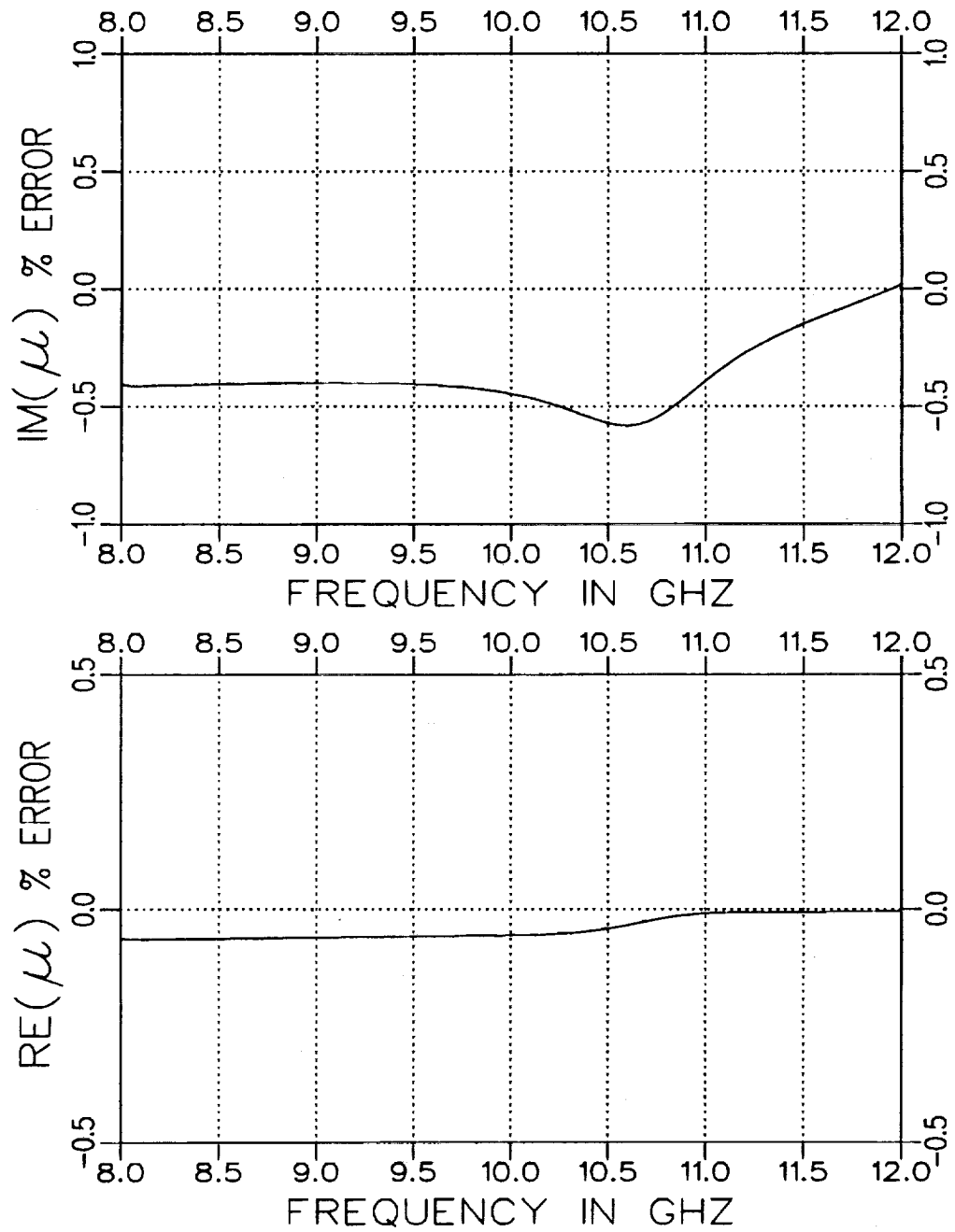


Figure 3.16: Normalized error in  $\mu$  for an .002" air gap along the long wall for a rectangular guide with  $\epsilon_r = (4.0, -j.20)$ ,  $\mu_r = (1.2, -j.12)$  and  $d = .156$ ". Geometry B but assumed completely filled.

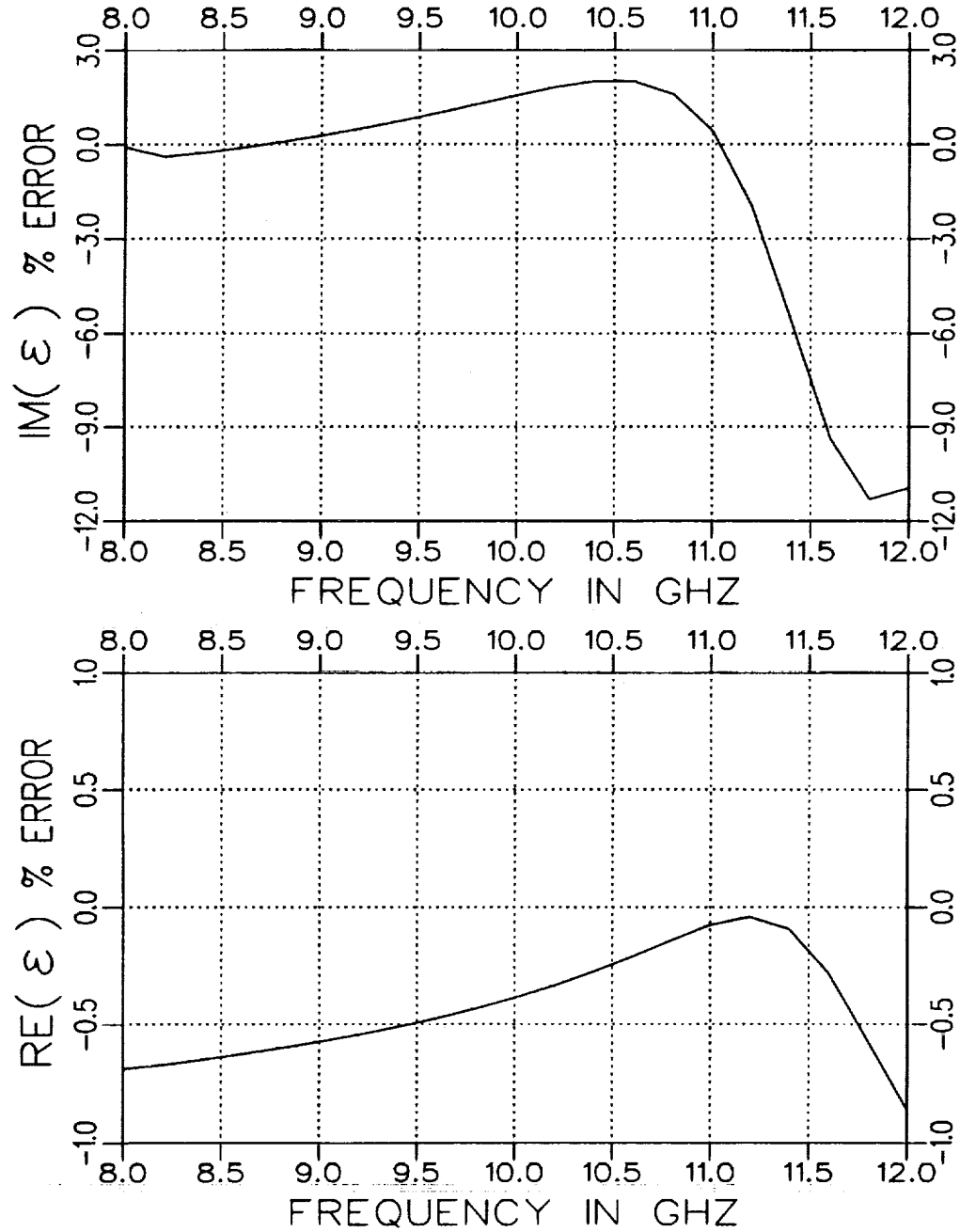


Figure 3.17: Normalized error in  $\epsilon$  for an additional .002" air gap along the long wall for a rectangular guide with  $\epsilon_r = (4.0, -j.20)$ ,  $\mu_r = (1.2, -j.12)$ ,  $d = .156$ " and assumed  $t = .300$ ". Geometry B.



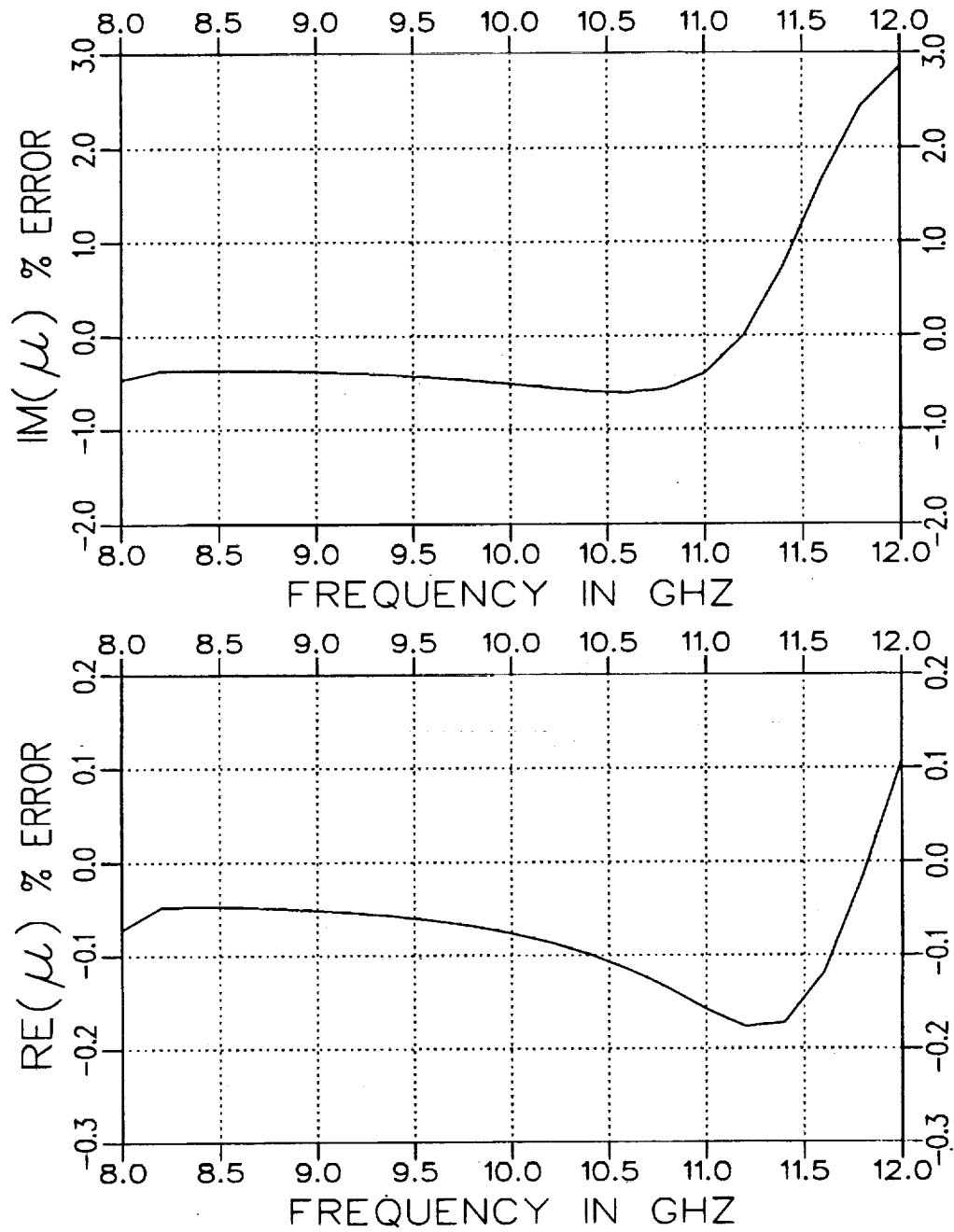


Figure 3.18: Normalized error in  $\mu$  for an additional .002" air gap along the long wall for a rectangular guide with  $\epsilon_r = (4.0, -j.20)$ ,  $\mu_r = (1.2, -j.12)$ ,  $d = .156''$  and assumed  $t = .300''$ . Geometry B.

## Chapter 4

# Parameter Extraction

The reflection and transmission characteristics of material samples in transmission line fixtures allow the extraction of the constitutive parameters for the material. As indicated in Chapter 2, simple closed-form expressions exist when the fixture cross section is completely filled in the sample region. The only requirement on sample dimension is that the length should not be in the region of  $\lambda_g/2$  to avoid nulls in the reflection measurement. The presence of a null can potentially result in error due to a poor signal-to-noise ratio.

The parameter extraction process is not as simple when the cross section of the sample region is not completely filled. An iterative procedure has to be initiated to acquire the constitutive parameters as indicated in Chapter 3. This is a result of many modes being generated to satisfy the required boundary conditions in the sample region. As before, the sample dimensions should not be in the vicinity of  $\lambda_g/2$  to produce a null in the reflected field. The guide wavelength of a partially-filled fixture is also dependent upon the sample thickness in the cross section plane as well as the constitutive parameters of the sample. The sample thickness should be sufficient to produce  $S_{11}$  and  $S_{21}$  parameters with comparable dynamic range. This occurrence will minimize the possibility of the reflected and

transmitted fields not sensing the material sufficiently. It would be undesirable to extract constitutive parameters from measurements when the reflected signal is too close to zero or the transmitted signal is too close to unity. Reasonable choices for sample thickness and length can be obtained from parameter studies as illustrated in Figures 4.1 through 4.4 as well as Figures 3.3 through 3.6 and 3.11 through 3.14.

Note that in Figure 4.3 the amplitude as well as the phase of the  $S_{11}$  parameter changes significantly when the waveguide is nearly completely filled ( $t \approx 0.4''$ ) for Geometry B. This indicates that one should avoid taking measurements for the completely-filled case as a small, undesired air gap along the longer waveguide wall would significantly alter the values of the S parameters. This in turn would hinder the accuracy of the extraction process of the constitutive parameters. As long as the air gap is large enough and in the range of  $t$  where both S parameters do not fluctuate greatly, parameter extraction ought to be accurate. Also it may be assumed that when taking measurements in the Geometry A configuration, significant error in the measured S parameters may occur because of a small unintended air gap along the long wall. This is the case when the dielectric sample is not sufficiently flush against the waveguide walls.

Geometry B may be the preferred geometry configuration provided that the air gap along the long wall is sufficiently large and a small error in  $t$  will not significantly change the S parameters. This is suggested in Figure 4.1 where it is seen that a small air gap along the short wall does not alter the S parameters as drastically as in Geometry B. Then it is assumed that any small unintended air gap along the short wall will not significantly affect the S parameter measurements and accurate parameter extraction should occur.

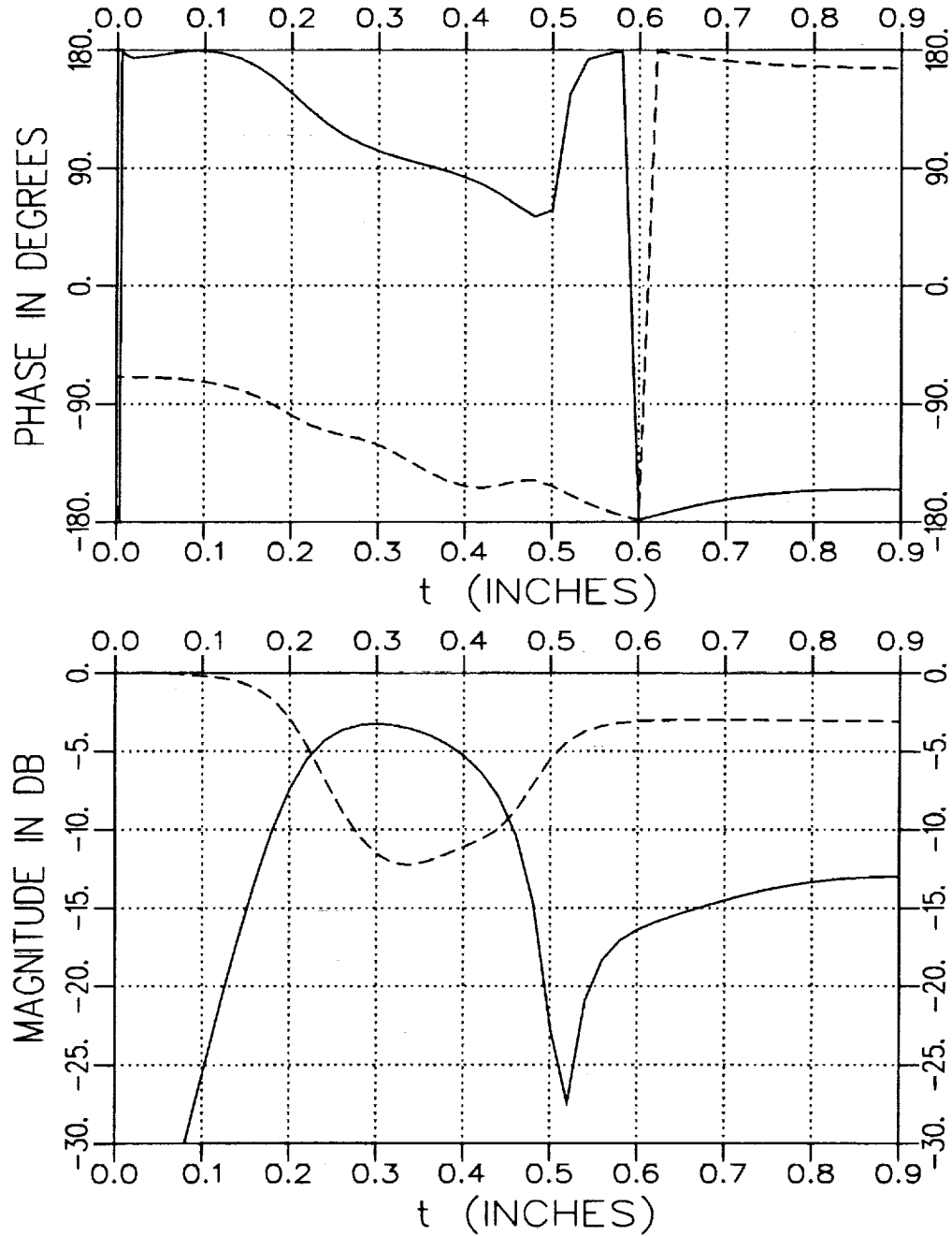


Figure 4.1: Calculated  $S_{11}$  (solid) and  $S_{21}$  (dashed) for varying  $t$  with  $\epsilon_r = (4.0, -j.20)$ ,  $\mu_r = (1.2, -j.12)$ ,  $d = .3''$  and  $f = 10$  GHz. Geometry A.

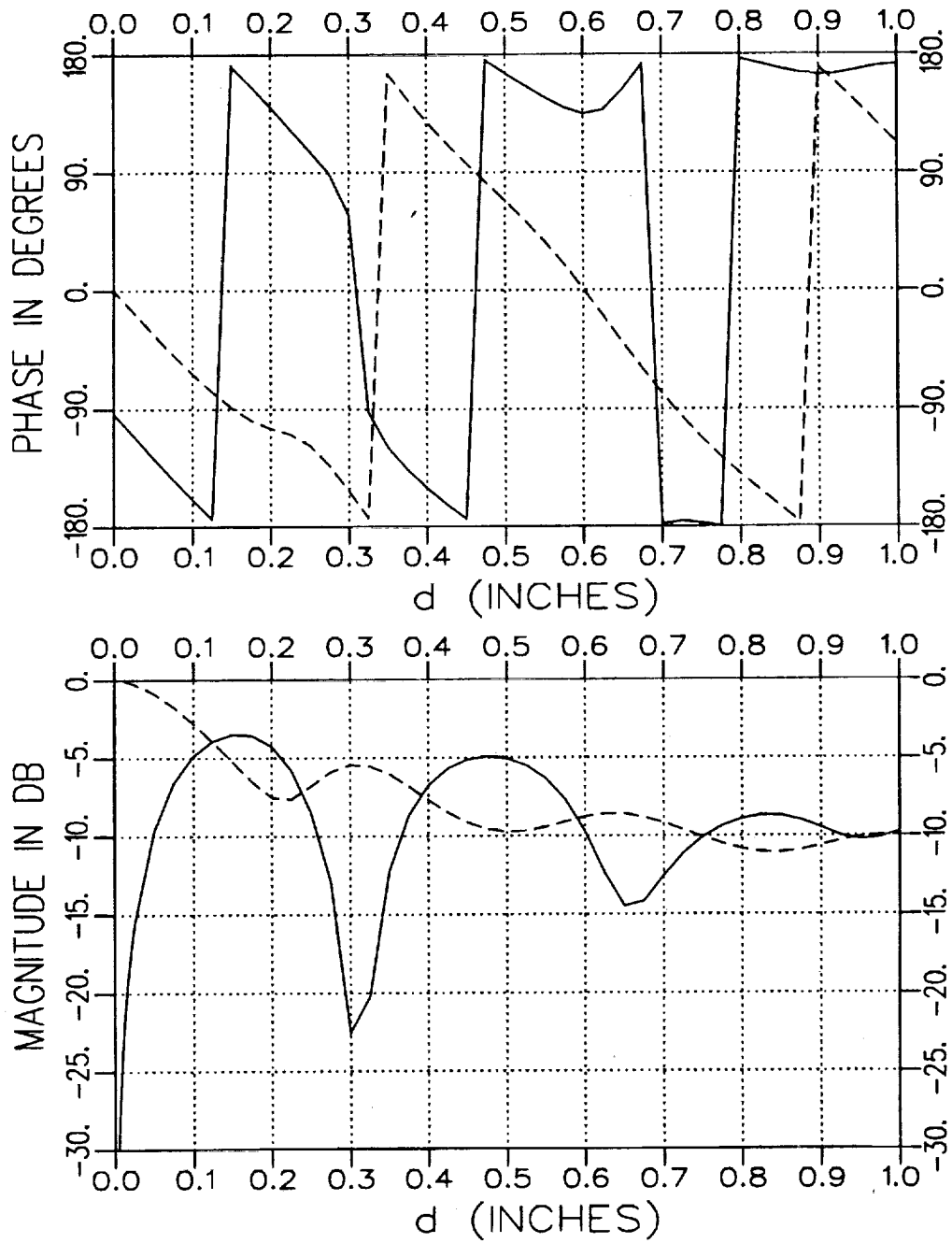


Figure 4.2: Calculated  $S_{11}$  (solid) and  $S_{21}$  (dashed) for varying  $d$  with  $\epsilon_r = (4.0, -j.20)$ ,  $\mu_r = (1.2, -j.12)$ ,  $t = .5''$  and  $f = 10$  GHz. Geometry A.

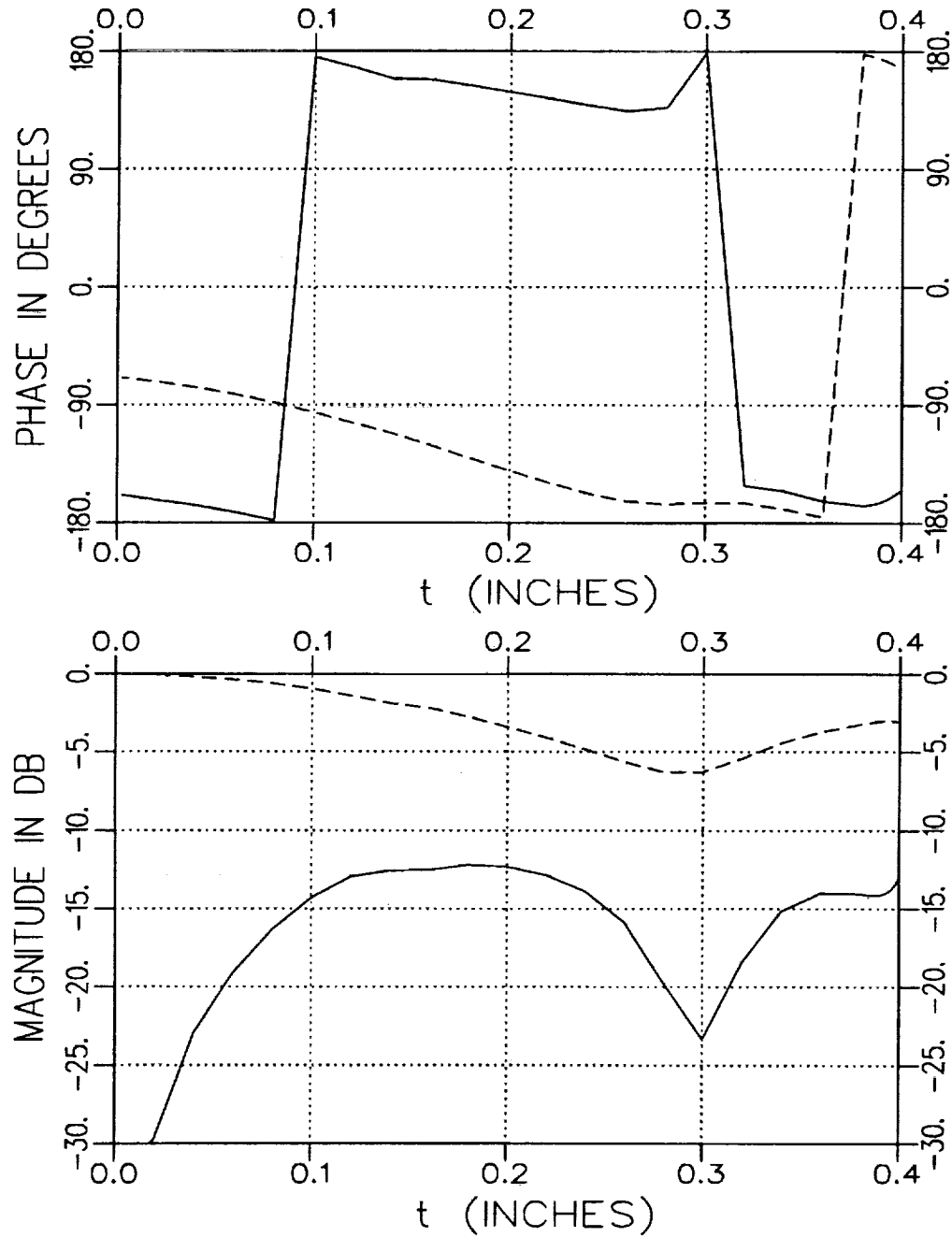


Figure 4.3: Calculated  $S_{11}$  (solid) and  $S_{21}$  (dashed) for varying  $t$  with  $\epsilon_r = (4.0, -j.20)$ ,  $\mu_r = (1.2, -j.12)$ ,  $d = .3''$  and  $f = 10$  GHz. Geometry B.

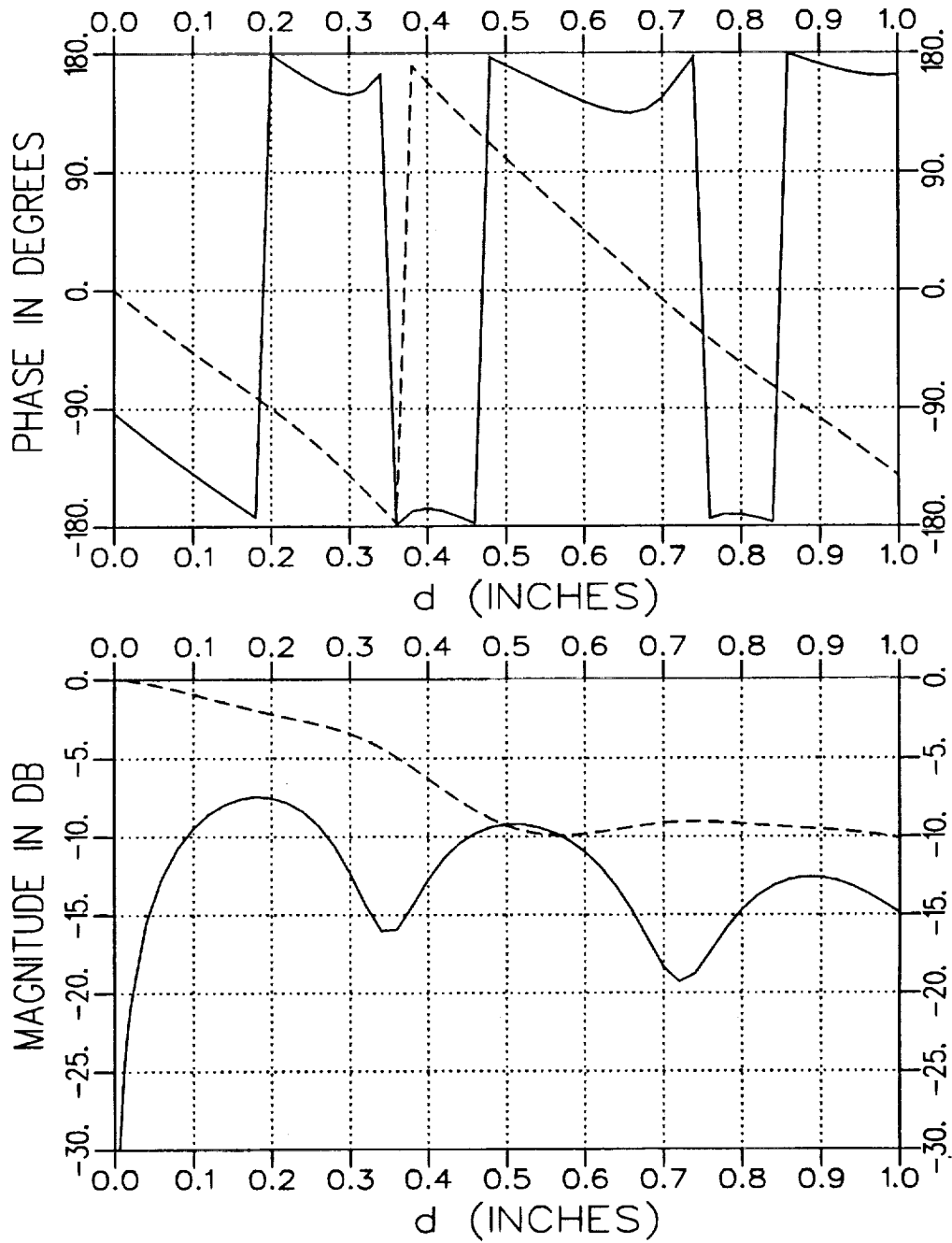


Figure 4.4: Calculated  $S_{11}$  (solid) and  $S_{21}$  (dashed) for varying  $d$  with  $\epsilon_r = (4.0, -j.20)$ ,  $\mu_r = (1.2, -j.12)$ ,  $t = .2''$  and  $f = 10$  GHz. Geometry B.

The following sections focus on the measured S parameters and extracted constitutive parameters for two different port configurations. The material sample used in these examples was measured using a coaxial fixture to obtain independent values for the constitutive parameters. These material parameter values are shown in Figures 4.5 and 4.6. Representative values for these parameters are  $\epsilon_r = (4.0, -j.20)$  and  $\mu_r = (1.2, -j.12)$  between 8 and 12 GHz. The samples were cut from a .156" thick slab of material and were appropriately positioned in the X-band fixture for the different geometry configurations. The fixture used is illustrated in Figure 4.7. The calibration technique applied to the measured S parameters is discussed in [9]. Note that an additional phase factor of  $e^{-jk_0 d}$  was applied to the  $S_{21}$ . This accounts for the apparent increase of the fixture length when the sample was inserted in the fixture. This phase factor is not required if the fixture length is physically increased by a sample holder.

Just how accurate the extracted parameters are depends, of course, on the level of error terms in the S parameter measurements. Figures 4.8 through 4.11 demonstrate how much the accuracy of the extracted constitutive parameters is affected by the level of error added to the S parameter data for both geometry configurations. The level of the error term added to the S parameters is defined to be

$$\text{ERROR LEVEL dB} = 20 \log_{10} |S_{ij}| \text{ERROR LEVEL}$$

It is seen that the percent error for the real part of complex  $\epsilon$  and  $\mu$  remains moderate as the error level increases. However for both geometries, the imaginary components of the extracted permittivity and permeability suffer greatly if the error level is not kept sufficiently low. Note that error levels



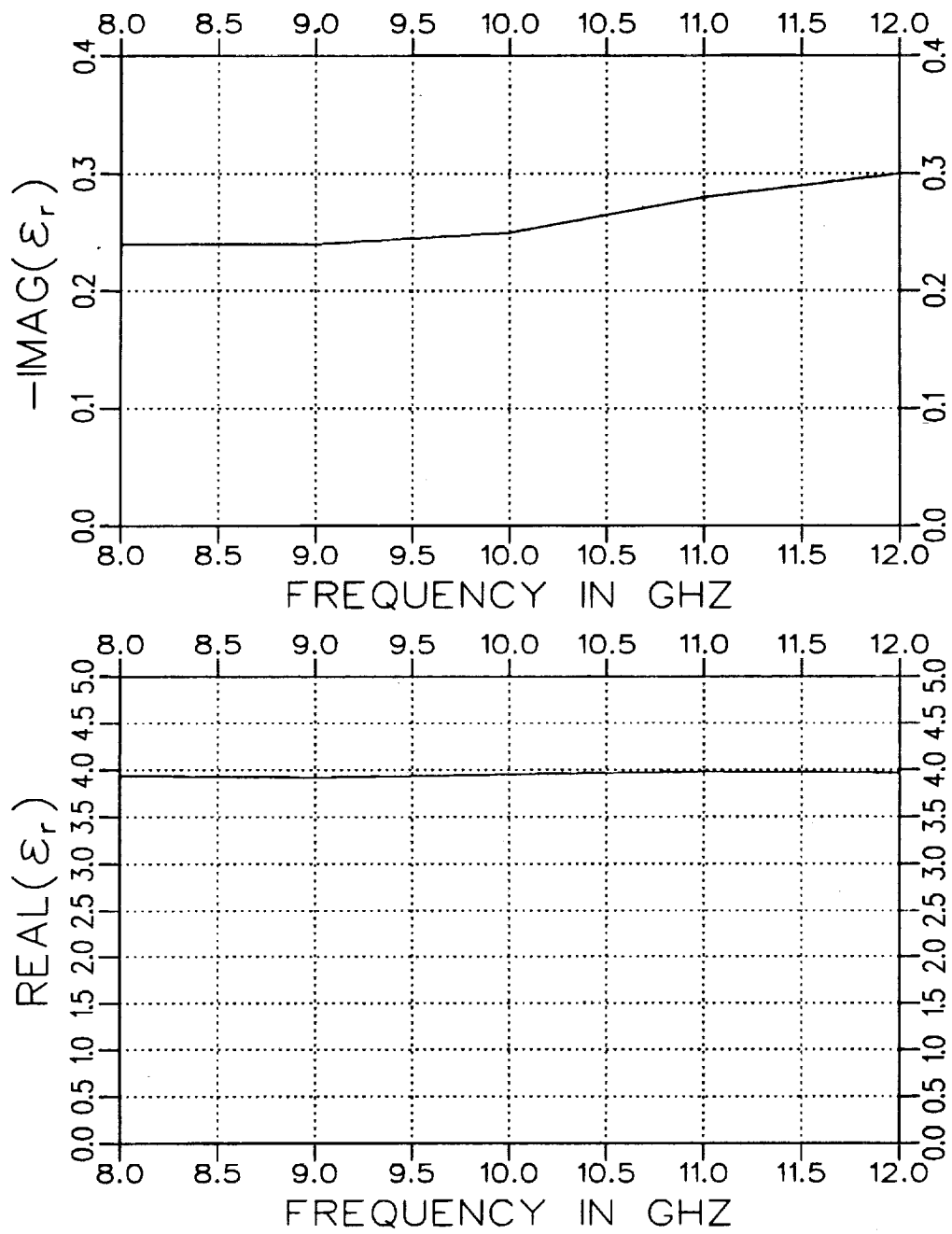


Figure 4.5:  $\epsilon_r$  values using a coaxial airline fixture.

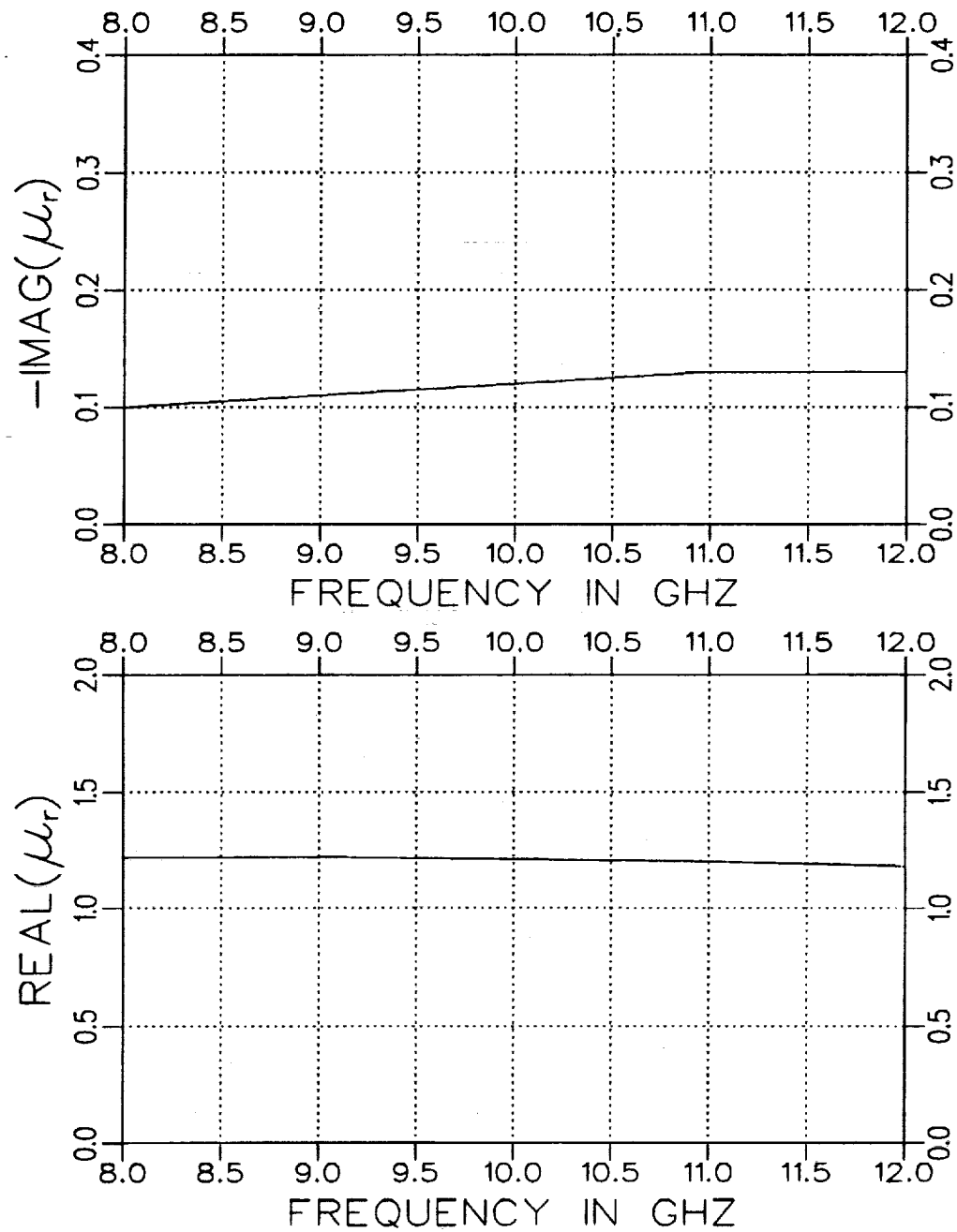


Figure 4.6:  $\mu_r$  values using a coaxial airline fixture.

ORIGINAL PAGE  
BLACK AND WHITE PHOTOGRAPH

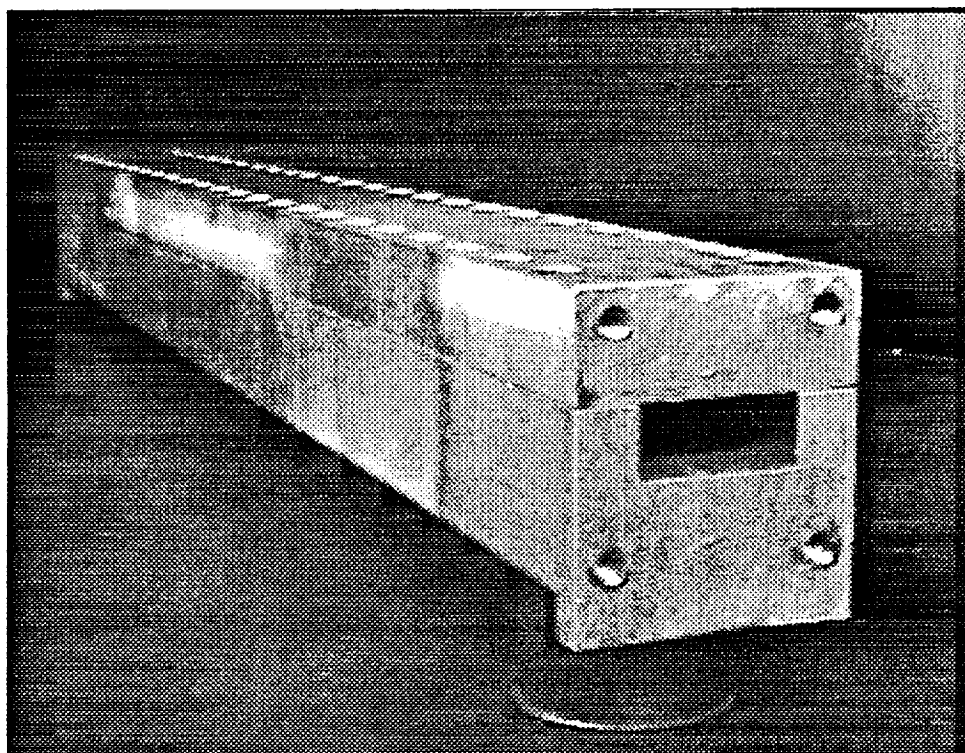


Figure 4.7: Illustration of X-band fixture used for material measurement.

ORIGINAL PAGE IS  
OF POOR QUALITY

of  $-20$  and  $-40$  dB represent S parameter error percentages of 10 and 1 percent, respectively. As seen before, a small error in the real part of an extracted parameter results in a large error in the imaginary part. The imaginary part of the material parameter is subject to larger errors because the real part of the material parameter is much larger than the imaginary part.

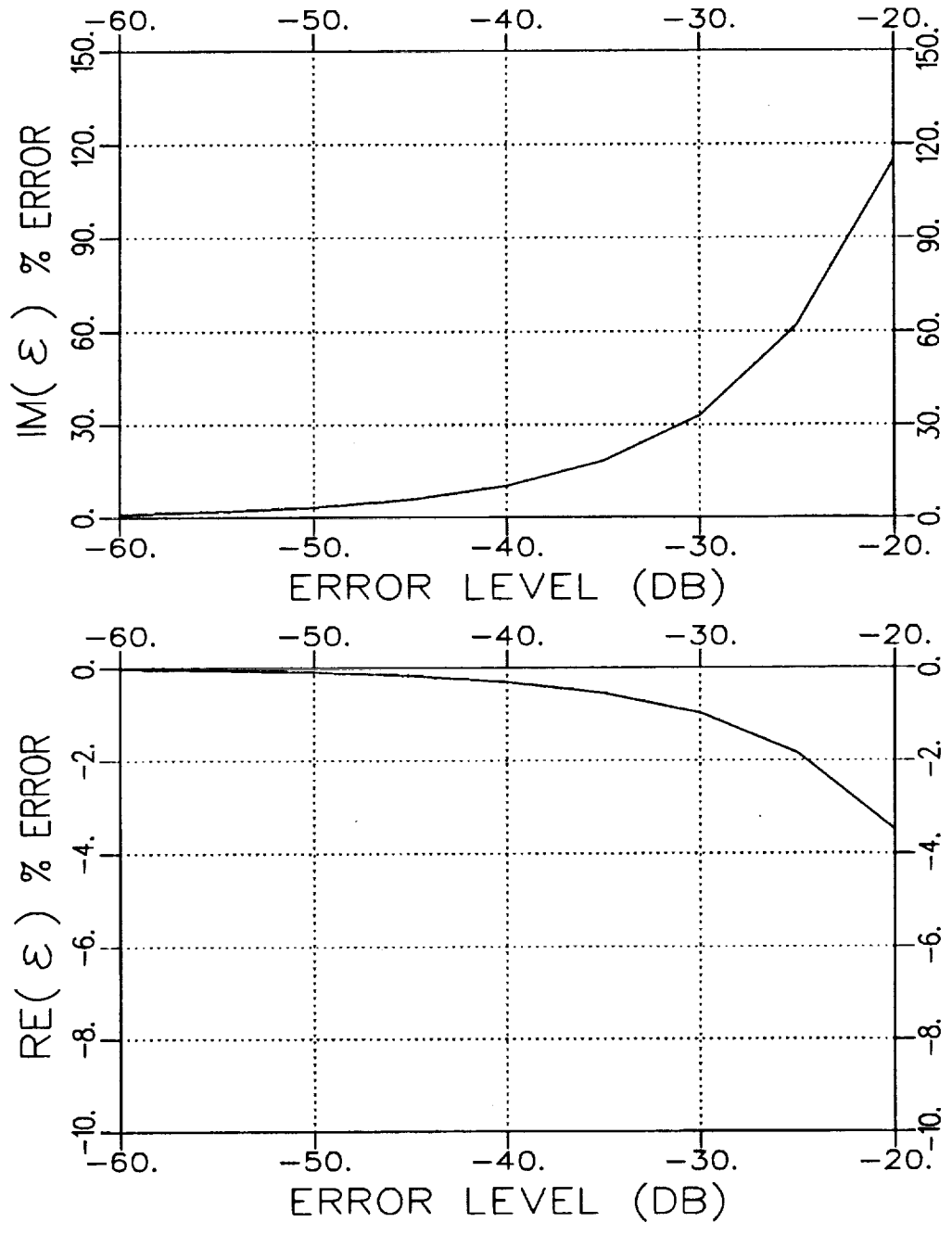


Figure 4.8: Normalized error in extracted permittivity vs. error level added to S parameters. Geometry A with  $\epsilon_r = (4.0, -j.20)$ ,  $\mu_r = (1.2, -j.12)$ ,  $t = .490''$ ,  $d = .156''$  and  $f = 10$  GHz in an X-band fixture.

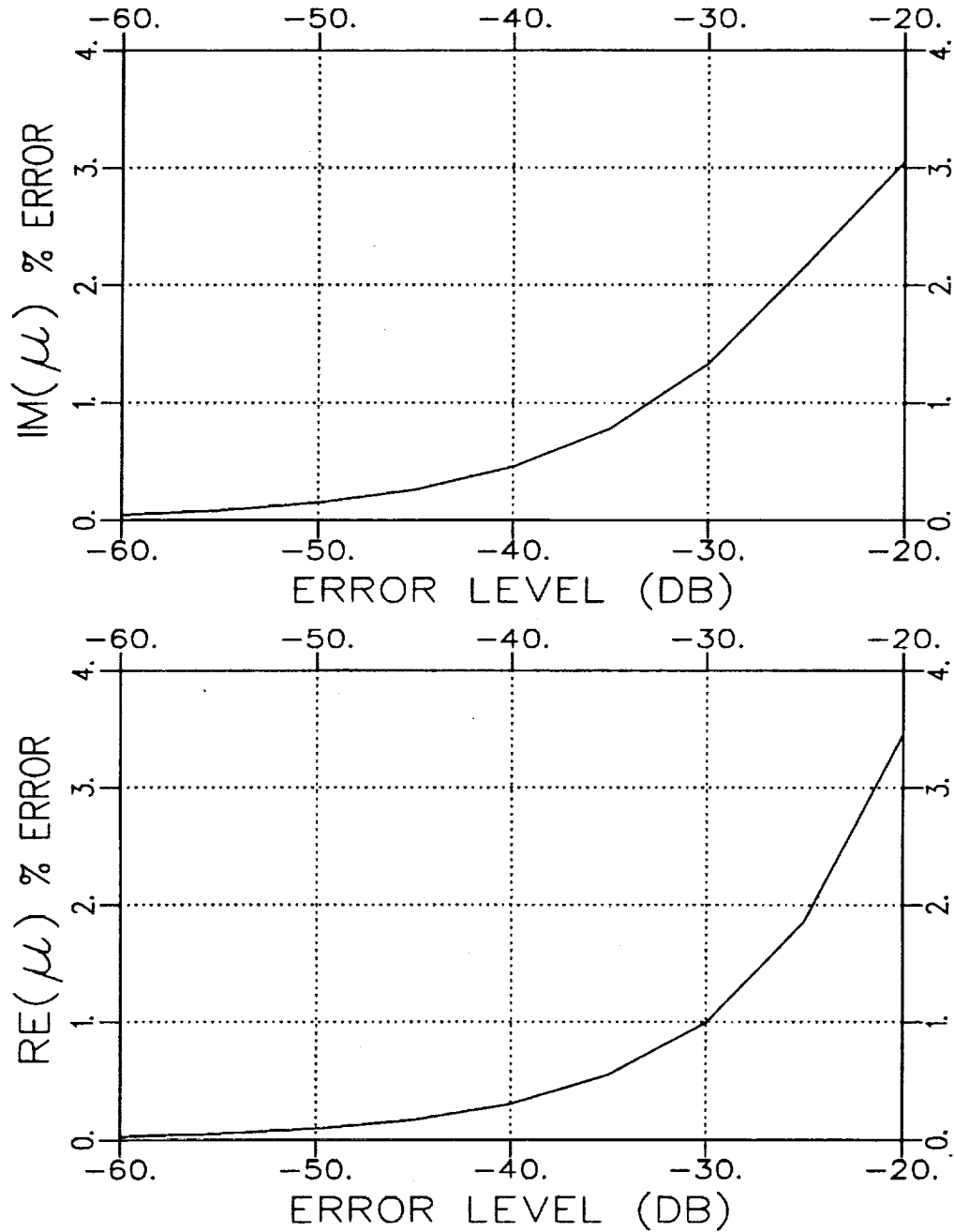


Figure 4.9: Normalized error in extracted permeability vs. error level added to S parameters. Geometry A with  $\epsilon_r = (4.0, -j.20)$ ,  $\mu_r = (1.2, -j.12)$ ,  $t = .490''$ ,  $d = .156''$  and  $f = 10 \text{ GHz}$  in an X-band fixture.

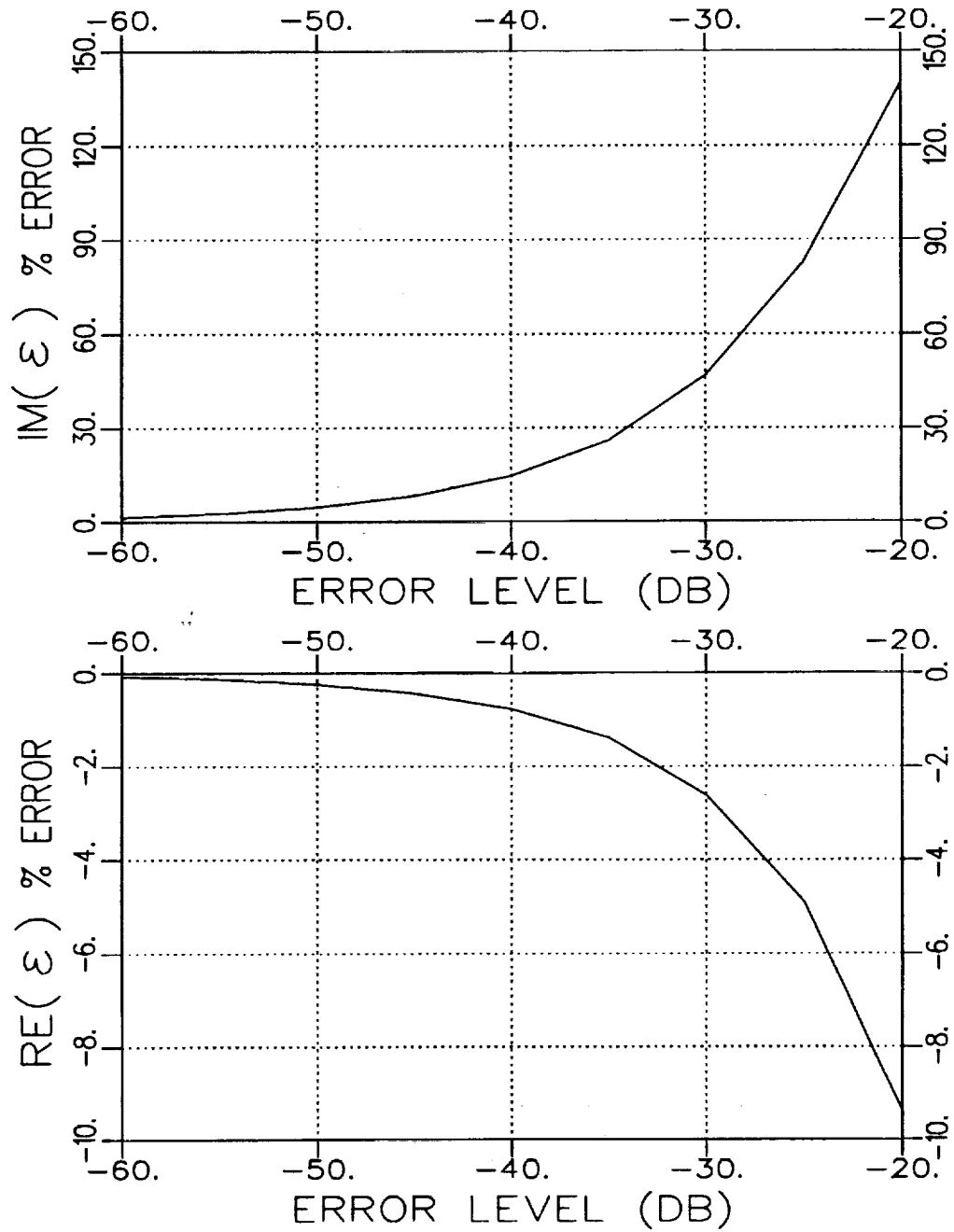


Figure 4.10: Normalized error in extracted permittivity vs. error level added to S parameters. Geometry B with  $\epsilon_r = (4.0, -j.20)$ ,  $\mu_r = (1.2, -j.12)$ ,  $t = .3''$ ,  $d = .156''$  and  $f = 10$  GHz in an X-band fixture.

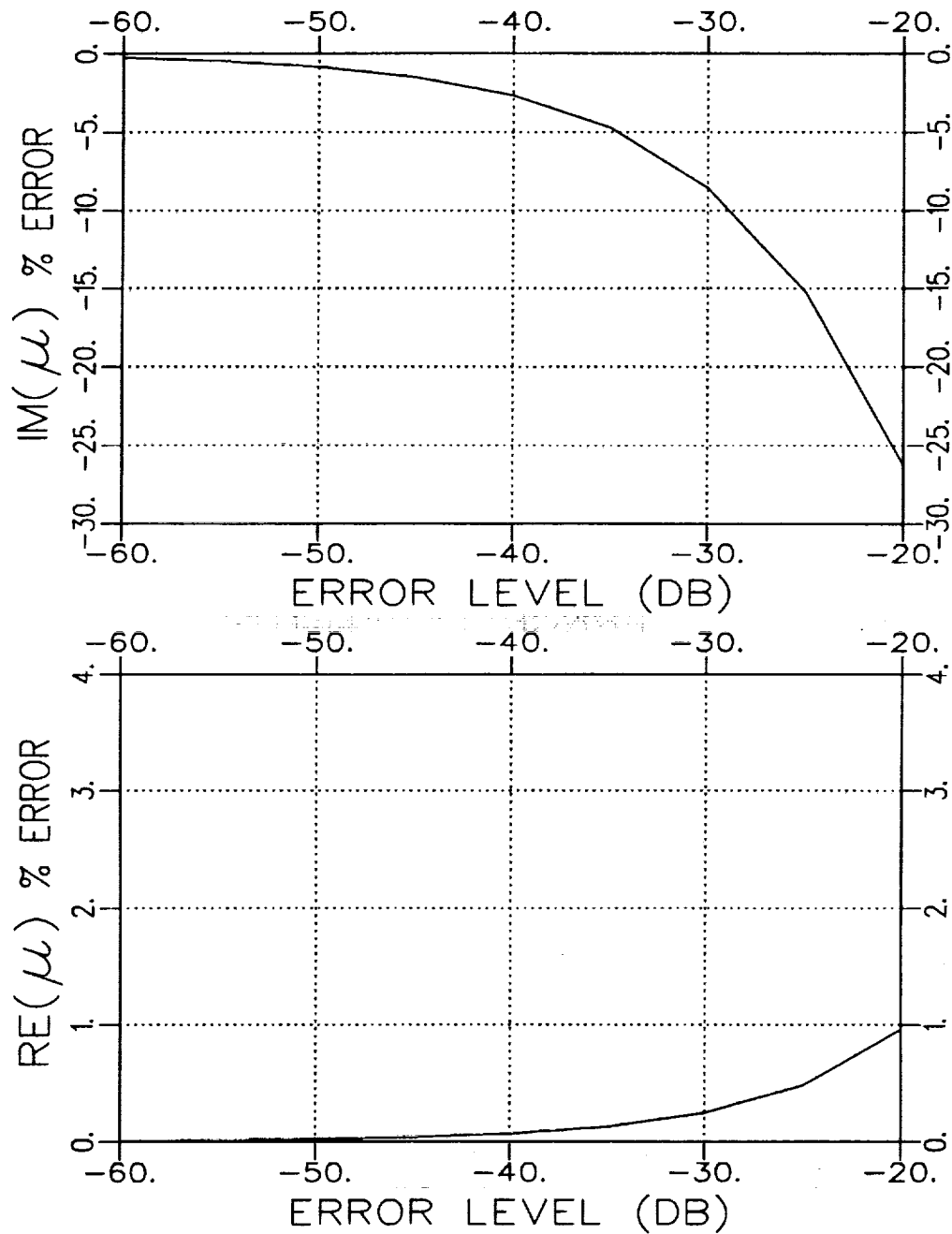


Figure 4.11: Normalized error in extracted permeability vs. error level added to S parameters. Geometry B with  $\epsilon_r = (4.0, -j.20)$ ,  $\mu_r = (1.2, -j.12)$ ,  $t = .3''$ ,  $d = .156''$  and  $f = 10$  GHz in an X-band fixture.



# I Two-Port Approach

Parameter extraction for the two-port case first requires the measurement of the reflected and transmitted field quantities (i.e.,  $S_{11}$  and  $S_{21}$ ) for a sample-filled waveguide. After a calibration has been performed on the measured data, the constitutive parameters for the sample may now be obtained via an iterative two-dimensional Newton-Raphson technique.

Figures 4.12 and 4.13 show the measured  $S_{11}$  and  $S_{21}$  data for Geometry A with sample dimensions  $t = .490''$  and  $d = .156''$ . For comparison the S parameters, calculated using the constitutive parameters of the coaxial line fixture, are also plotted. It is seen that the calculated and measured values are very similar for both S parameters except after about 11 GHz. This indicates that the parameter extraction process should produce accurate  $\epsilon$  and  $\mu$  values at frequencies below 11 GHz.

Figures 4.14 and 4.15 illustrate the measured and calculated S parameter data for Geometry B with sample dimensions  $t = .300''$  and  $d = .156''$ . Notice that around a frequency of 10.5 GHz the measured  $S_{11}$  begins to diverge considerably from the expected calculated  $S_{11}$ . Also after 11 GHz the measured  $S_{21}$  begins to differ significantly from the calculated values of  $S_{21}$ . These discrepancies may be explained by the fact that there was not sufficient contact between the sample material and the wall of the waveguide. Also error in the calibration technique may have occurred. In any case parameter extraction from these S parameter measurements for Geometry B cannot be expected to be accurate after around 10.5 GHz for this particular case.

This Newton-Raphson method uses two functionals,  $F_1$  and  $F_2$ , which consist of calculated and measured values of  $S_{11}$  and  $S_{21}$  and are defined as

$$F_1 = S_{11}^{calc}(\epsilon, \mu) - S_{11}^{meas} \quad (4.1)$$

and

$$F_2 = S_{21}^{calc}(\epsilon, \mu) - S_{21}^{meas}. \quad (4.2)$$

An initial set of values for  $\epsilon_i$  and  $\mu_i$  are used to find the calculated  $S_{11}$  and  $S_{21}$  parameters. The next set of  $\epsilon_{i+1}$  and  $\mu_{i+1}$  are found using

$$\epsilon_{i+1} = \epsilon_i + \Delta\epsilon_i, \quad (4.3)$$

$$\mu_{i+1} = \mu_i + \Delta\mu_i \quad (4.4)$$

where

$$\Delta\epsilon_i = \frac{F_2 \frac{\partial F_1}{\partial \mu} - F_1 \frac{\partial F_2}{\partial \mu}}{J}, \quad (4.5)$$

$$\Delta\mu_i = \frac{F_1 \frac{\partial F_2}{\partial \epsilon} - F_2 \frac{\partial F_1}{\partial \epsilon}}{J} \quad (4.6)$$

and

$$J = \begin{vmatrix} \frac{\partial F_1}{\partial \epsilon} & \frac{\partial F_1}{\partial \mu} \\ \frac{\partial F_2}{\partial \epsilon} & \frac{\partial F_2}{\partial \mu} \end{vmatrix}. \quad (4.7)$$

The iteration process is continued until both functionals are driven to zero. The extracted set of constitutive parameters is then the values used in the final iteration.

Figures 4.16 and 4.17 show the extracted  $\epsilon_r$  and  $\mu_r$  values, respectively, for Geometry A from the set of measured data given in Figures 4.12 and 4.13. As expected because of the reasonable measured S parameter values, the extracted values for  $\epsilon$  and  $\mu$  are fairly stable and accurate below 11 GHz, especially the real components. The imaginary components are

not as accurate as the real parts, but it was shown earlier that the accuracy of the imaginary components would be affected more significantly by noise.

Figures 4.18 and 4.19 show the extracted  $\epsilon_r$  and  $\mu_r$  values for Geometry B from the set of measured data given in Figures 4.14 and 4.15. Although the values for extracted  $\epsilon_r$  are a little low, the values for extracted  $\mu_r$  are accurate throughout the frequency spectrum. This is true despite the S parameters diverging from the calculated values after 11 GHz.

Parameter extraction seems to have worked fairly well for both geometries. The real part of the extracted values were around what they were expected to be. But there was some inaccuracy in the imaginary parts of the extracted constitutive parameters. This inaccuracy is a result of the real part of the extracted values being much larger than the imaginary part. Vectorially, a small angular change of the complex extracted value results in essentially the same value for the real part ( $|\epsilon| \cos \alpha \approx |\epsilon|$  for small  $\alpha$ ) while the imaginary part can experience dramatic changes ( $|\epsilon| \sin \alpha \approx |\epsilon| \alpha$ ).

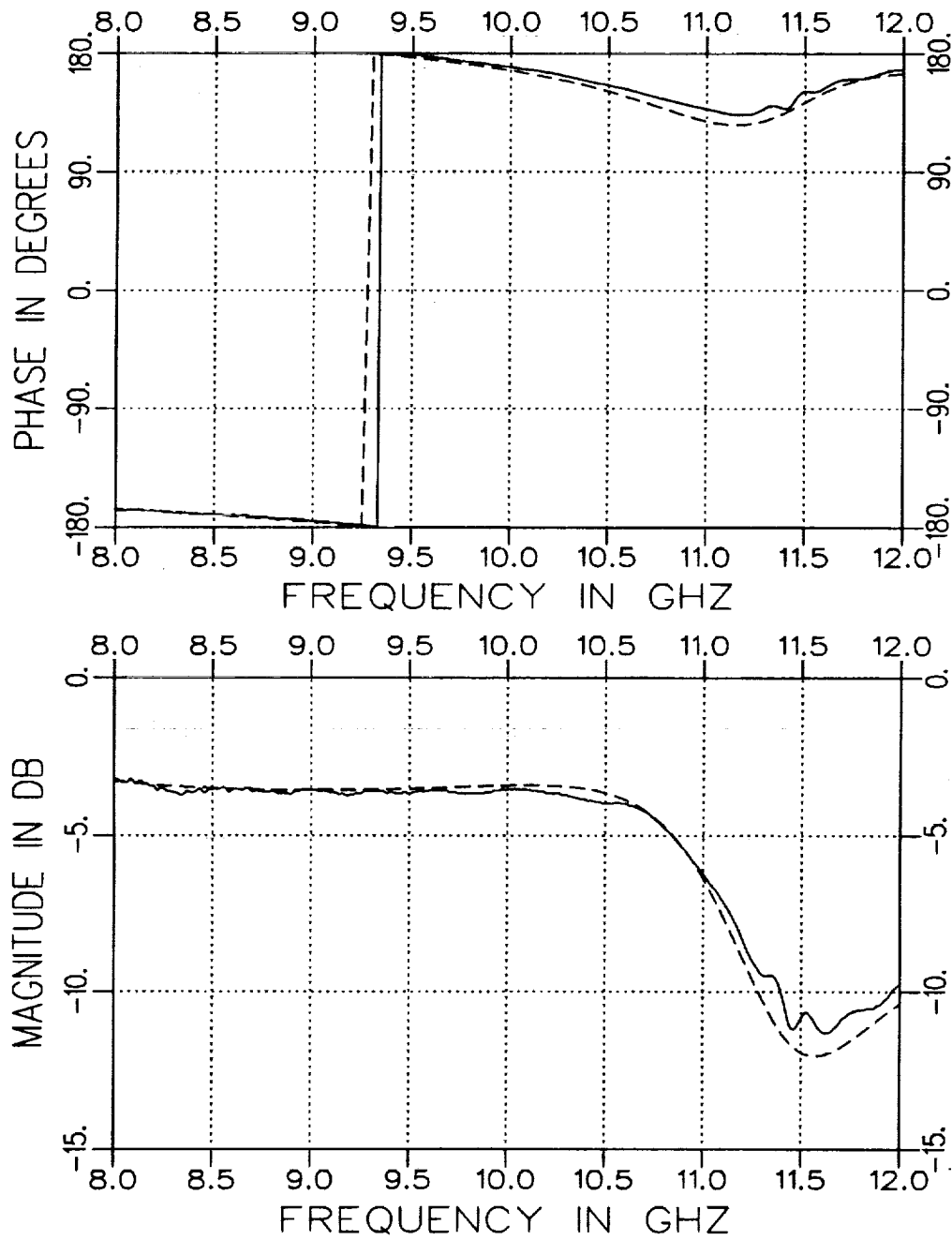


Figure 4.12: Measured (solid) and calculated (dashed)  $S_{11}$  for  $t = .490''$  and  $d = .156''$  in an X-band fixture (.4''x.9''). Calculations use  $\epsilon_r = (4.0, -j.20)$  and  $\mu_r = (1.2, -j.12)$ . Geometry A.

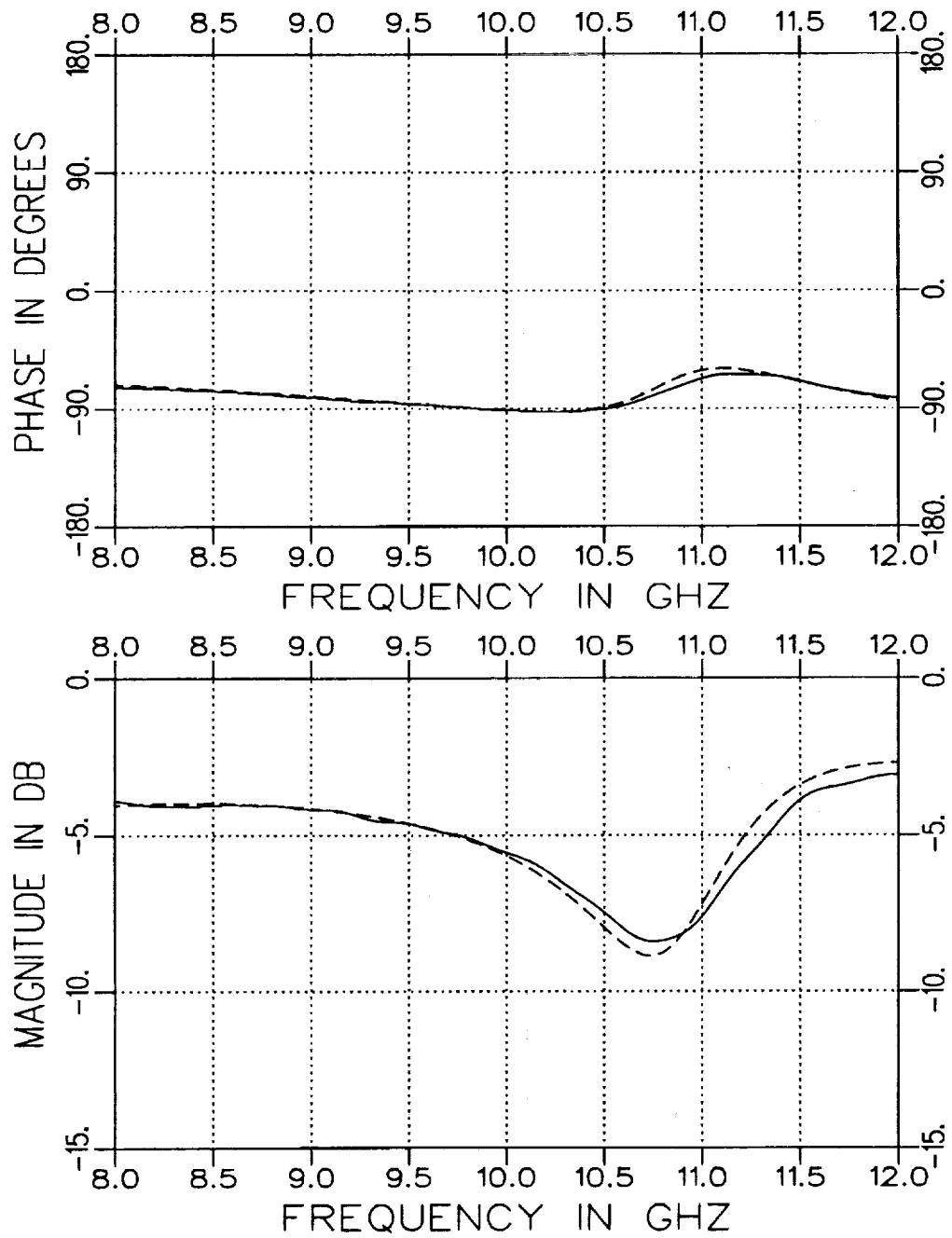


Figure 4.13: Measured (solid) and calculated (dashed)  $S_{21}$  for  $t = .490''$  and  $d = .156''$  in an X-band fixture (.4''x.9''). Calculations use  $\epsilon_r = (4.0, -j.20)$  and  $\mu_r = (1.2, -j.12)$ . Geometry A.

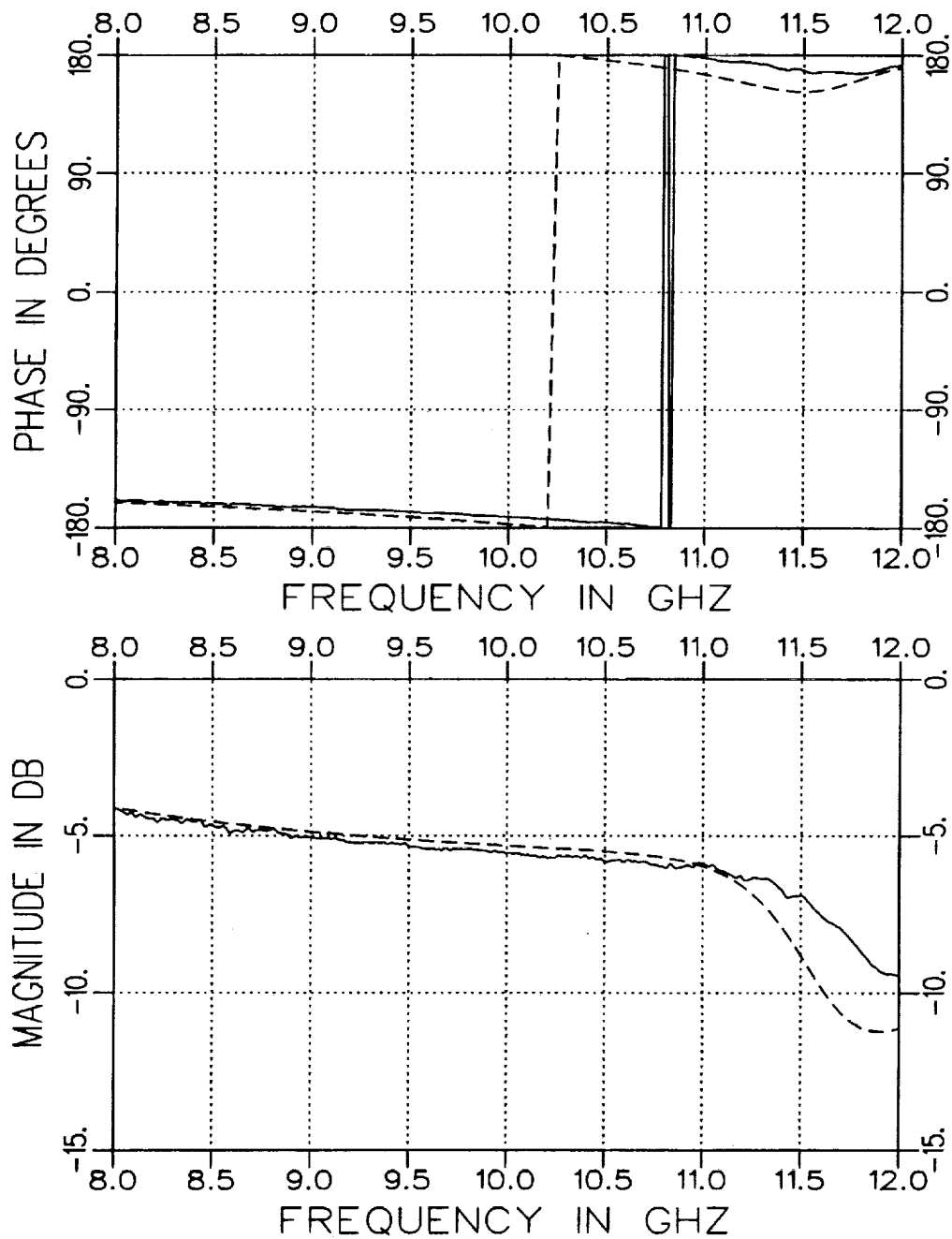


Figure 4.14: Measured (solid) and calculated (dashed)  $S_{11}$  for  $t = .300''$  and  $d = .156''$  in an X-band fixture (.4''x.9''). Calculations use  $\epsilon_r = (4.0, -j.20)$  and  $\mu_r = (1.2, -j.12)$ . Geometry B.

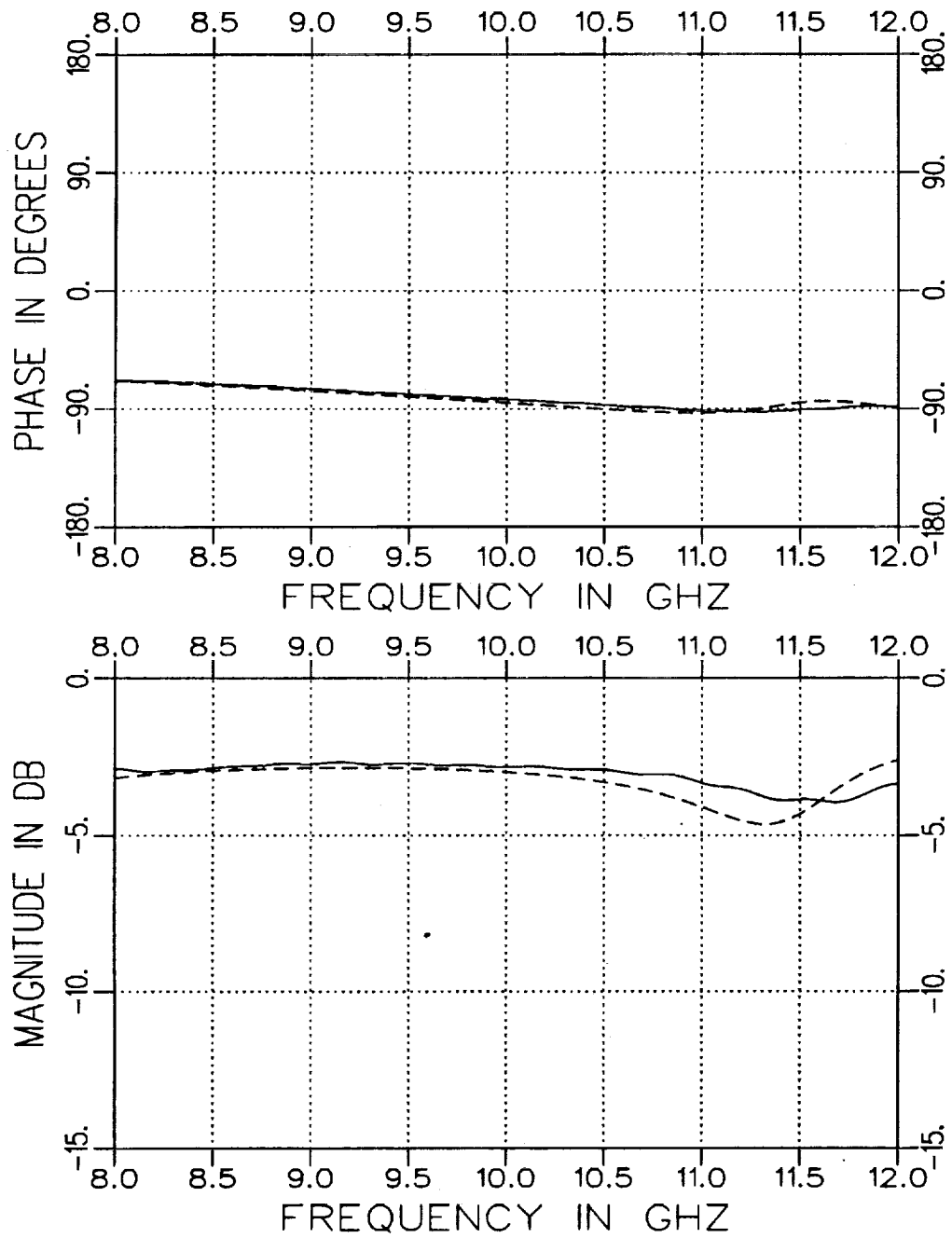


Figure 4.15: Measured (solid) and calculated (dashed)  $S_{21}$  for  $t = .300''$  and  $d = .156''$  in an X-band fixture (.4"x.9"). Calculations use  $\epsilon_r = (4.0, -j.20)$  and  $\mu_r = (1.2, -j.12)$ . Geometry B.

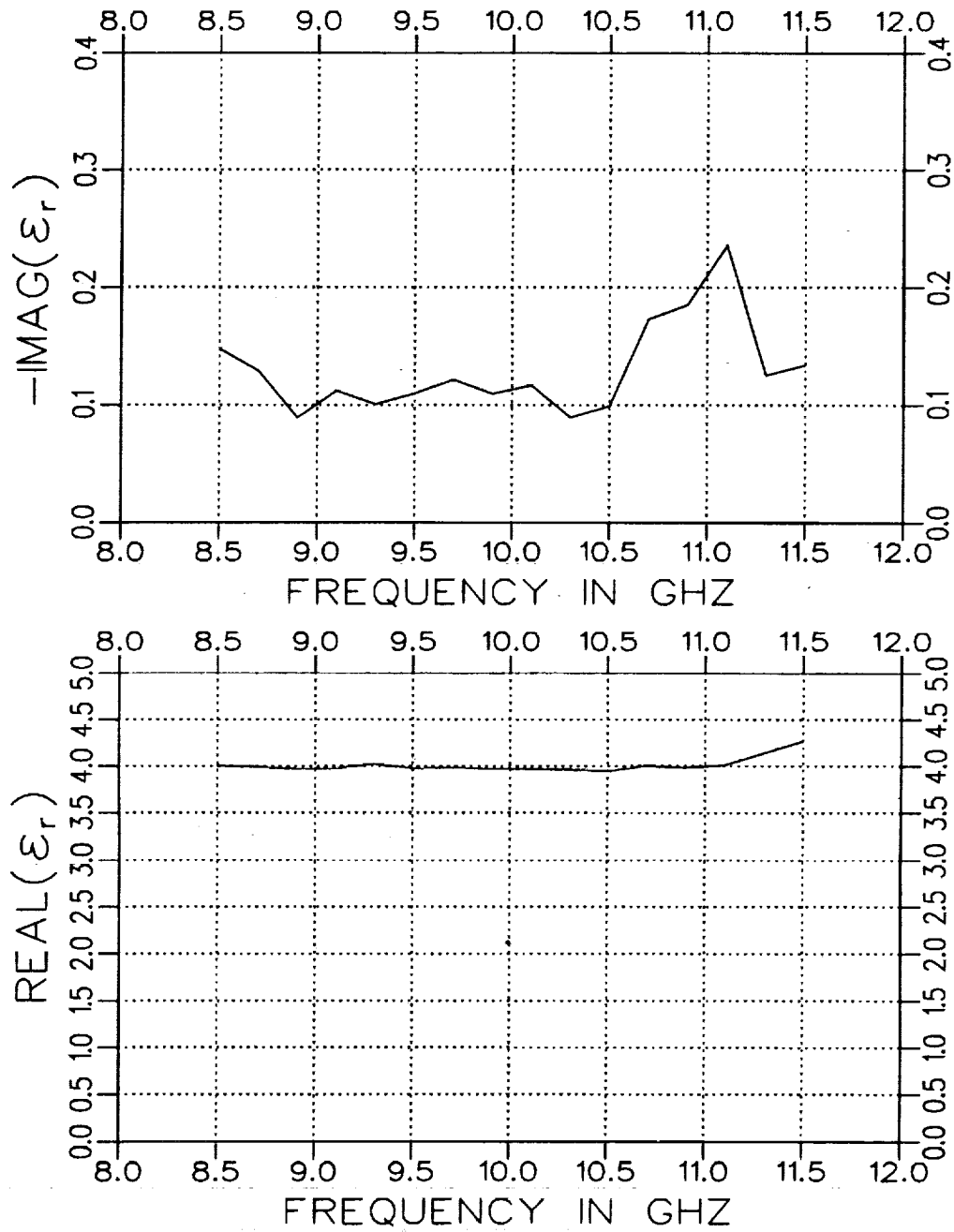


Figure 4.16: Extracted  $\epsilon_r$  for Geometry A with  $t = .490''$  and  $d = .156''$  in an X-band fixture (.4''x.9'').



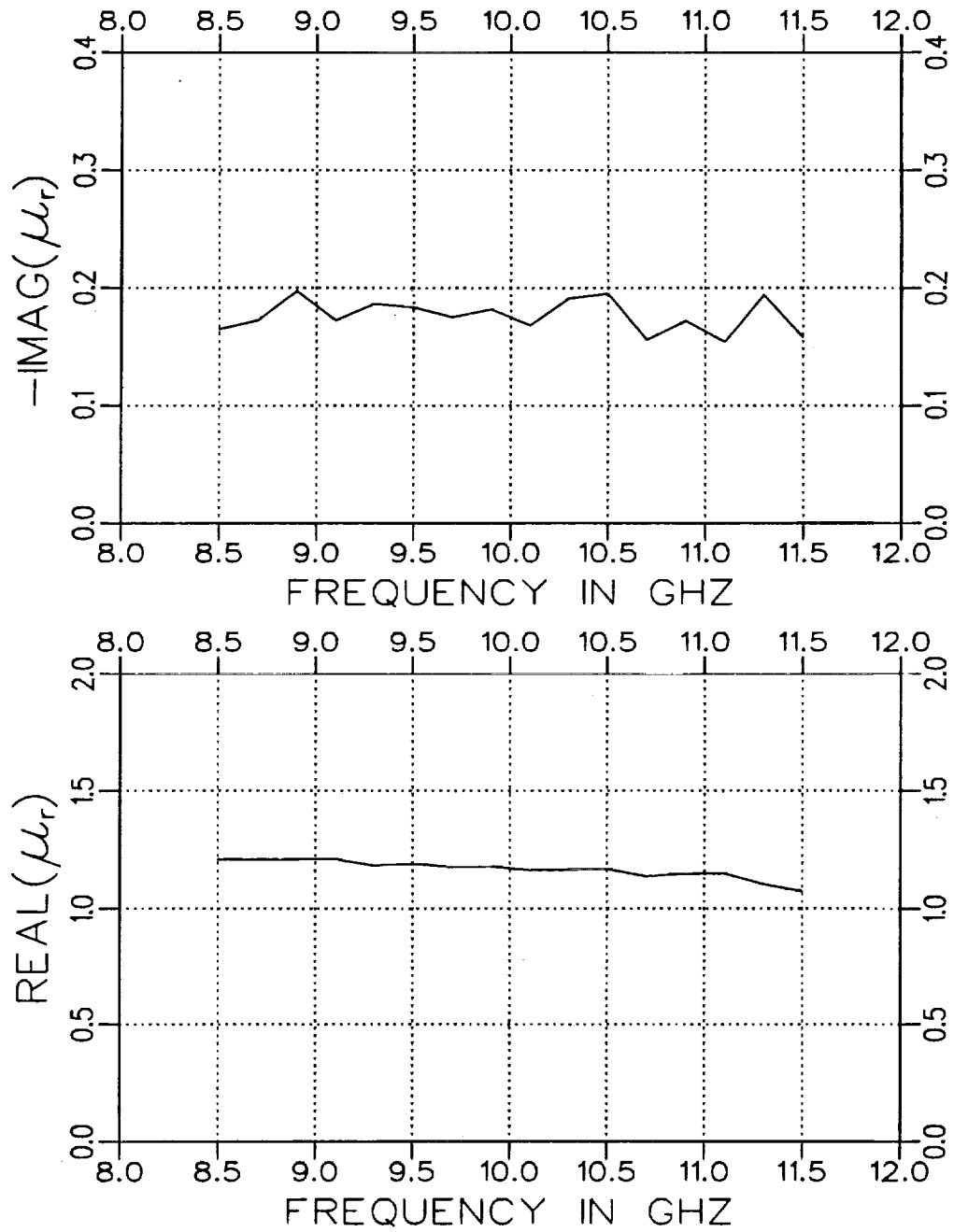


Figure 4.17: Extracted  $\mu_r$  for Geometry A with  $t = .490''$  and  $d = .156''$  in an X-band fixture (.4''x.9'').

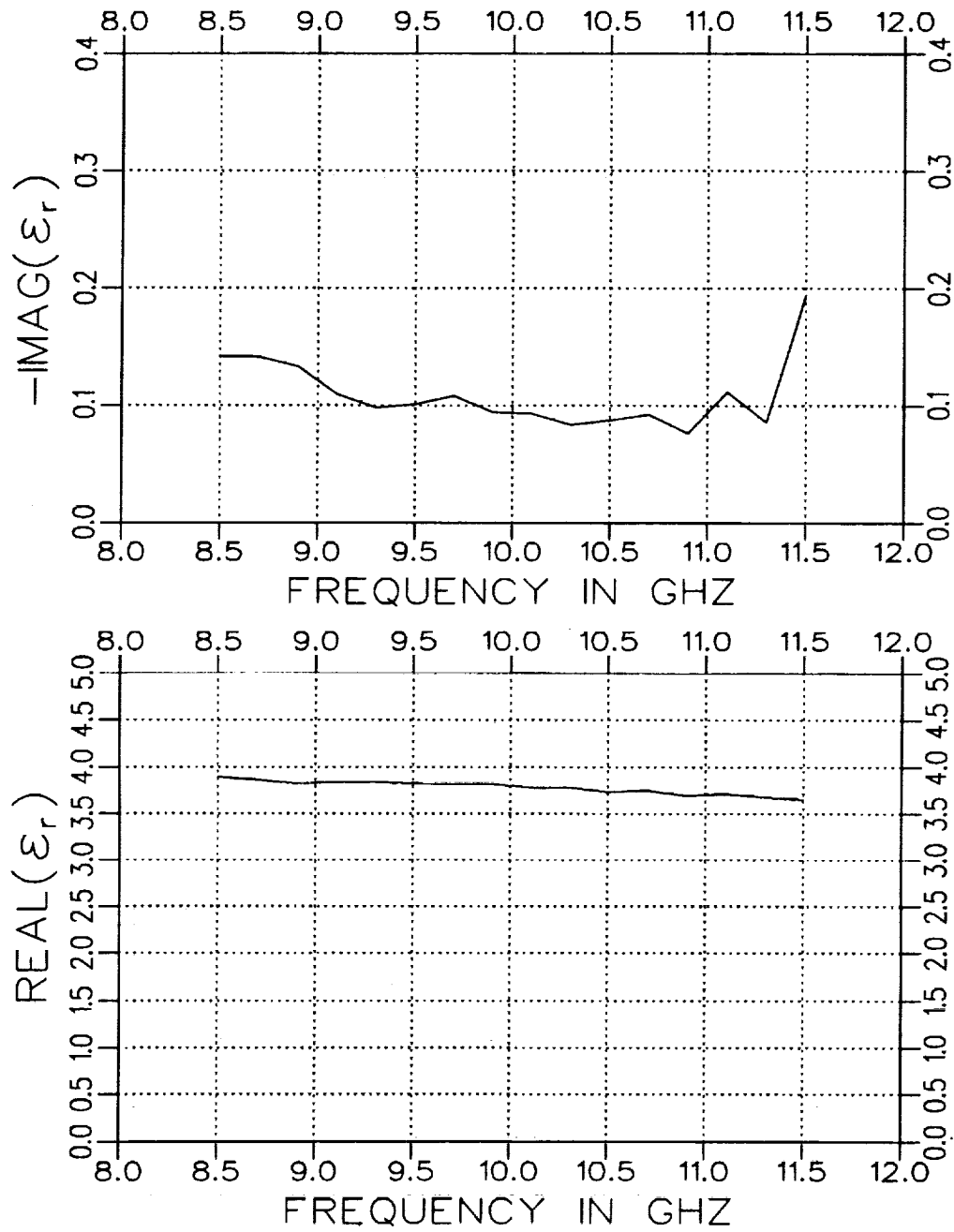


Figure 4.18: Extracted  $\epsilon_r$  for Geometry B with  $t = .300''$  and  $d = .156''$  in an X-band fixture (.4"x.9").

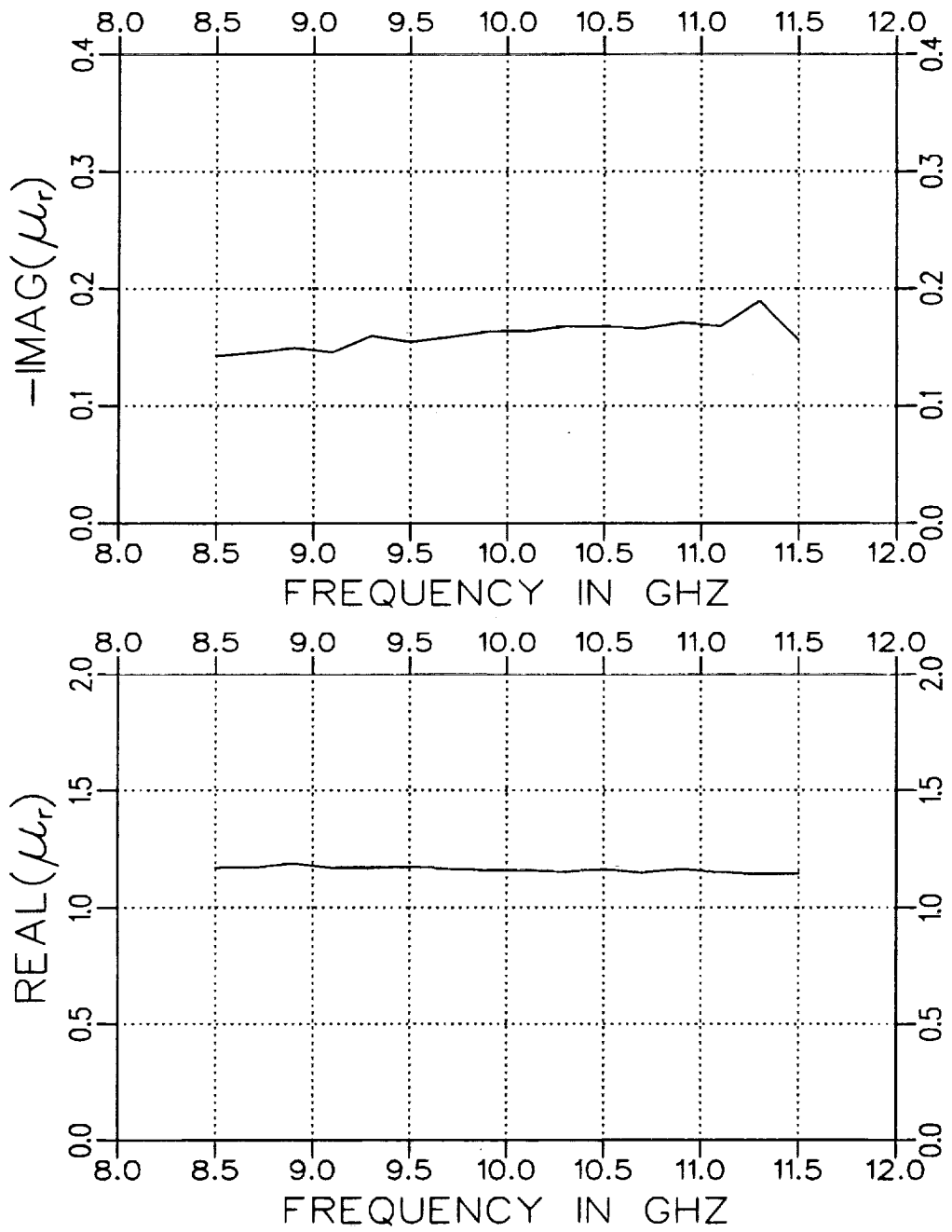


Figure 4.19: Extracted  $\mu_r$  for Geometry B with  $t = .300''$  and  $d = .156''$  in an X-band fixture (.4"x.9").

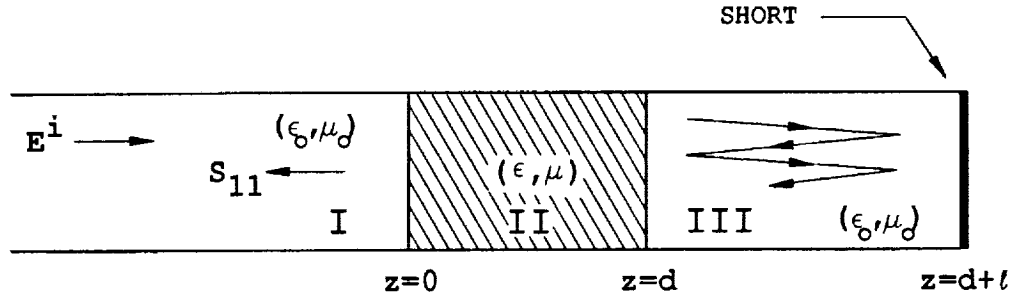


Figure 4.20: Single-port fixture geometry.

## II Single-Port Approach

The necessary S parameters for material parameter extraction can be acquired from a two-port fixture. However, a single-port fixture may be used to simplify the measurement process and requirements of fixture design at elevated temperatures. For this simplification, additional signal processing is required to recover the  $S_{11}$  and  $S_{21}$  parameters. Figure 4.20 illustrates the single-port fixture geometry. The reflected field for this geometry can be expressed as

$$E^r = S_{11} - \frac{S_{21}^2 e^{-j2\beta_0 \ell}}{1 + S_{11} e^{-j2\beta_0 \ell}} \quad (4.8)$$

when only the dominant mode can propagate in the air-filled portion of the guide and  $\beta_0$  is the propagation constant for that mode. It is important to account for loss in the propagation constant,  $\beta_0$ , if the fixture itself has sufficient loss. The self-consistent expression for this fixture geometry is given in Appendix A which accounts for all modes in the air-filled portion of the fixture. The other higher order modes are not of great importance when the sample/short separation distance,  $\ell$ , is large.

Equation (4.8) contains the S parameter information required to determine the material parameters. This expression is simply the geometric

summation of all the multiple reflected and transmitted signals due to the short in the fixture. Figure 4.21 illustrates the terms of this summation in a time domain plot for a completely-filled waveguide cross section and  $d = .156''$ . The first signal ( $t=0$ ) in this figure is simply  $S_{11}$  while the second is  $-S_{21}^2$ . These desired quantities can be recovered from the total reflected field through signal processing techniques. One technique is time domain gating [11] which may be undesirable due to the small single mode bandwidth available in waveguide fixtures. An alternative is to use a moving average technique upon the frequency domain data. This technique is conceptually comparable to the time domain gating approach because it duplicates a discrete convolution. This particular moving average performs a weighted average around the  $i^{\text{th}}$  point using the neighboring  $n$  points. The greater  $n$  becomes, the tighter the effective time gating window becomes.

The  $S_{11}$  parameter can be recovered from the measured data by simply applying a moving average to the data when the phase reference is placed at  $t=0$  and using the proper number of neighboring points. The  $S_{21}$  parameter is recovered in a similar manner but with the data initially phase adjusted to place the second signal at  $t=0$ . This is accomplished by multiplying the measured data by the phase factor of  $e^{j2\beta_0 \ell}$ .

The performance of this technique is demonstrated in Figures 4.22 through 4.27 where the distance from the front of the sample to the short ( $d + \ell$ ) was  $10.012''$  and an X-band fixture was used. Figures 4.22 and 4.23 contain the recovered S parameters for a completely-filled cross-sectional waveguide sample region. Figures 4.24 through 4.27 contain the recovered S parameters for the partially-filled case for Geometries A and B. Because of the type of processing that was used, the recovery of the S parameters at the frequency band edges was not good. Note that for the moving

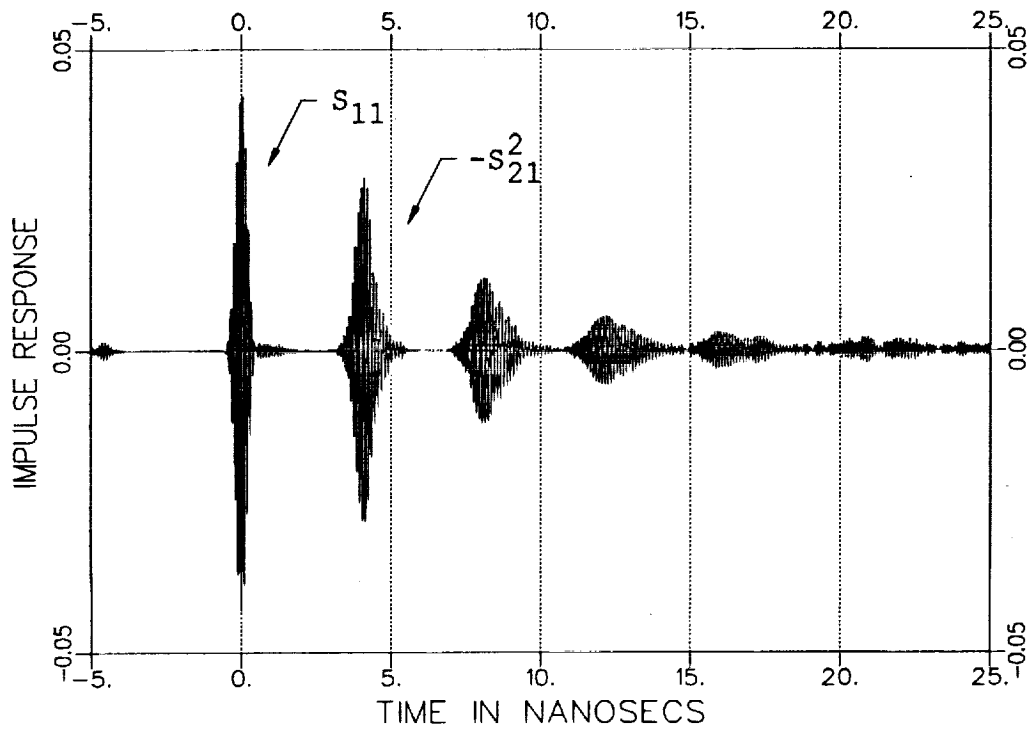


Figure 4.21: Time domain plot for a one-port measurement. Completely filled X band fixture with  $d = .156''$ .

average approach to succeed in recovering the desired S parameters, the sample/short separation distance,  $\ell$ , has to be sufficiently large. A length of at least six inches is required. Also note that the sample length should be less than  $\lambda_g/2$  to avoid nulls in the S parameters which is a similar requirement when the cross-section is completely filled. This requirement is based not only on the need to maintain a good signal to noise ratio but also to avoid nulls since the moving average technique will "fill" them in.

Now that the  $S_{11}$  and  $S_{21}$  data has been determined, the extraction procedure of the two-port method is used to find the constitutive parameters. Figures 4.28 through 4.33 show the extracted  $\epsilon$  and  $\mu$  values for the completely-filled case and the two geometries of Figures 4.22 through 4.27. Note that the measured and calculated values of the S parameters are in fairly good agreement. This indicates that accurate constitutive parameter extraction should occur. As expected, Figures 4.28 through 4.33 suggest that accurate parameter extraction has indeed been achieved at least for the real components. The imaginary components suffered a bit of inaccuracy due mostly to the small amount of error introduced during the process of recovering the S parameters from the one-port data. For the completely-filled case and both geometry configurations, it was found that because of this error the imaginary component of  $\epsilon$  tended to be low while the imaginary part of  $\mu$  tended to be high.

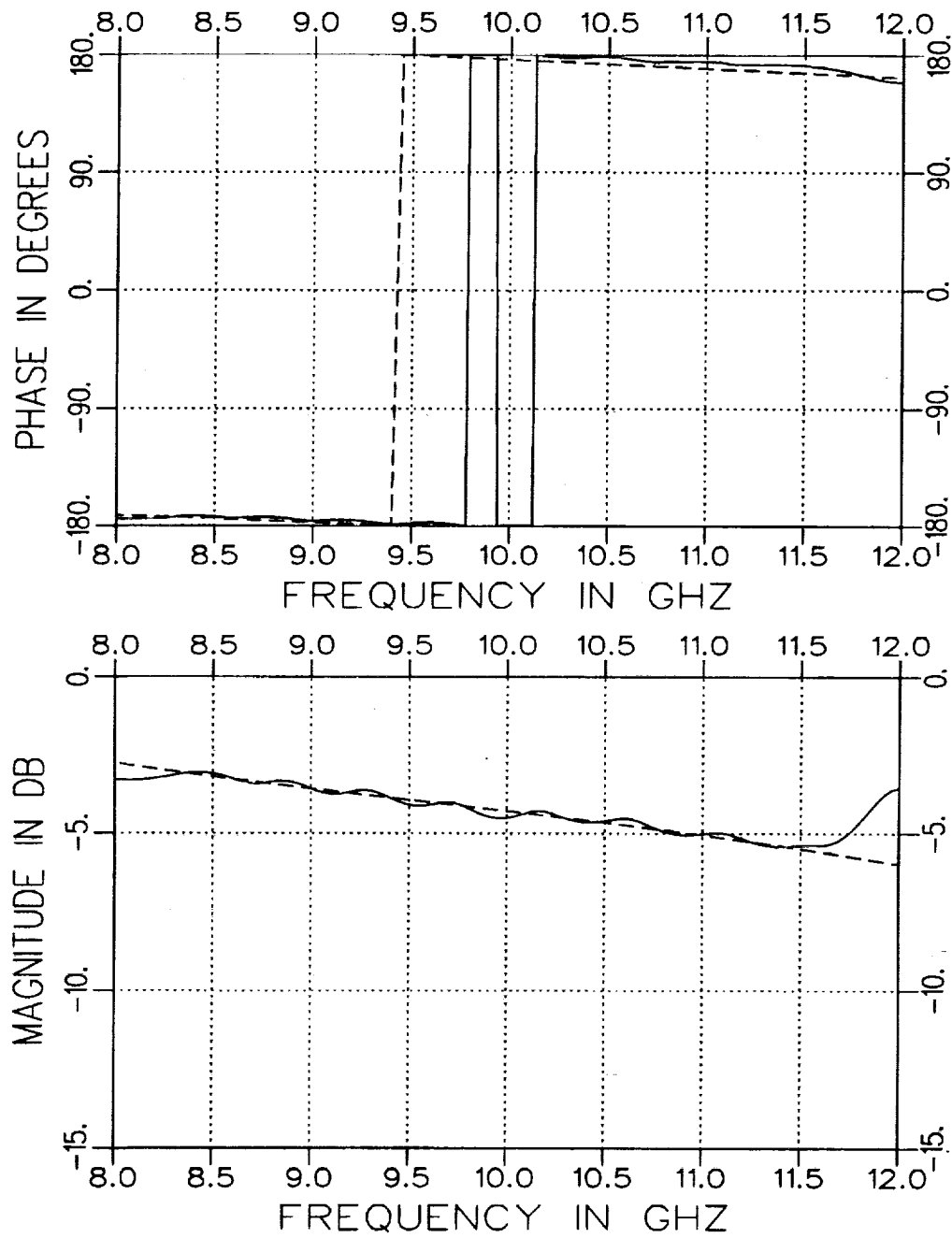


Figure 4.22: Recovered  $S_{11}$  from a measured one-port file (solid) compared with  $S_{11}$  from a two-port measurement (dashed). Completely-filled cross-section with  $d = .156''$  in an X-band fixture.



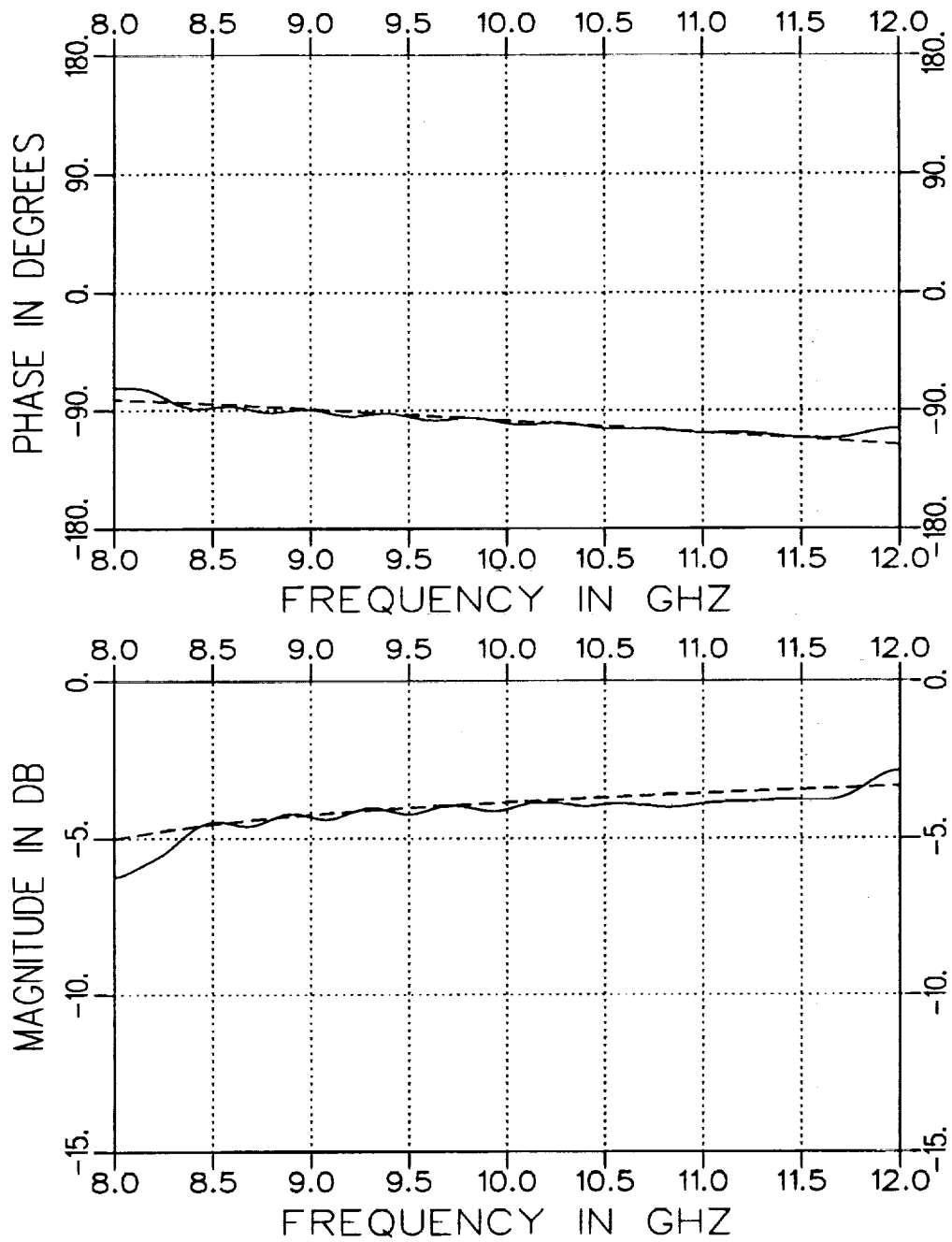


Figure 4.23: Recovered  $S_{21}$  from a measured one-port file (solid) compared with  $S_{21}$  from a two-port measurement (dashed). Completely-filled cross-section with  $d = .156''$  in an X-band fixture.

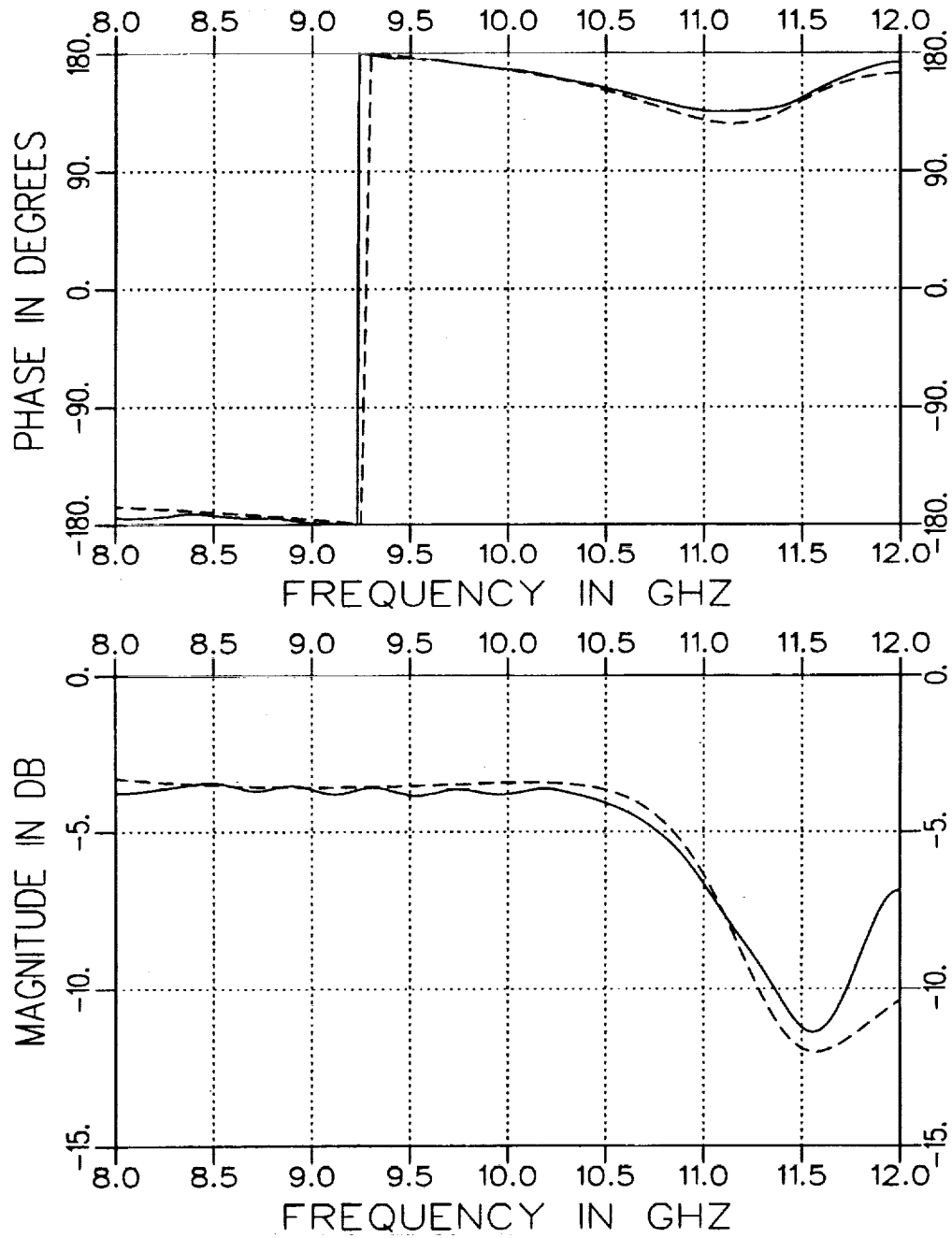


Figure 4.24: Recovered  $S_{11}$  from a measured one-port file (solid) compared with  $S_{11}$  from a two-port measurement (dashed). Geometry A with  $t = .490''$  and  $d = .156''$  in an X-band fixture.

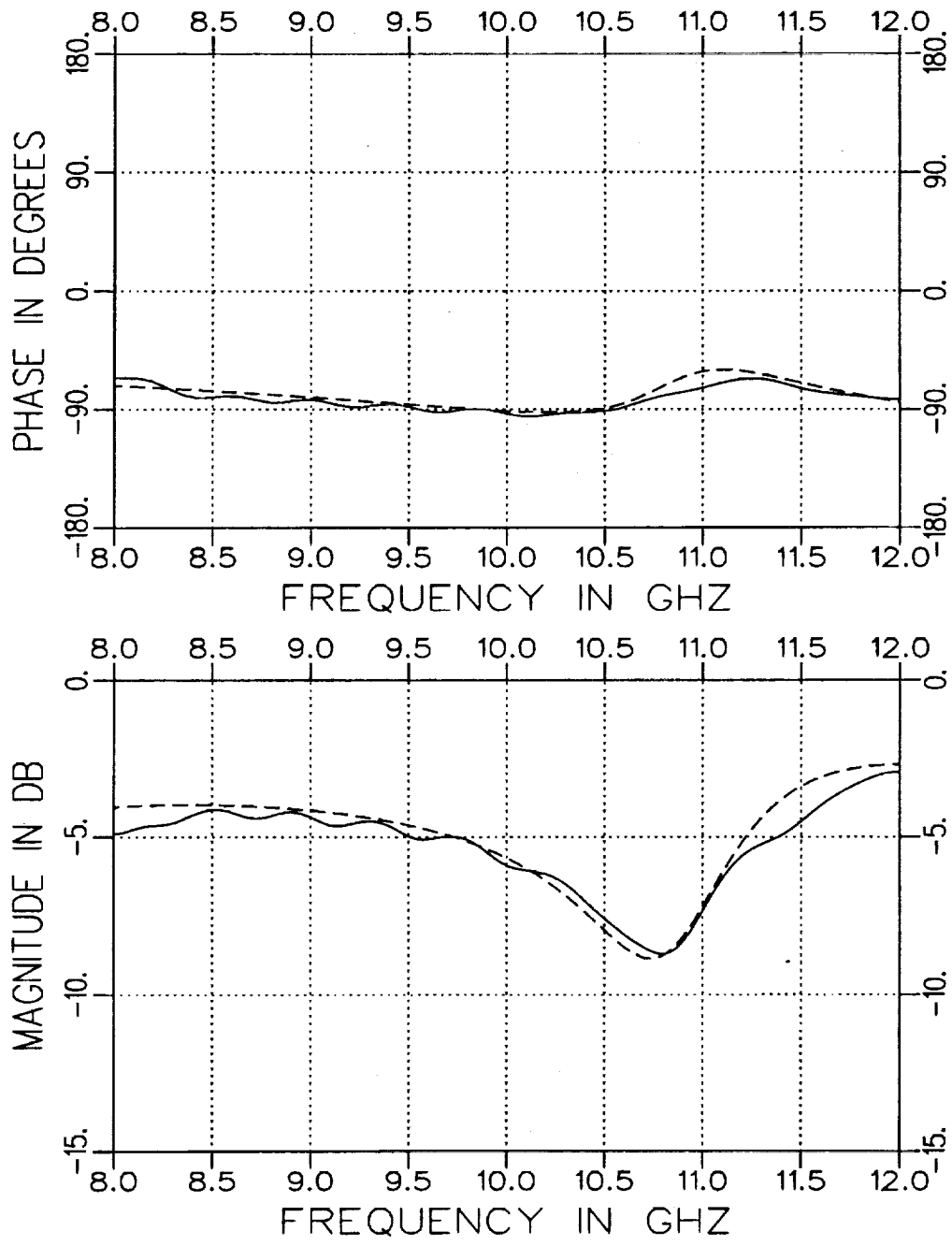


Figure 4.25: Recovered  $S_{21}$  from a measured one-port file (solid) compared with  $S_{21}$  from a two-port measurement (dashed). Geometry A with  $t = .490''$  and  $d = .156''$  in an X-band fixture.

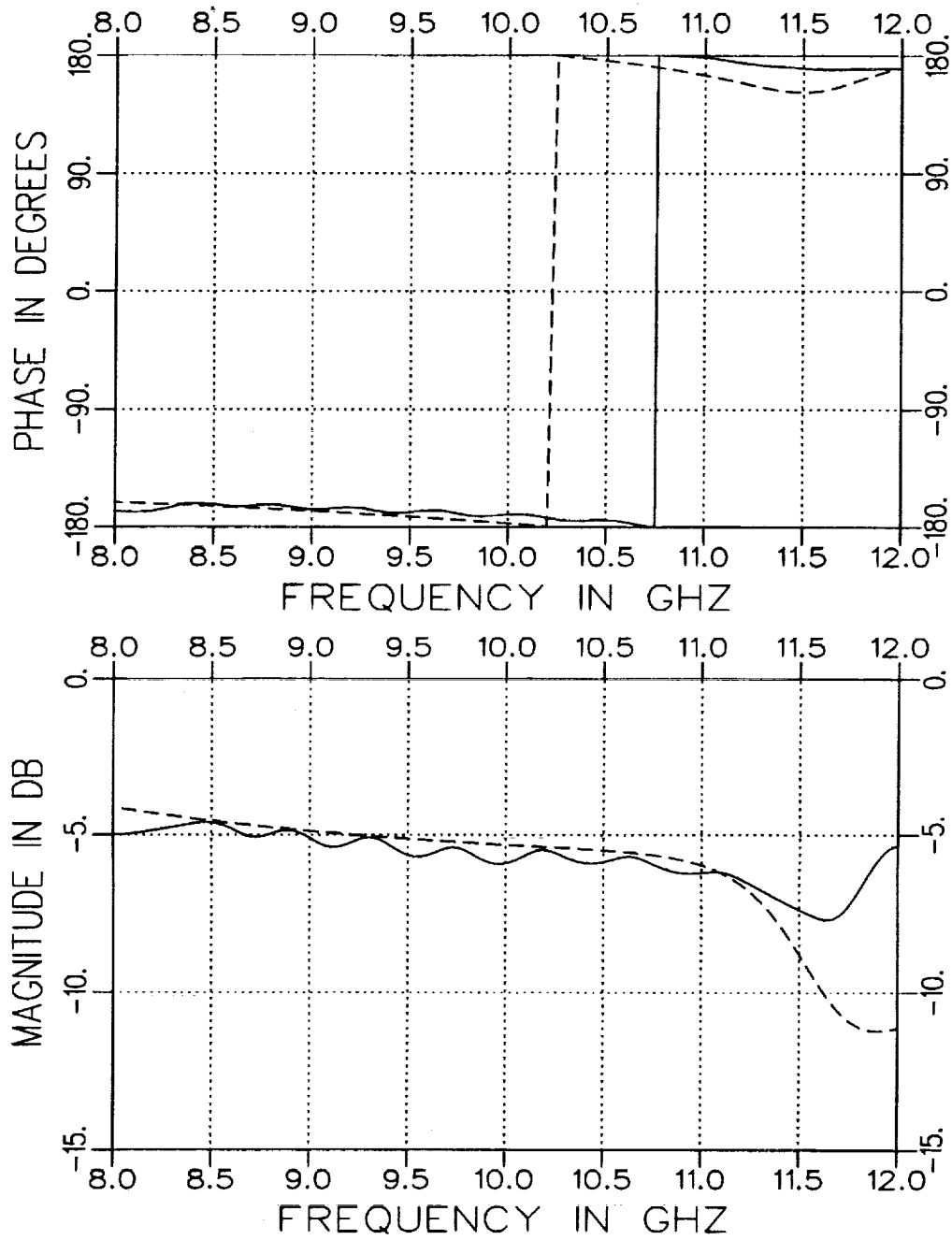


Figure 4.26: Recovered  $S_{11}$  from a measured one-port file (solid) compared with  $S_{11}$  from a two-port measurement (dashed). Geometry B with  $t = .300''$  and  $d = .156''$  in an X-band fixture.

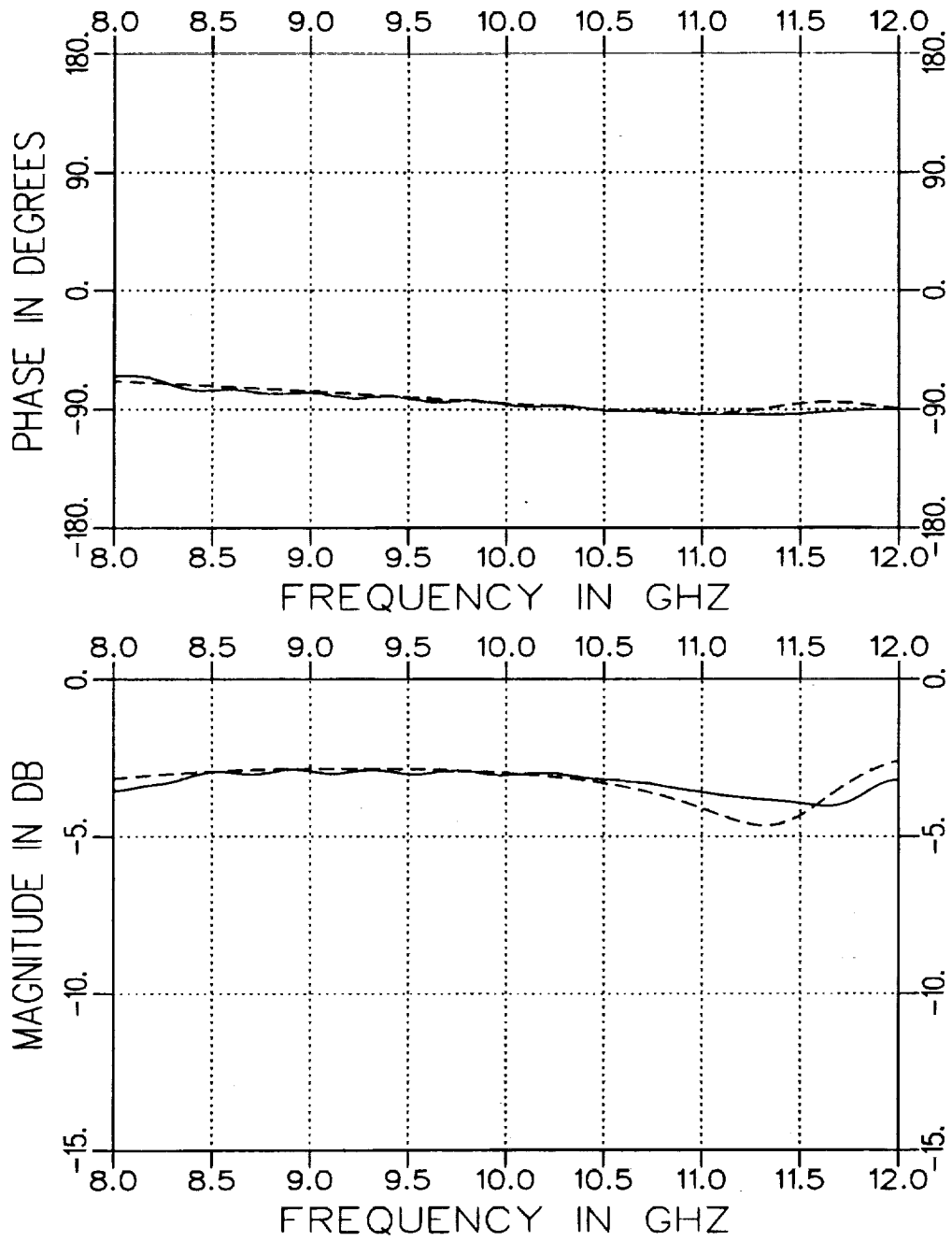


Figure 4.27: Recovered  $S_{21}$  from a measured one-port file (solid) compared with  $S_{21}$  from a two-port measurement (dashed). Geometry B with  $t = .300''$  and  $d = .156''$  in an X-band fixture.

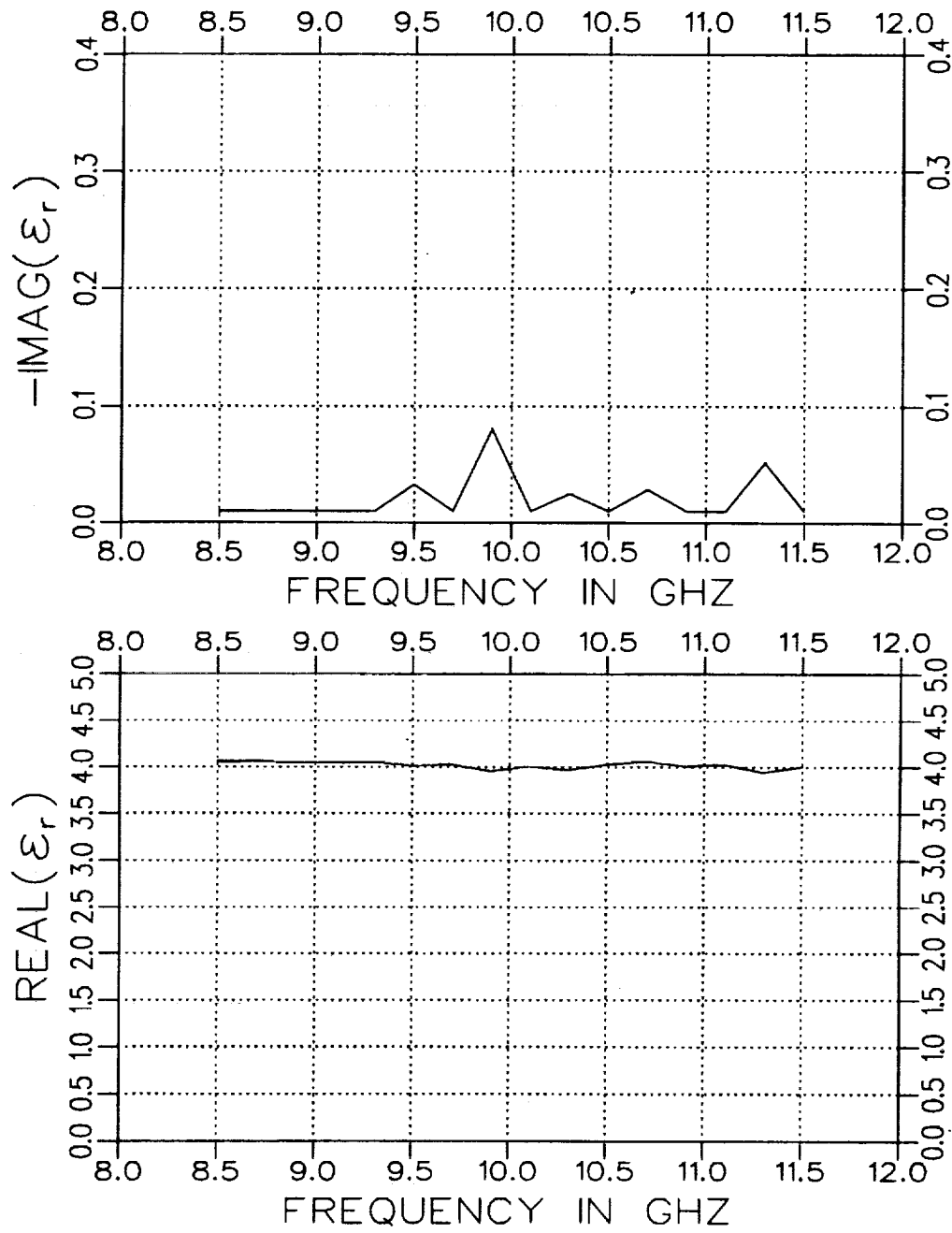


Figure 4.28: Extracted  $\epsilon_r$  from a one-port file for a completely-filled waveguide with  $d = .156''$  in an X-band fixture.

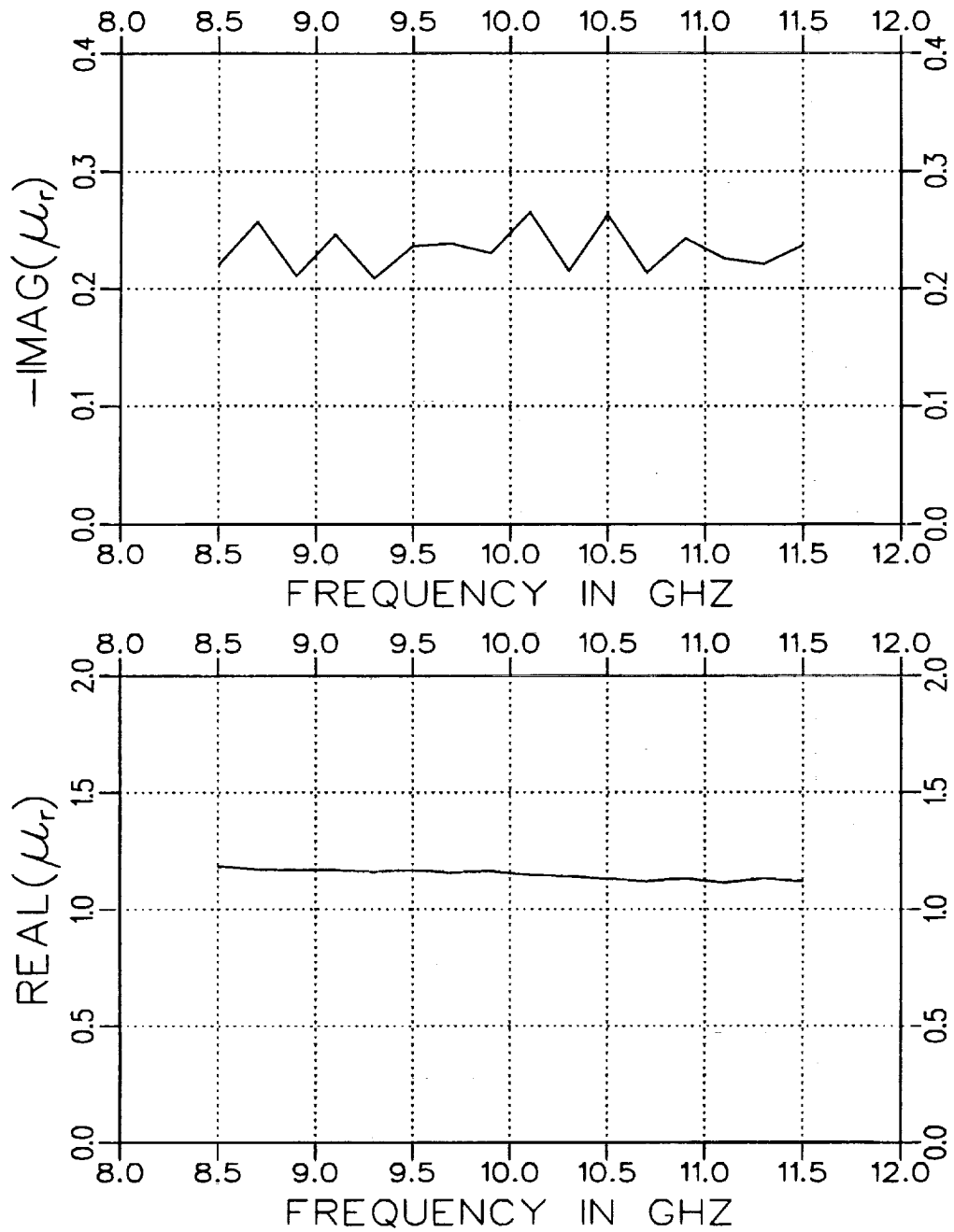


Figure 4.29: Extracted  $\mu_r$  from a one-port file for a completely-filled waveguide with  $d = .156''$  in an X-band fixture.

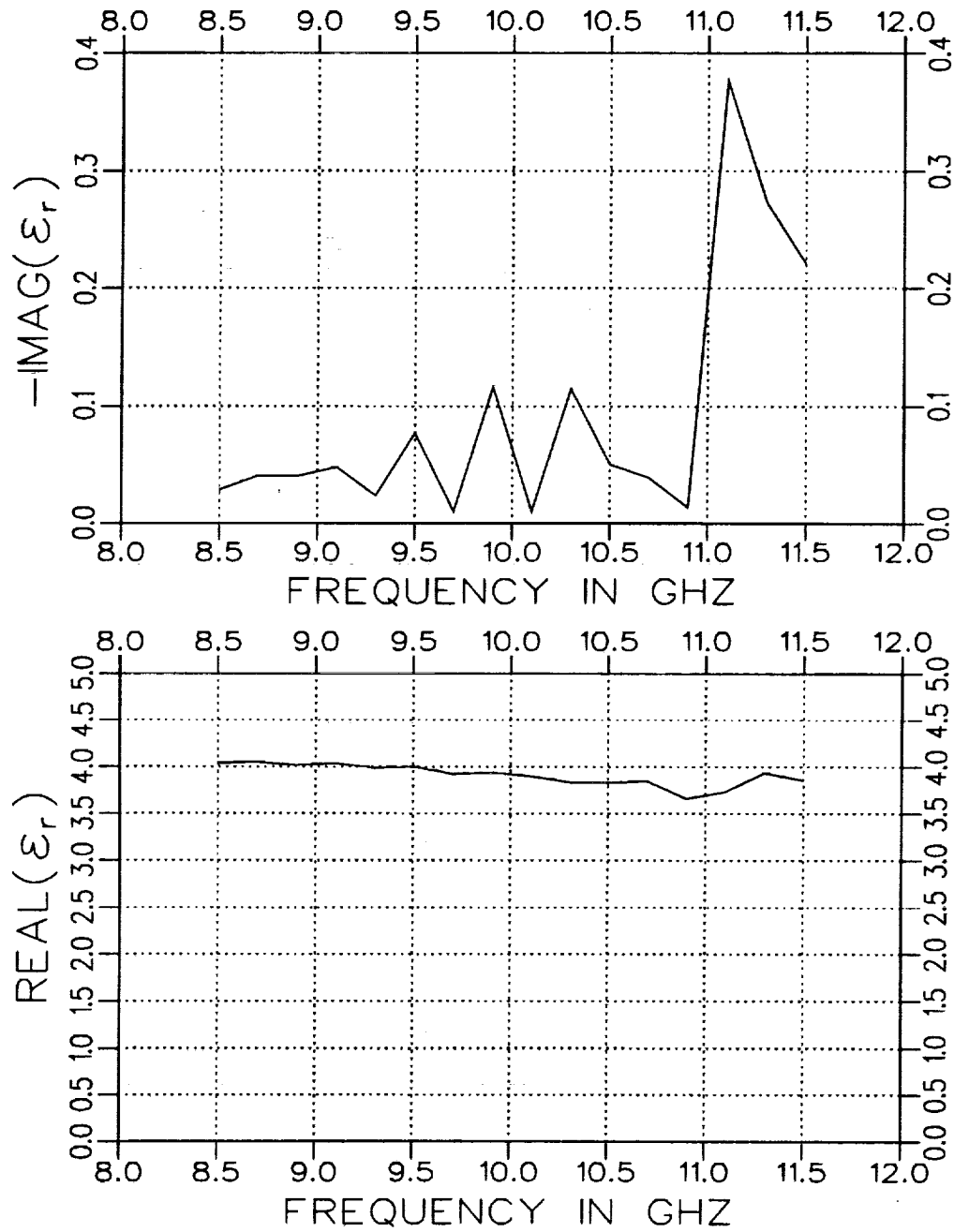


Figure 4.30: Extracted  $\epsilon_r$  from a one-port file. Geometry A with  $t = .490''$  and  $d = .156''$  in an X-band fixture.



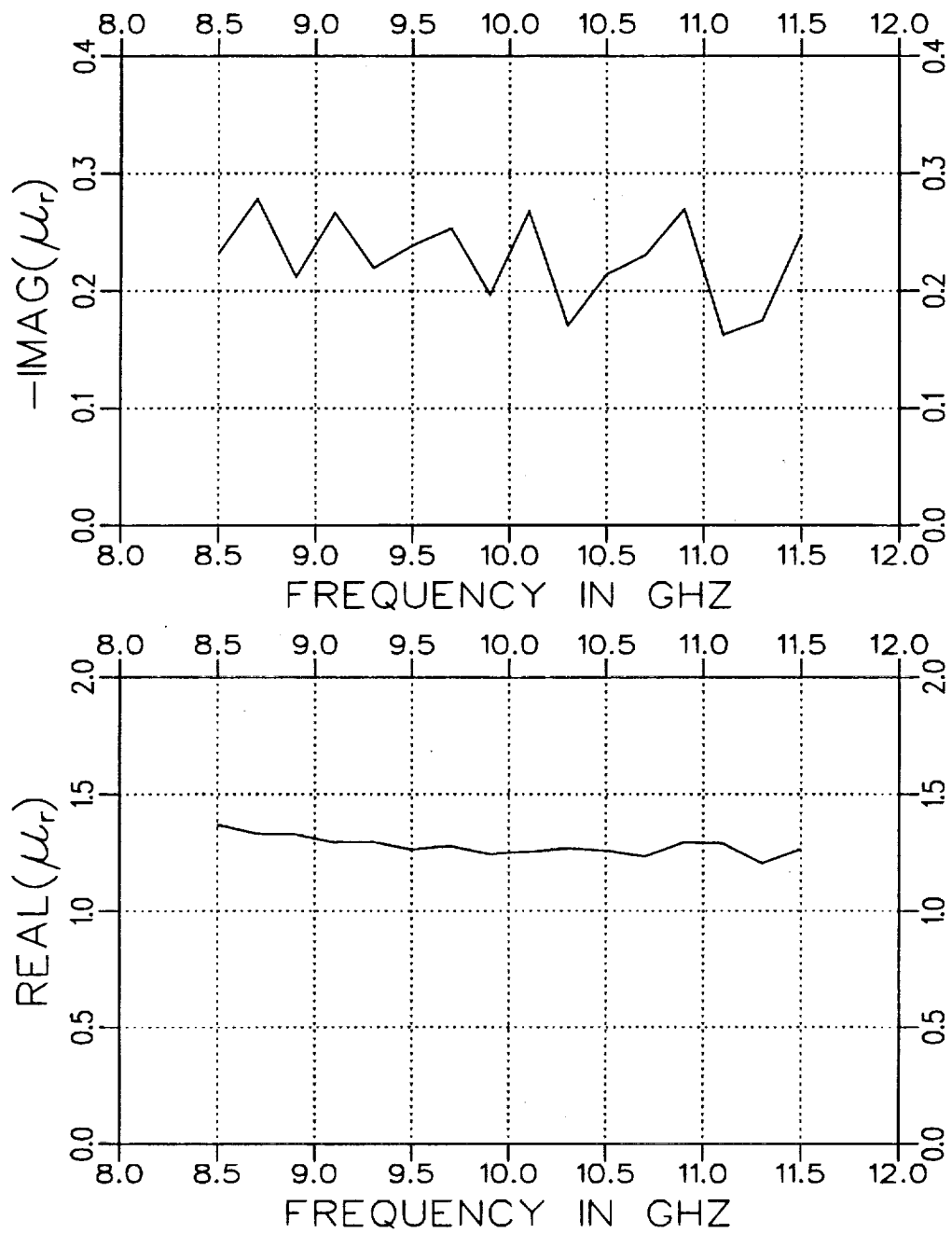


Figure 4.31: Extracted  $\mu_r$  from a one-port file. Geometry A with  $t = .490''$  and  $d = .156''$  in an X-band fixture.

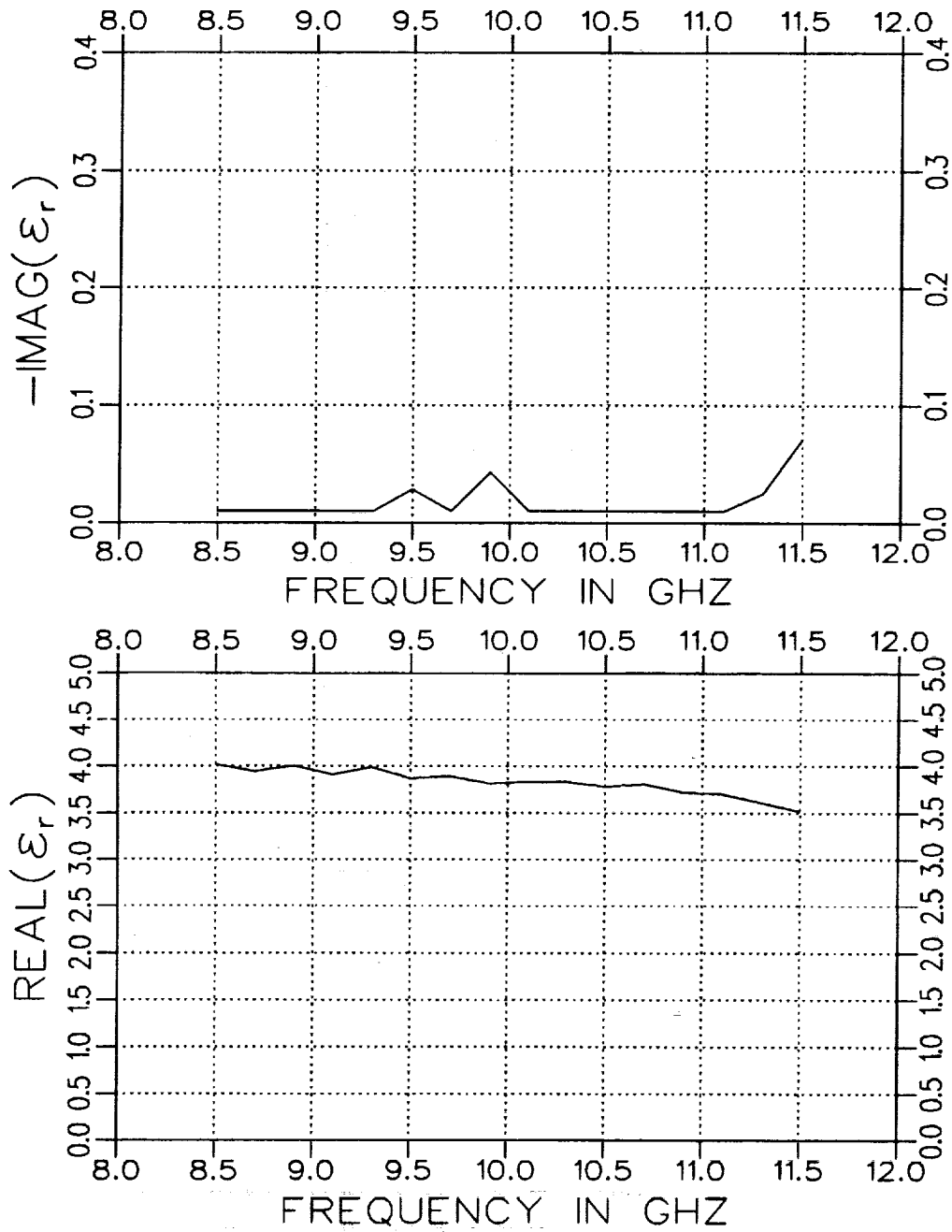


Figure 4.32: Extracted  $\epsilon_r$  from a one-port file. Geometry B with  $t = .300''$  and  $d = .156''$  in an X-band fixture.

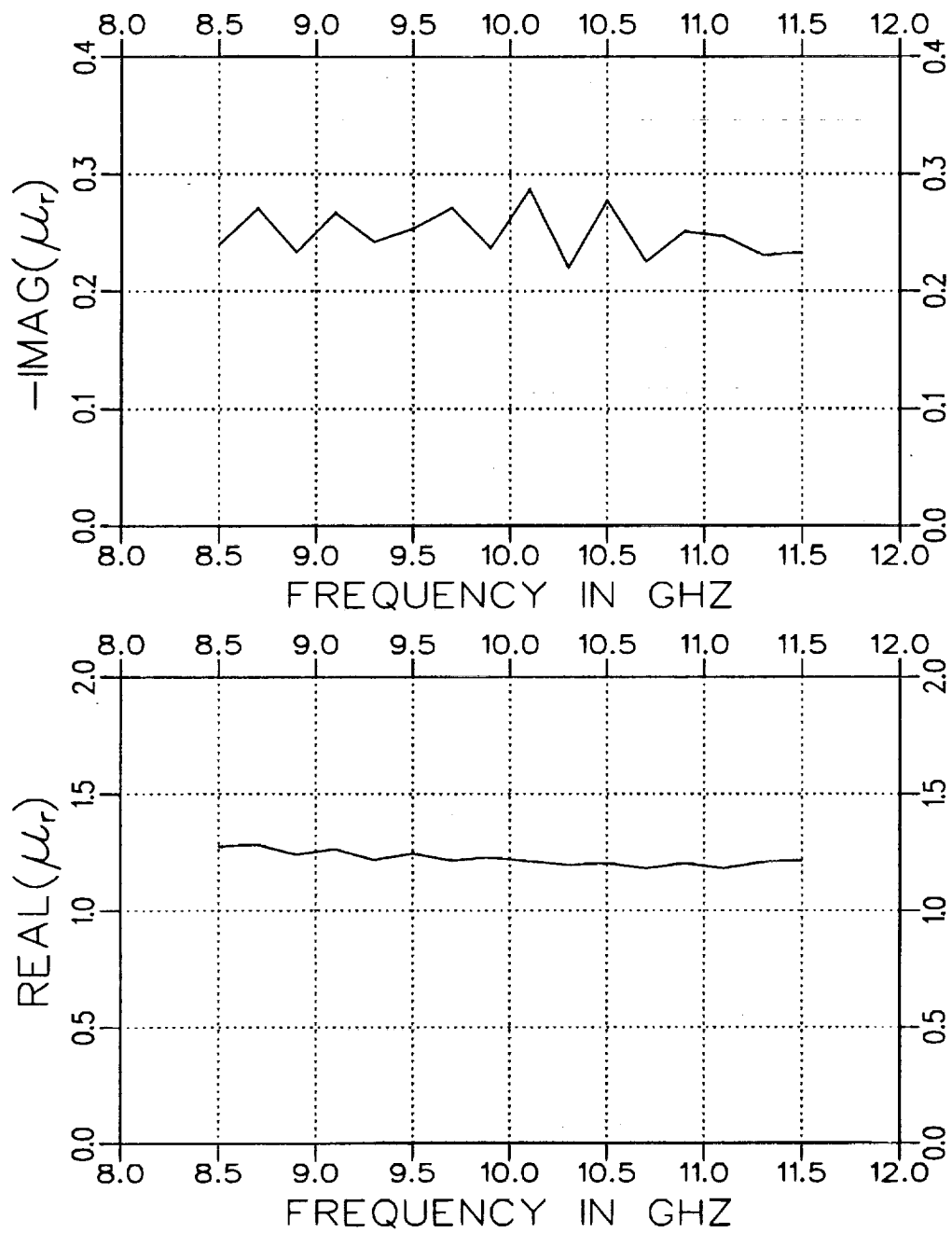


Figure 4.33: Extracted  $\mu_r$  from a one-port file. Geometry B with  $t = .300''$  and  $d = .156''$  in an X-band fixture.

# Chapter 5

## Conclusions

Waveguide structures can be used to ascertain the constitutive parameters  $\epsilon$  and  $\mu$  of a material. Traditionally for a rectangular waveguide fixture its cross section is completely filled with the material to be measured. But with a high temperature environment, air gaps can appear which cause error in the S parameter measurements. This lessens the accuracy of the constitutive parameters that are extracted from these S parameter measurements. This report examined the effect of air gaps on the accuracy of the extracted parameters and provides alternate approaches to account for these air gaps in the extraction process. An added benefit of introducing an air gap between the fixture's side walls and sample allows a greater choice in sample dimensions to provide for a desired level of measured signals. Also included is a description for a single-port approach to obtain the necessary quantities ( $S_{11}$  and  $S_{21}$ ) obtained from the more traditional two-port approach. A single-port approach has mechanical benefits for high temperature heating considerations.

Errors in the measurement originate from several sources. This report focused upon the effect of air gaps but also considered sample positioning and dimensions error as well. Errors from calibration or fixture connections were not considered.

The effect of air gaps along both side walls of the fixture was examined. A small air gap oriented along the short wall of a rectangular waveguide (Geometry A) was shown to have little effect on the S parameters which means that parameter extraction should remain accurate. In contrast, a small air gap oriented along the longer wall of a rectangular waveguide (Geometry B) alters the S parameters significantly so that the recovery of an accurate set of constitutive parameters would become difficult. But if the size of the air gap in Geometry B is made larger and known beforehand the S parameters may not change very much with small changes in the size of the air gap. Thus the preferred orientation of the sample in the rectangular waveguide is Geometry B because small gaps along the short wall that may appear with high temperature variation does not seem to impair accurate parameter extraction as drastically as small gaps along the long wall.

Other examined errors which occur in any rectangular waveguide measurements are those due to phase offset error in  $S_{11}$  and sample length error. The phase offset error which is caused by the sample not being placed where the calibration reference was placed effected a large amount of error in the imaginary part of the extracted constitutive parameters. Thus the positioning of the material sample must be fairly accurate. On the other hand the accuracy of the extracted parameters is not nearly as sensitive to the error between the actual and assumed lengths of the material.

The two-port and single-port approaches to S parameter measurement were discussed. The two-port approach requires simply acquiring  $S_{11}$  and  $S_{21}$  and initiating the extraction process. The one-port approach would be more suitable to high temperature variation since only one end of the waveguide would be necessary to acquire  $S_{11}$ . The one-port method involves recover-

ing the equivalent  $S_{11}$  and  $S_{21}$  parameters of a two-port system from the one-port  $S_{11}$  measurements. Because the one-port approach requires an additional signal processing step, it does not yield as accurate  $\epsilon$  and  $\mu$  values as in the two-port approach.

The accuracy of the presented single-port technique relies heavily upon knowing the separation distance between the material sample and the short very accurately. This may have limitations for elevated temperature measurements. An alternative to this technique but still using a single-port fixture is to measure the return from two material samples of different lengths which have their far side positioned against a short. This technique is similar to the presented technique but with no separation distance between the material sample and the short. With this alternate technique, two different sample lengths have to be measured to acquire two independent responses. The presented technique acquires two independent responses through signal processing. Such processing is not possible when the separation distance is zero.

Finally, significant error is introduced in the imaginary component of the extracted  $\epsilon$  and  $\mu$  values when the loss is small. This result occurs in any transmission line measurement. Vectorially examining the extracted values indicates the explanation. A small change in the magnitude or angle of this vector will result in only a small change in its real component while a significant change will occur in its imaginary when the loss is small. However, the uncertainty in the loss value is minimized when a sufficient sample length is used.

# Appendix A

## The Self-Consistent Technique

The self-consistent procedure is used to simplify the analysis of the two- and single-port waveguide problems. Potentially, one method used to find the reflected and transmitted fields in a two-port problem is to expand the fields in the three different regions of the waveguide and then enforce the boundary conditions at the two material interfaces. The desired solution then requires a matrix inversion. The size of the required matrix to be inverted can be reduced to one half the size if only one interface boundary (semi-infinite problem) needs to be enforced. The self-consistent technique provides this smaller dimensioned matrix to be inverted. This benefit results in a faster solution when the order of the matrix becomes large. The desired two-interface problem can be solved with the one interface results. Formally the size of these matrices is infinitely large, but in practice there are  $N \times N$  matrices where  $N$  is the number of terms kept in the modal expansions.

Once the scattering matrices are known, they can be used in the formulas for the reflected and transmitted fields. These formulas will be derived next using the self-consistent procedure for the two-port and single-port formulations.

# I Two-Port Formulation

Referring to Figure A.1, let  $[A^+]$  denote the vector containing the amplitudes of the modes of Region II traveling in the  $+\hat{n}$  ( $-z$ ) direction and  $[A^-]$  the amplitudes of the modes traveling in the  $-\hat{n}$  ( $+z$ ) direction. Then the reflected and transmitted fields can be decomposed as

$$[E^r] = [s_{11}][E^i] + [s_{12}][A^+] \quad (\text{A.1})$$

and

$$[E^t] = [s_{12}][P][A^-] \quad (\text{A.2})$$

where  $[E^i]$  is the incident field vector and  $[P]$  is the diagonal matrix accounting for the propagation phase delay of the modes over the path length  $d$ .

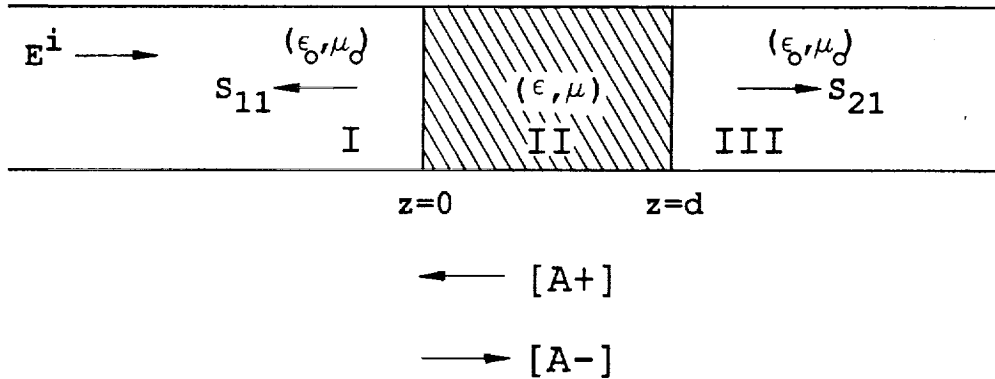


Figure A.1: Waveguide regions for the two-port approach.

The vectors  $[A^+]$  and  $[A^-]$  can be expressed as

$$[A^+] = [P][s_{22}][P][A^-] \quad (\text{A.3})$$



and

$$[A^-] = [s_{21}][E^i] + [s_{22}][A^+]. \quad (\text{A.4})$$

Inserting Eq. (A.3) in (A.4) gives

$$[A^-] = [s_{21}][E^i] + [s_{22}][P][s_{22}][P][A^-]. \quad (\text{A.5})$$

Rearranging Eq. (A.5) leads to

$$[A^-] = (I - [s_{22}][P][s_{22}][P])^{-1} [s_{21}][E^i]. \quad (\text{A.6})$$

Substituting Eq. (A.6) back into (A.3) gives

$$[A^+] = [P][s_{22}][P](I - [s_{22}][P][s_{22}][P])^{-1} [s_{21}][E^i]. \quad (\text{A.7})$$

Inserting Eq. (A.7) into (A.1) gives the equation for the reflected field and is given by

$$[E^r] = \{[s_{11}] + [s_{12}][P][s_{22}][P](I - [s_{22}][P][s_{22}][P])^{-1} [s_{21}]\} [E^i] \quad (\text{A.8})$$

and inserting Eq. (A.6) into Eq. (A.2), the expression for the transmitted field is

$$[E^t] = [s_{12}][P](I - [s_{22}][P][s_{22}][P])^{-1} [s_{21}][E^i]. \quad (\text{A.9})$$

## II Single-Port Formulation

For the single-port method where a short is placed a distance  $\ell$  from the end of the dielectric material, the self-consistent procedure is used again

to determine the reflected field from the scattering matrices. Referring to Figure A.2, let the vectors  $[A_1^+]$  and  $[A_1^-]$  denote the amplitudes of the modes of Region II at  $z=0$  traveling in the  $+\hat{n}$  and  $-\hat{n}$  directions, respectively, and let  $[A_2^+]$  and  $[A_2^-]$  represent the amplitudes of the modes of Region III at  $z=d$  traveling in the  $+\hat{n}$  and  $-\hat{n}$  directions. Then the reflected field can be expressed as

$$[E^r] = [s_{11}][E^i] + [s_{12}][A_1^+] \quad (\text{A.10})$$

where

$$[A_1^+] = [P_1][s_{22}][P_1][A_1^-] + [P_1][s_{21}][A_2^+], \quad (\text{A.11})$$

$$[A_1^-] = [s_{21}][E^i] + [s_{22}][A_1^+], \quad (\text{A.12})$$

$$[A_2^+] = [P_2][s_{\Gamma}][P_2][A_2^-] \text{ and} \quad (\text{A.13})$$

$$[A_2^-] = [s_{12}][P_1][A_1^-] + [s_{11}][A_2^+] \quad (\text{A.14})$$

where  $[E^i]$  is the incident field vector,  $[s_{\Gamma}] = -I$  is the scattering matrix for the shorted end,  $[P_1]$  is the diagonal matrix accounting for the propagation phase delay of the modes over the path length  $d$  and  $[P_2]$  is the diagonal propagation matrix over the path length  $\ell$ .

Inserting Eq. (A.13) into Eq. (A.14) and rearranging gives

$$[A_2^-] = (I - [s_{11}][P_2][s_{\Gamma}][P_2])^{-1} [s_{12}][P_1][A_1^-]. \quad (\text{A.15})$$

Substituting Eq. (A.15) back into (A.13)

$$[A_2^+] = [P_2][s_{\Gamma}][P_2](I - [s_{11}][P_2][s_{\Gamma}][P_2])^{-1} [s_{12}][P_1][A_1^-]. \quad (\text{A.16})$$

Putting Eq. (A.16) in (A.11)

$$[A_1^+] = \{[P_1][s_{22}][P_1]$$

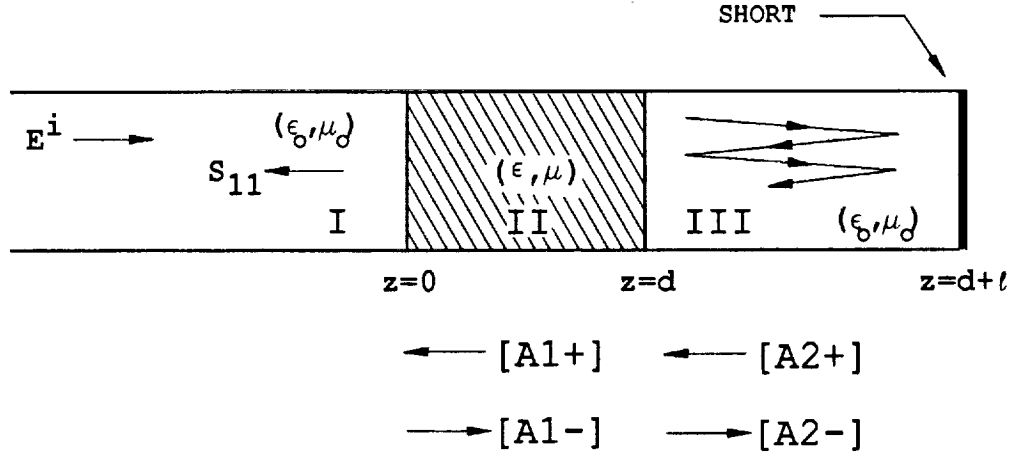


Figure A.2: Waveguide regions for the one-port approach.

$$\begin{aligned}
 & + [P_1][s_{21}][P_2][s_\Gamma][P_2] (I - [s_{11}][P_2][s_\Gamma][P_2])^{-1} [s_{12}][P_1] \} [A_1^-] \\
 & = [M][A_1^-] \tag{A.17}
 \end{aligned}$$

where

$$\begin{aligned}
 [M] & = [P_1] \{ [s_{22}] + [s_{21}][P_2][s_\Gamma][P_2] \\
 & \quad \cdot (I - [s_{11}][P_2][s_\Gamma][P_2])^{-1} [s_{12}] \} [P_1]. \tag{A.18}
 \end{aligned}$$

Inserting Eq. (A.17) into (A.12) and rearranging leads to

$$[A_1^-] = \{ I - [s_{22}][M] \}^{-1} [s_{21}][E^i]. \tag{A.19}$$

Substituting Eq. (A.19) back into Eq. (A.17) gives

$$[A_1^+] = [M] \{ I - [s_{22}][M] \}^{-1} [s_{21}][E^i]. \tag{A.20}$$

Finally using Eq. (A.20) in (A.10) and the fact that  $[s_\Gamma] = -I$ , the reflected field is

$$[E^r] = \{[s_{11}] + [s_{12}][M']\{I - [s_{22}][M']\}^{-1}[s_{21}]\}[E^i]. \quad (\text{A.21})$$

where

$$[M'] = [P_1] \{ [s_{22}] - [s_{21}][P_2][P_2] \\ \cdot (I + [s_{11}][P_2][P_2])^{-1} [s_{12}] \} [P_1]. \quad (\text{A.22})$$

## Appendix B

# Scattering Matrix Formulation for Geometry A

This section deals with attaining the elements of the scattering matrices which are to be used in the self-consistent procedure shown in the previous appendix for Geometry A.

First the scattered fields are defined below for Regions I ( $z < 0$ ) and II ( $z > 0$ ) where the scattered fields denoted by a superscript  $s$  are propagating or attenuating in the  $-z$  direction for Region I and propagating or attenuating in the  $+z$  direction for Region II.

Region I

$$E_y^{s,I} = \sum_{n=1}^{\infty} a_n \Phi_n e^{\Gamma_n z} \quad (\text{B.1})$$

and

$$H_x^{s,I} = \sum_{n=1}^{\infty} a_n Y_n \Phi_n e^{\Gamma_n z} \quad (\text{B.2})$$

where

$$\Phi_n = \sqrt{\frac{2}{a}} \sin \frac{n\pi}{a} x, \quad (\text{B.3})$$

$$\Gamma_n^2 = \left(\frac{n\pi}{a}\right)^2 - k_o^2 \quad \text{and} \quad (B.4)$$

$$Y_n = \frac{\Gamma_n}{jZ_o k_o}. \quad (B.5)$$

Region II

$$E_y^{s,II} = \sum_{n=1}^{\infty} b_n \Psi_n e^{-\gamma_n z} \quad (B.6)$$

and

$$H_x^{s,II} = - \sum_{n=1}^{\infty} b_n Y_{in} \Psi_n e^{-\gamma_n z} \quad (B.7)$$

where

$$\begin{aligned} \Psi_n &= C \sin k_{x_{1n}} x && \text{for } 0 \leq x \leq t, \\ \Psi_n &= C \frac{\sin k_{x_{1n}} t}{\sin k_{x_{0n}}(a-t)} \sin k_{x_{0n}}(a-x) && \text{for } t \leq x \leq a, \\ \gamma_n^2 &= k_{x_{1n}}^2 - k_o^2 \epsilon_r \mu_r = k_{x_{0n}}^2 - k_o^2, && (B.8) \\ Y_{1n} &= \frac{\gamma_n}{jZ_o k_o \mu_r} && \text{for } 0 \leq x \leq t, \\ Y_{0n} &= \frac{\gamma_n}{jZ_o k_o} && \text{for } t \leq x \leq a \end{aligned}$$

and  $C$  is a normalization constant. The constants  $k_{x_{1n}}$  and  $k_{x_{0n}}$  satisfy the following transcendental equation and are found using an iterative Newton-Raphson technique.

$$-k_{x_{1n}} \cos k_{x_{1n}} t \sin k_{x_{0n}}(a-t) = \mu_r k_{x_{0n}} \sin k_{x_{1n}} t \cos k_{x_{0n}}(a-t) \quad (B.9)$$

To get the first column of the  $s_{11}$  and  $s_{21}$  scattering matrices, it is assumed that the  $TE_{10}$  mode in Region I is the excitation mode propagating in the  $+z$  direction and incident on the material junction ( $z=0$ ). The excitation field quantities of Region I denoted by the superscript  $i$  are given by

$$E_y^i = \Phi_1 e^{-\Gamma_1 z} \quad (\text{B.10})$$

and

$$H_z^i = -Y_1 \Phi_1 e^{-\Gamma_1 z}. \quad (\text{B.11})$$

Matching the total tangential E and H fields (incident+scattered) at  $z = 0$  gives

$$(1 + a_1)\Phi_1 + \sum_{n=2}^{\infty} a_n \Phi_n = \sum_{m=1}^{\infty} b_m \Psi_m \quad (\text{B.12})$$

and

$$-(1 - a_1)Y_1 \Phi_1 + \sum_{n=2}^{\infty} a_n Y_n \Phi_n = - \sum_{m=1}^{\infty} b_m Y_{im} \Psi_m. \quad (\text{B.13})$$

Multiplying the above equations by the test functions  $\Phi_q$  ( $q = 1, 2, 3, \dots$ ), integrating from  $x=0$  to  $x=a$ , keeping the first N terms of the series and rearranging gives

$$\delta_{q1} = \sum_{n=1}^N (-a_n \delta_{qn} + b_n P_{qn}) \quad (\text{B.14})$$

and

$$Y_1 \delta_{q1} = \sum_{n=1}^N (a_n Y_n \delta_{qn} + b_n Y_{0n} Q_{qn}) \quad (\text{B.15})$$

where

$$\delta_{qn} = \begin{cases} 1 & \text{for } q = n \\ 0 & \text{for } q \neq n \end{cases}, \quad (\text{B.16})$$

$$P_{qn} = \int_0^a \Phi_q \Psi_n dx \quad \text{and} \quad (\text{B.17})$$

$$Q_{qn} = \frac{1}{\mu_r} \int_0^t \Phi_q \Psi_n dx + \int_t^a \Phi_q \Psi_n dx. \quad (\text{B.18})$$

In matrix form Eqs. (B.14) and (B.15) are

$$[X][S] = [E] \quad (B.19)$$

where the matrices X,S,and E are illustrated in Figure B.1.

$$[X] = \begin{bmatrix} -1 & 0 & 0 & \cdots & 0 & P_{11} & P_{12} & \cdots & P_{1N} \\ 0 & -1 & 0 & \cdots & & P_{21} & P_{22} & \cdots & P_{2N} \\ \vdots & & & & & \vdots & \vdots & & \vdots \\ 0 & \cdots & 0 & -1 & & P_{N1} & P_{N2} & \cdots & P_{NN} \\ \hline Y_1 & 0 & 0 & \cdots & 0 & Y_{01}Q_{11} & Y_{02}Q_{12} & \cdots & Y_{0N}Q_{1N} \\ 0 & Y_2 & 0 & \cdots & 0 & Y_{01}Q_{21} & Y_{02}Q_{22} & \cdots & Y_{0N}Q_{2N} \\ \vdots & & & & & \vdots & \vdots & & \vdots \\ 0 & \cdots & 0 & Y_N & & Y_{01}Q_{N1} & Y_{02}Q_{N2} & \cdots & Y_{0N}Q_{NN} \end{bmatrix}$$
  

$$[S] = \begin{bmatrix} a_1 \\ a_2 \\ \vdots \\ a_N \\ \hline b_1 \\ b_2 \\ \vdots \\ b_N \end{bmatrix} \left. \begin{array}{l} \text{1st COLUMN} \\ \text{OF } s_{11} \text{ MATRIX} \\ \hline \text{1st COLUMN} \\ \text{OF } s_{21} \text{ MATRIX} \end{array} \right\}$$
  

$$[E] = \begin{bmatrix} 1 \\ 0 \\ \vdots \\ 0 \\ \hline Y_1 \\ 0 \\ \vdots \\ 0 \end{bmatrix} \left. \begin{array}{l} \text{1st COLUMN} \\ \text{OF EXCITATION} \\ \text{MATRIX} \end{array} \right\}$$

Figure B.1: Matrix solution for the first column of the  $s_{11}$  and  $s_{21}$  scattering matrices. Geometry A.

To get the  $k^{th}$  ( $k = 2, 3, \dots, N$ ) columns of the  $s_{11}$  and  $s_{21}$  scattering matrices, the incident fields of Region I are

$$E_y^i = \Phi_k e^{-\Gamma_k z} \quad (B.20)$$

and



$$H_x^i = -Y_k \Phi_k e^{-\Gamma_k z}. \quad (\text{B.21})$$

Then the same procedure shown above is used.

To get the  $k^{\text{th}}$  columns of the  $s_{22}$  and  $s_{12}$  scattering matrices, the incident field now propagates (or attenuates) in the  $-z$  direction in Region II and one uses the following incident field expressions for Region II:

$$E_y^i = \Psi_k e^{\gamma_k z} \quad (\text{B.22})$$

and

$$H_x^i = Y_{ik} \Psi_k e^{\gamma_k z}. \quad (\text{B.23})$$

The entire matrix structure is illustrated in Figure B.2 where the X matrix in Figure B.2 has been partitioned into four parts.

$$\begin{bmatrix} [s_{11}] & [s_{12}] \\ \hline [s_{21}] & [s_{22}] \end{bmatrix} = \begin{bmatrix} [x_{11}] & [x_{12}] \\ \hline [x_{21}] & [x_{22}] \end{bmatrix}^{-1} \begin{bmatrix} [-x_{11}] & [-x_{12}] \\ \hline [x_{21}] & [x_{22}] \end{bmatrix}$$

Figure B.2: Complete matrix solution for all four scattering matrices. Geometry A.

# Appendix C

## Scattering Matrix Formulation for Geometry B

This appendix shows how the elements of the scattering matrices needed for the self-consistent procedure are attained for Geometry B.

First the scattered fields are defined below for Regions I and II where the scattered fields denoted by a superscript  $s$  are propagating or attenuating in the  $-z$  direction for Region I and propagating or attenuating in the  $+z$  direction for Region II.

Region I

$$E_y^{s,I} = \sum_{n=0}^{\infty} a_n^M A_n Z_n^M \Phi_n^I e^{\Gamma_n z}, \quad (\text{C.1})$$

$$E_x^{s,I} = \sum_{n=1}^{\infty} (a_n^M B_n + a_n^E C_n Z_n^E) \Phi_n^I e^{\Gamma_n z}, \quad (\text{C.2})$$

$$H_x^{s,I} = a_0^M A_0 \Phi_0^I e^{\Gamma_0 z} + \sum_{n=1}^{\infty} (a_n^M A_n + a_n^E B_n) \Phi_n^I e^{\Gamma_n z}, \quad (\text{C.3})$$

$$H_y^{s,I} = - \sum_{n=1}^{\infty} a_n^E C_n \Phi_n^I e^{\Gamma_n z} \quad (\text{C.4})$$

where

$$\Phi_n^I = \begin{cases} \sqrt{\frac{1}{b}} \sin \frac{\pi x}{a} & \text{for } n = 0 \\ \sqrt{\frac{2}{b}} \sin \frac{\pi x}{a} \cos \frac{n\pi y}{b} & \text{for } n = 1, 2, \dots \end{cases}, \quad (\text{C.5})$$

$$\Phi_n^{II} = \sqrt{\frac{2}{b}} \cos \frac{\pi x}{a} \sin \frac{n\pi y}{b}, \quad (\text{C.6})$$

$$\Gamma_n^2 = \left(\frac{n\pi}{b}\right)^2 - k_o^2 + \left(\frac{\pi}{a}\right)^2, \quad (\text{C.7})$$

$$Z_n^M = \frac{j \left[ k_o^2 - \left(\frac{n\pi}{b}\right)^2 \right]}{\omega \epsilon_0 \Gamma_n}, \quad (\text{C.8})$$

$$Z_n^E = \frac{\omega \mu_0 \Gamma_n}{j \left[ k_o^2 - \left(\frac{n\pi}{b}\right)^2 \right]}, \quad (\text{C.9})$$

$$A_n = j\omega \epsilon_0 \Gamma_n, \quad (\text{C.10})$$

$$B_n = \frac{n\pi^2}{ab} \quad \text{and} \quad (\text{C.11})$$

$$C_n = \left(\frac{\pi}{a}\right)^2 - \Gamma_n^2. \quad (\text{C.12})$$

Region II

$$E_y^{s,II} = \sum_{n=0}^{\infty} b_n^M A_n^M Z_n^{Mi} \Psi_n^{IM} e^{-\gamma_n^M z}, \quad (\text{C.13})$$

$$E_x^{s,II} = \sum_{n=1}^{\infty} (b_n^M B_n^M \Psi_n^{IM} e^{-\gamma_n^M z} + b_n^E C_n^E Z_n^{E1} \Psi_n^{IE} e^{-\gamma_n^E z}), \quad (\text{C.14})$$

$$H_x^{s,II} = -b_0^M A_0^M \Psi_0^{IM} e^{-\gamma_0^M z} - \sum_{n=1}^{\infty} (b_n^M A_n^M \Psi_n^{IM} e^{-\gamma_n^M z} + b_n^E B_n^E \Psi_n^{IE} e^{-\gamma_n^E z}), \quad (\text{C.15})$$

$$H_y^{s,II} = \sum_{n=1}^{\infty} b_n^E C_n^E \frac{\mu_1}{\mu_i} \Psi_n^{IE} e^{-\gamma_n^E z} \quad (\text{C.16})$$

where

$$i = \begin{cases} 1 & \text{for } 0 \leq y \leq t \\ 0 & \text{for } t \leq y \leq b \end{cases}, \quad (\text{C.17})$$

$$\Psi_n^{I\dagger} = \sin \frac{\pi x}{a} \begin{cases} \cos k_{y_{1n}}^\dagger y & \text{for } 0 \leq y \leq t \\ \frac{\cos k_{y_{1n}}^\dagger t}{\cos k_{y_{0n}}^\dagger (b-t)} \cos k_{y_{0n}}^\dagger (b-y) & \text{for } t \leq y \leq b \end{cases}, \quad (\text{C.18})$$

$$\Psi_n^{II\dagger} = \cos \frac{\pi x}{a} \begin{cases} \sin k_{y_{1n}}^\dagger y & \text{for } 0 \leq y \leq t \\ \frac{\sin k_{y_{1n}}^\dagger t}{\sin k_{y_{0n}}^\dagger (b-t)} \sin k_{y_{0n}}^\dagger (b-y) & \text{for } t \leq y \leq b \end{cases}, \quad (\text{C.19})$$

$$\gamma_n^{\dagger 2} = k_{y_{in}}^{\dagger 2} - k_i^2 + \left(\frac{\pi}{a}\right)^2, \quad (\text{C.20})$$

$$Z_n^{Mi} = \frac{j \left[ \left( \frac{\pi}{a} \right)^2 - \gamma_n^{M2} \right]}{\omega \epsilon_i \gamma_n^M}, \quad (\text{C.21})$$

$$Z_n^{Ei} = \frac{\omega \mu_i \gamma_n^E}{j \left[ \left( \frac{\pi}{a} \right)^2 - \gamma_n^{E2} \right]}, \quad (\text{C.22})$$

$$A_n^M = j \omega \epsilon_1 \gamma_n^M, \quad (\text{C.23})$$

$$B_n^\dagger = \frac{\pi k_{y1n}^\dagger}{a} \quad \text{and} \quad (\text{C.24})$$

$$C_n^E = \left( \frac{\pi}{a} \right)^2 - \gamma_n^{E2}. \quad (\text{C.25})$$

The constants  $k_{y1n}^M$  and  $k_{y0n}^M$  satisfy the following transcendental equation and are found using an iterative Newton-Raphson technique.

$$-k_{y1n}^M \sin k_{y1n}^M t \cos k_{y0n}^M (b-t) = \epsilon_r k_{y0n}^M \cos k_{y1n}^M t \sin k_{y0n}^M (b-t). \quad (\text{C.26})$$

The constants  $k_{y1n}^E$  and  $k_{y0n}^E$  satisfy the following:

$$-k_{y1n}^E \cos k_{y1n}^E t \sin k_{y0n}^E (b-t) = \mu_r k_{y0n}^E \sin k_{y1n}^E t \cos k_{y0n}^E (b-t). \quad (\text{C.27})$$

To determine the first column elements of the  $s_{11}$  and  $s_{21}$  matrices, the  $\text{TE}_{10}$  mode (or  $\text{TM}_{y10}$ ) in Region I is assumed to be the excitation mode propagating in the  $+z$  direction and incident on the material junction ( $z=0$ ). The excitation quantities exist only in Region I and are

$$E_y^i = A_0 Z_0^M \Phi_0^I e^{-\Gamma_0 z}, \quad (\text{C.28})$$

$$E_x^i = 0, \quad (\text{C.29})$$

$$H_x^i = -A_0 \Phi_0^I e^{-\Gamma_0 z} \quad (\text{C.30})$$

and

$$H_y^i = 0. \quad (C.31)$$

Matching the total tangential E and H fields (incident+scattered) at  $z=0$  gives

$$(1 + a_0^M)A_0Z_0^M\Phi_0^I + \sum_{n=1}^{\infty} a_n^M A_n Z_n^M \Phi_n^I = \sum_{m=0}^{\infty} b_m^M A_m^M Z_m^{M1} \Psi_m^{IM}, \quad (C.32)$$

$$\begin{aligned} \sum_{n=1}^{\infty} (a_n^M B_n + a_n^E C_n Z_n^E) \Phi_n^H &= \sum_{m=1}^{\infty} (b_m^M B_m^M \Psi_m^{HM} \\ &+ b_m^E C_m^E Z_m^{E1} \Psi_m^{HE}), \end{aligned} \quad (C.33)$$

$$\begin{aligned} -(1 - a_0^M)A_0\Phi_0^I + \sum_{n=1}^{\infty} (a_n^M A_n + a_n^E B_n) \Phi_n^I &= \\ -b_0^M A_0^M \Psi_0^{IM} - \sum_{m=1}^{\infty} (b_m^M A_m^M \Psi_m^{IM} + b_m^E B_m^E \Psi_m^{IE}) & \end{aligned} \quad (C.34)$$

and

$$-\sum_{n=1}^{\infty} a_n^E C_n \Phi_n^H = \sum_{m=1}^{\infty} b_m^E C_m^E \frac{\mu_1}{\mu_i} \Psi_m^{HE}. \quad (C.35)$$

Multiplying Eqs. (C.32) and (C.34) by the test functions  $\Phi_q^I$  ( $q = 0, 1, \dots, N$ ), multiplying Eqs. (C.33) and (C.35) by the test functions  $\Phi_{q'}^H$  ( $q' = 1, 2, \dots, N$ ), integrating from  $y=0$  to  $y=b$ , keeping the first  $N$  terms of the series and some rearranging gives

$$A_0 Z_0^M \delta_{q0} = \sum_{n=0}^{\infty} (-a_n^M A_n Z_n^M \delta_{qn} + b_n^M A_n^M Z_n^{M1} Q_{qn}^{IM}), \quad (C.36)$$

$$\begin{aligned} 0 &= \sum_{n=1}^{\infty} \left\{ -(a_n^M B_n + a_n^E C_n Z_n^E) \delta_{q'n} + b_n^M B_n^M P_{q'n}^{HM} \right. \\ &\quad \left. + b_n^E C_n^E Z_n^{E1} P_{q'n}^{HE} \right\}, \end{aligned} \quad (C.37)$$

$$\begin{aligned}
A_0 \delta_{q_0} = & \\
& a_0^M A_0 \delta_{q_0} + b_0^M A_0^M P_{q_0}^{IM} \\
& + \sum_{n=1}^{\infty} \left\{ (a_n^M A_n + a_n^E B_n) \delta_{qn} + b_n^M A_n^M P_{qn}^{IM} + b_n^E B_n^E P_{qn}^{IE} \right\} \quad (C.38)
\end{aligned}$$

and

$$0 = \sum_{n=1}^{\infty} (a_n^E C_n \delta_{q'n} + b_n^E C_n^E Q_{q'n}^{IE}) \quad (C.39)$$

where

$$\delta_{qn} = \begin{cases} 1 & \text{for } q = n \\ 0 & \text{for } q \neq n \end{cases}, \quad (C.40)$$

$$P_{qn}^{I\dagger} = \int_0^b \Phi_q^I \Psi_n^{I\dagger} dy, \quad (C.41)$$

$$P_{qn}^{II\dagger} = \int_0^b \Phi_q^{II} \Psi_n^{II\dagger} dy, \quad (C.42)$$

$$Q_{qn}^{IM} = \int_0^t \Phi_q^I \Psi_n^{IM} dy + \epsilon_r \int_t^b \Phi_q^I \Psi_n^{IM} dy \quad \text{and} \quad (C.43)$$

$$Q_{qn}^{IE} = \int_0^t \Phi_q^{II} \Psi_n^{IE} dy + \mu_r \int_t^b \Phi_q^{II} \Psi_n^{IE} dy. \quad (C.44)$$

Eqs. (C.36),(C.37),(C.38) and (C.39) are given in matrix form as

$$[X][S] = [E] \quad (C.45)$$

where the matrices X, S, and E are illustrated in Figure C.1.

To get the  $k^{th}$  ( $k = 1, 2, \dots, N$ ) columns of the  $s_{11}$  and  $s_{21}$  scattering matrices, the incident fields used in Region I are

$$E_y^i = A_k Z_k^M \Phi_k^I e^{-\Gamma_k z}, \quad (C.46)$$

$$E_x^i = B_k \Phi_k^{II} e^{-\Gamma_k z}, \quad (C.47)$$

$$H_x^i = -A_k \Phi_k^I e^{-\Gamma_k z} \quad (\text{C.48})$$

and

$$H_y^i = 0. \quad (\text{C.49})$$

Then the same procedure shown above is used.

To get the  $k'^{th}$  ( $k' = k + N$ ) columns of the the  $s_{11}$  and  $s_{21}$  scattering matrices, the incident fields in Region I are

$$E_y^i = 0, \quad (\text{C.50})$$

$$E_x^i = C_{k'} Z_{k'}^E \Phi_{k'}^H e^{-\Gamma_{k'} z}, \quad (\text{C.51})$$

$$H_x^i = -B_{k'} \Phi_{k'}^I e^{-\Gamma_{k'} z} \quad (\text{C.52})$$

and

$$H_y^i = C_{k'} \Phi_{k'}^H e^{-\Gamma_{k'} z}. \quad (\text{C.53})$$

To get the  $k^{th}$  ( $k = 0, 1, \dots, N$ ) columns of the  $s_{22}$  and  $s_{12}$  scattering matrices, the incident field now propagates (or attenuates) in the  $-z$  direction in Region II, and one uses the following incident field expressions for Region II:

$$E_y^i = A_k^M Z_k^M \Psi_k^{IM} e^{\gamma_k^M z}, \quad (\text{C.54})$$

$$E_x^i = \begin{cases} B_k^M \Psi_k^{HM} e^{\gamma_k^M z} & \text{for } k \neq 0 \\ 0 & \text{for } k = 0 \end{cases}, \quad (\text{C.55})$$

$$H_x^i = A_k^M \Psi_k^{IM} e^{\gamma_k^M z} \quad (\text{C.56})$$

and

$$H_y^i = 0. \quad (\text{C.57})$$

To get the  $k'^{th}$  ( $k' = k + N, k = 1, 2, \dots, N$ ) columns of the the  $s_{11}$  and  $s_{21}$  scattering matrices, the incident fields in Region I are

$$E_y^i = 0, \quad (\text{C.58})$$

$$E_x^i = C_{k'}^E Z_{k'}^{E1} \Psi_{k'}^{IE} e^{\gamma_{k'}^E z}, \quad (\text{C.59})$$

and

$$H_x^i = B_{k'}^E \Psi_{k'}^{IE} e^{\gamma_{k'}^E z} \quad (\text{C.60})$$

and

$$H_y^i = -C_{k'}^E \frac{\mu_1}{\mu_i} \Psi_{k'}^{IE} e^{\gamma_{k'}^E z}. \quad (\text{C.61})$$

The entire matrix structure is illustrated in Figure C.2.



$$[X] = \begin{array}{|c|c|c|c|} \hline \begin{array}{c} -A_0 Z_0^M \\ \vdots \\ -A_N Z_N^M \end{array} & \begin{array}{c} \text{Hatched} \\ \text{Block} \end{array} & \begin{array}{c} A_0^M Z_0^{M1} Q_{00}^{IM} \\ A_0^M Z_0^{M1} Q_{10}^{IM} \\ \vdots \\ A_N^M Z_N^{M1} Q_{NN}^{IM} \end{array} & \begin{array}{c} \text{Hatched} \\ \text{Block} \end{array} \\ \hline \begin{array}{c} 0 \quad -B_1 \\ \vdots \\ 0 \quad -B_N \end{array} & \begin{array}{c} -C_1 Z_1^E \\ \vdots \\ -C_N Z_N^E \end{array} & \begin{array}{c} 0 \quad B_1^M P_{11}^{IIM} \\ B_1^M P_{21}^{IIM} \\ \vdots \\ 0 \quad B_N^M P_{NN}^{IIM} \end{array} & \begin{array}{c} C_1^E Z_1^{E1} P_{11}^{IIE} \\ C_1^E Z_1^{E1} P_{21}^{IIE} \\ \vdots \\ C_N^E Z_1^{E1} P_{NN}^{IIE} \end{array} \\ \hline A_0 & 0 \quad 0 & \begin{array}{c} A_0^M P_{00}^{IM} \\ A_0^M P_{10}^{IM} \\ \vdots \\ A_N^M P_{NN}^{IM} \end{array} & \begin{array}{c} 0 \quad 0 \\ B_1^E P_{11}^{IE} \\ \vdots \\ B_N^E P_{NN}^{IE} \end{array} \\ \hline \begin{array}{c} \text{Hatched} \\ \text{Block} \end{array} & C_1 & \begin{array}{c} \text{Hatched} \\ \text{Block} \end{array} & \begin{array}{c} C_1^E Q_{11}^{IIE} \\ C_1^E Q_{21}^{IIE} \\ \vdots \\ C_N^E Q_{NN}^{IIE} \end{array} \\ \hline \end{array}$$

$$[S] = \left[ \begin{array}{c} a_{00}^M \\ \vdots \\ a_{11}^M \\ \vdots \\ a_{NN}^M \\ \hline b_{00}^M \\ \vdots \\ b_{11}^M \\ \vdots \\ b_{NN}^M \end{array} \right] \left\{ \begin{array}{l} \text{1st COLUMN} \\ \text{OF } s_{11} \text{ MATRIX} \\ \hline \text{1st COLUMN} \\ \text{OF } s_{21} \text{ MATRIX} \end{array} \right.$$

$$[E] = \left[ \begin{array}{c} A_0 Z_0^M \\ 0 \\ \vdots \\ 0 \\ \hline 0 \\ A_0 \\ \vdots \\ 0 \\ \hline 0 \\ \vdots \\ 0 \end{array} \right] \left\{ \begin{array}{l} \text{1st COLUMN} \\ \text{OF EXCITATION} \\ \text{MATRIX} \end{array} \right.$$

Figure C.1: Matrix solution for the first column of the  $s_{11}$  and  $s_{21}$  scattering matrices. Geometry B.

$$\begin{bmatrix} [s_{11}] & [s_{12}] \\ [s_{21}] & [s_{22}] \end{bmatrix} = \begin{bmatrix} [x_{11}] & [x_{12}] & [x_{13}] & [x_{14}] \\ [x_{21}] & [x_{22}] & [x_{23}] & [x_{24}] \\ [x_{31}] & [x_{32}] & [x_{33}] & [x_{34}] \\ [x_{41}] & [x_{42}] & [x_{43}] & [x_{44}] \end{bmatrix}^{-1} \begin{bmatrix} [-x_{11}] & [-x_{12}] & [-x_{13}] & [-x_{14}] \\ [-x_{21}] & [-x_{22}] & [-x_{23}] & [-x_{24}] \\ [x_{31}] & [x_{32}] & [x_{33}] & [x_{34}] \\ [x_{41}] & [x_{42}] & [x_{43}] & [x_{44}] \end{bmatrix}$$

Figure C.2: Complete matrix solution for all four scattering matrices. Geometry B.

# Appendix D

## Determination of Gamma Constants

The calculation of the S parameters for a partially-filled waveguide requires finding a set of gamma (propagation) constants. For Geometry A the gamma constants  $\gamma_n$  ( $n = 1, 2, 3, \dots$ ) used in the series expansions for the S parameters satisfy the transcendental equation

$$k_{x_{1n}} \cos k_{x_{1n}} t \sin k_{x_{0n}}(a - t) + \mu_r k_{x_{0n}} \sin k_{x_{1n}} t \cos k_{x_{0n}}(a - t) = 0 \quad (\text{D.1})$$

where

$$\gamma_n^2 = k_{x_{1n}}^2 - k_o^2 \epsilon_r \mu_r = k_{x_{0n}}^2 - k_o^2. \quad (\text{D.2})$$

For Geometry B, the  $\text{TM}_y$  gamma constants  $\gamma_n^M$  ( $m = 0, 1, 2, \dots$ ) must satisfy

$$k_{y_{1m}}^M \sin k_{y_{1m}}^M t \cos k_{y_{0m}}^M (b - t) + \epsilon_r k_{y_{0m}}^M \cos k_{y_{1m}}^M t \sin k_{y_{0m}}^M (b - t) = 0 \quad (\text{D.3})$$

and the  $\text{TE}_y$  gammas  $\gamma_n^E$  ( $n = 1, 2, 3, \dots$ ) satisfy

$$k_{y_{1n}}^E \cos k_{y_{1n}}^E t \sin k_{y_{0n}}^E (b - t) + \mu_r k_{y_{0n}}^E \sin k_{y_{1n}}^E t \cos k_{y_{0n}}^E (b - t) = 0 \quad (\text{D.4})$$

where

$$\gamma_n^{\dagger 2} = k_{y_{in}}^{\dagger 2} - k_i^2 + \left(\frac{\pi}{a}\right)^2, \quad (\text{D.5})$$

$$i = \begin{cases} 1 & \text{for } 0 \leq y \leq t \\ 0 & \text{for } t \leq y \leq b \end{cases}. \quad (\text{D.6})$$

Each of the above transcendental equations contains an infinite number of roots. The method of obtaining the gamma constant for a particular index number  $n$  involves first finding the value which satisfies the above transcendental equations for the completely-filled (or empty) case. The exact gamma value  $\gamma_n^{\text{cf}}$  of a completely-filled guide for Geometry A and index  $n$  is given by

$$\gamma_n^{\text{cf}} = jk_0\sqrt{\epsilon_r\mu_r} \sqrt{1 - \frac{\lambda_0^2}{4\epsilon_r\mu_r} \left(\frac{n}{b}\right)^2}. \quad (\text{D.7})$$

The exact gamma value for Geometry B of a completely-filled guide is given by

$$\gamma_n^{\text{cf}} = jk_0\sqrt{\epsilon_r\mu_r} \sqrt{1 - \frac{\lambda_0^2}{4\epsilon_r\mu_r} \left[ \left(\frac{n}{a}\right)^2 + \left(\frac{1}{b}\right)^2 \right]}. \quad (\text{D.8})$$

Then the dimension  $t$  in Eqs. (D.1) through (D.4) is decreased from the completely-filled case by an increment  $\Delta t$ , and the initial gamma  $\gamma_n^{\text{cf}}$  calculated in Eq. (D.7) or Eq.(D.8) is used in the first iteration to find the gamma which satisfies the appropriate transcendental equation. This gamma value is then the initial value used in the next iteration where the current value of  $t$  in the transcendental equation is again decreased by  $\Delta t$ . This process is continued in increments of  $\Delta t$  until the desired dimension  $t$  is reached.

For each  $t$  used in the above procedure a Newton-Raphson iteration process is used to find the gamma constants which satisfy their transcendental equations.

Problems may occur in the search when  $\Delta t$  is not small enough. Also, finding a wrong gamma may occur when a gamma passes through zero in the complex plane during the iteration. A plot of how the gammas for different modal indices vary with  $t$  is given in Figure D.1 for Geometry A and Figures D.2 and D.3 for Geometry B. A plot for varying frequency is also given in Figure D.4 for Geometry A only.

The number of gamma constants actually needed to calculate the S parameters depends on the desired accuracy of the S parameters. Figures D.5 and D.6 illustrate how the S parameters vary with the number of gamma constants (modes) used in the calculations for Geometry A. Similarly results for Geometry B are presented in Figures D.7 and D.8 where a number  $N$  modes used refers to  $(N + 1)$   $TM_y$  modes and  $N$   $TE_y$  modes. The above figures used  $\epsilon_r = (4.0, -j.2)$  and  $\mu_r = (1.2, -j.12)$  in an X-band fixture. The typical number of modes used to generate the plots throughout this report was six for both geometries.

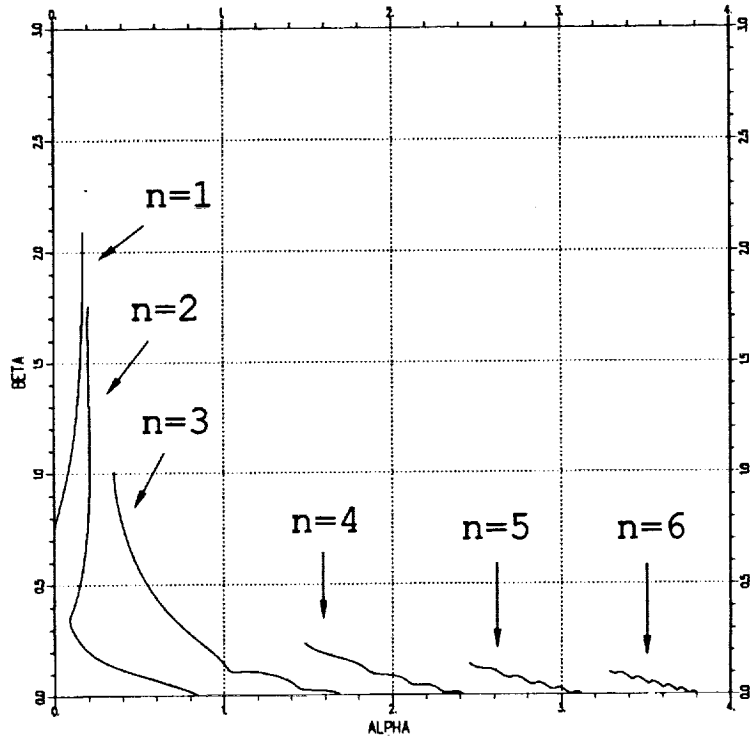


Figure D.1: Plot of alpha vs. beta from  $t = 0$  to  $t = a$  where  $\gamma = \alpha + j\beta$ . Geometry A in an X-band fixture (.4"x.9") with  $\epsilon_r = (4.0, -j.20)$ ,  $\mu_r = (1.2, -j.12)$ ,  $d = 0.3''$  and  $f = 10$  GHz.

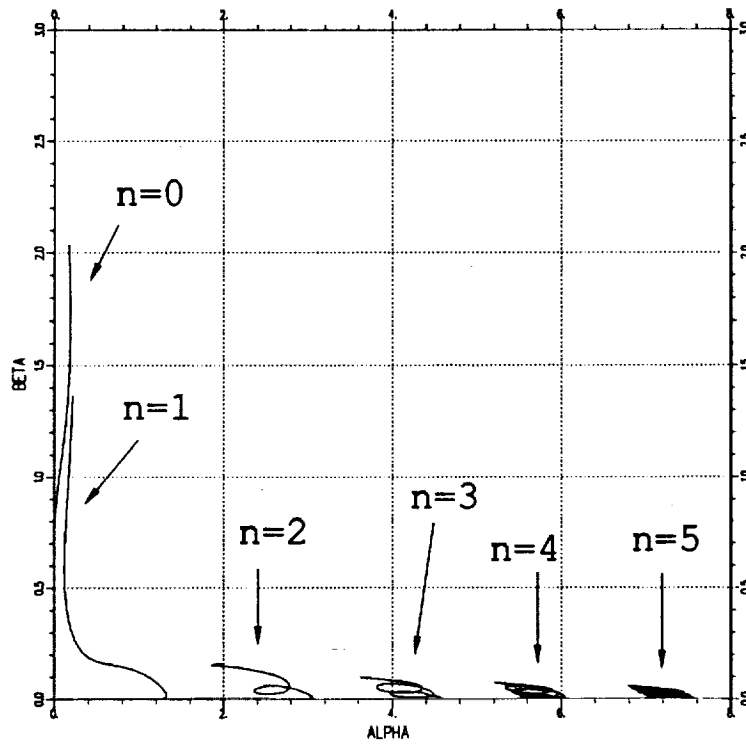


Figure D.2: Plot of alpha vs. beta for  $TM_y$  modes from  $t = 0$  to  $t = b$  where  $\gamma = \alpha + j\beta$ . Geometry B in an X-band fixture (.4"x.9") with  $\epsilon_r = (4.0, -j.20)$ ,  $\mu_r = (1.2, -j.12)$ ,  $d = 0.3''$  and  $f = 10$  GHz.

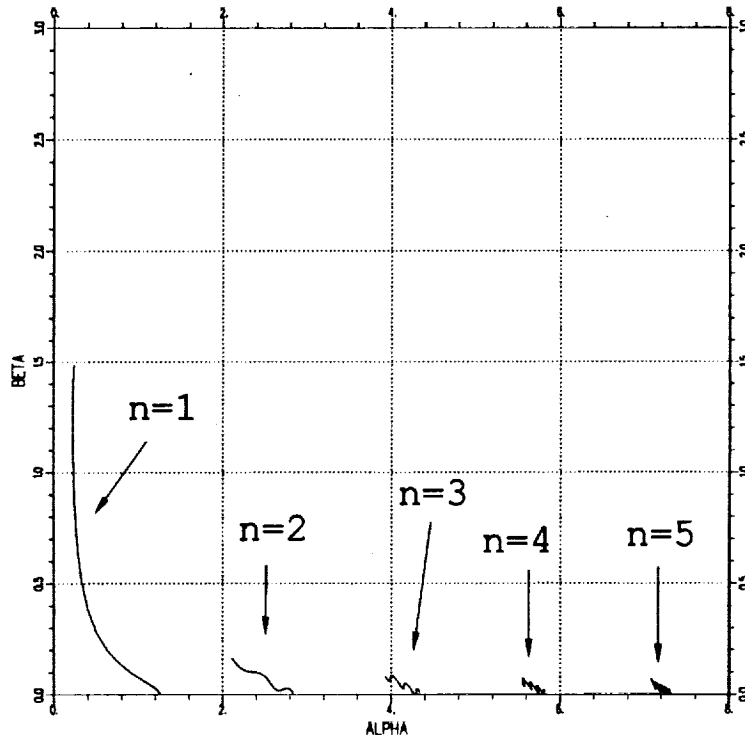


Figure D.3: Plot of alpha vs. beta for  $TE_y$  modes from  $t = 0$  to  $t = b$  where  $\gamma = \alpha + j\beta$ . Geometry B in an X-band fixture (.4"x.9") with  $\epsilon_r = (4.0, -j.20)$ ,  $\mu_r = (1.2, -j.12)$ ,  $d = 0.3''$  and  $f = 10$  GHz.



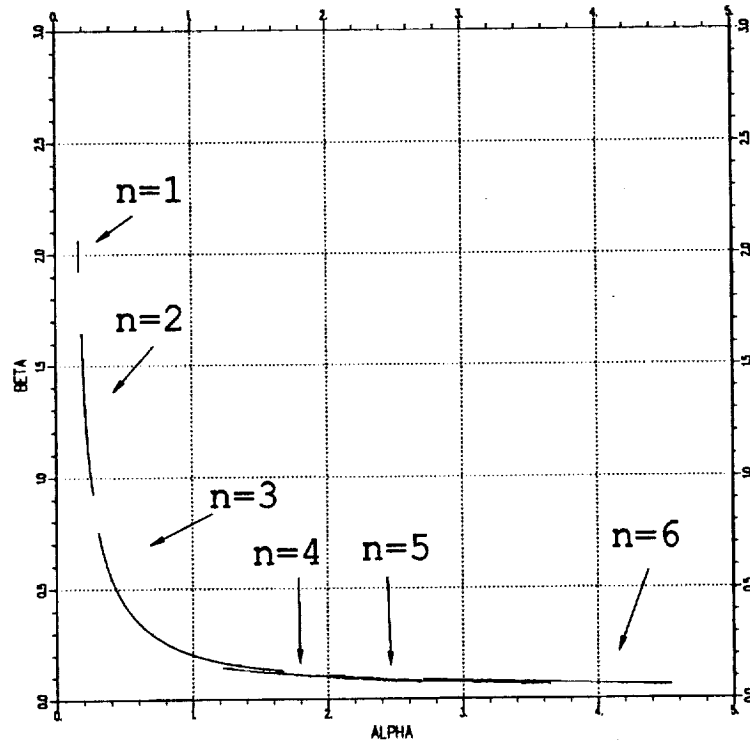


Figure D.4: Plot of alpha vs. beta from  $f = 8$  GHz to  $f = 12$  GHz where  $\gamma = \alpha + j\beta$ . Geometry A in an X-band fixture (.4"x.9") with  $\epsilon_r = (4.0, -j.20)$ ,  $\mu_r = (1.2, -j.12)$ ,  $d = 0.3''$  and  $t = 0.6''$ .

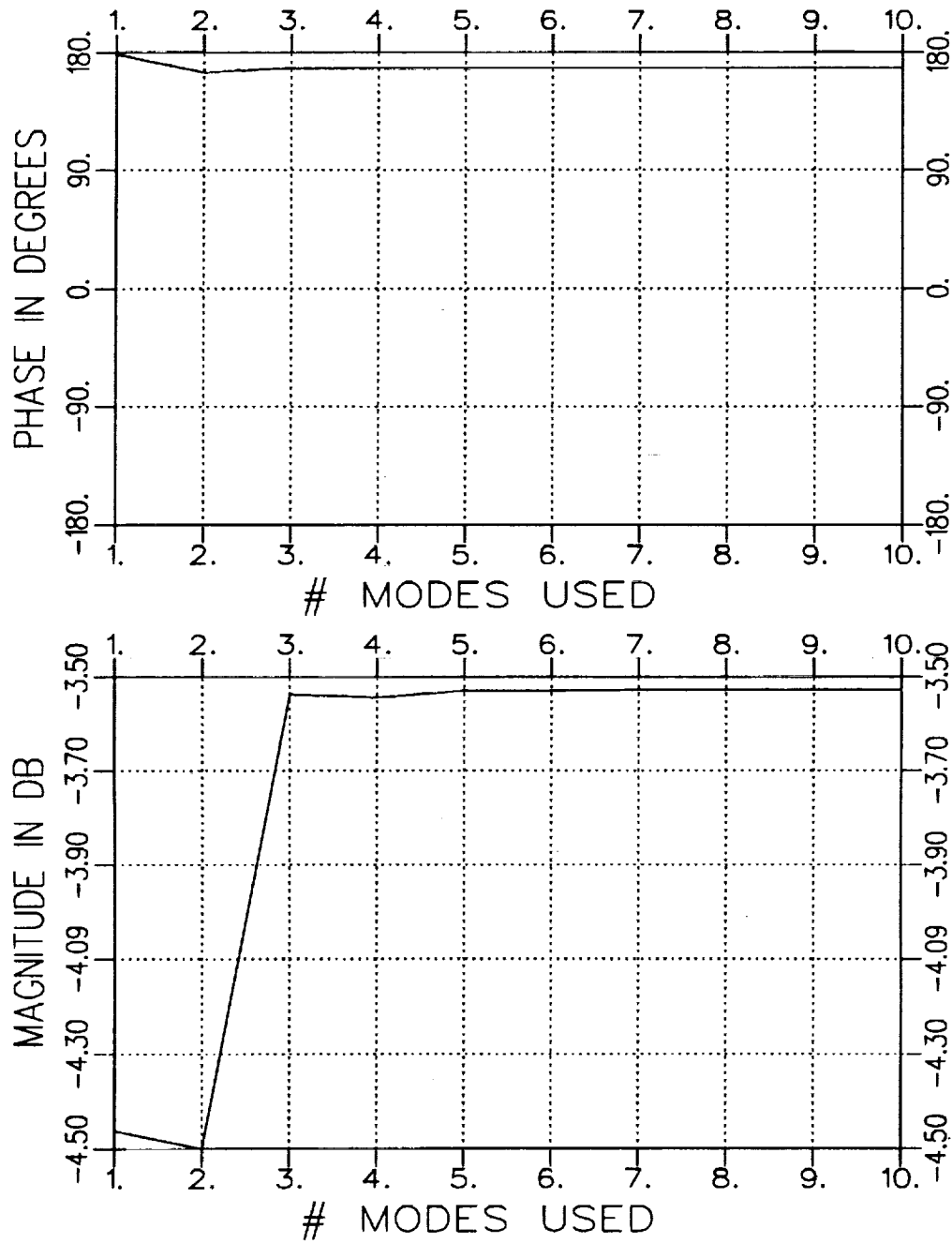


Figure D.5:  $S_{11}$  vs. number of modes used in calculations. Geometry A with  $t = .514''$ ,  $d = .3''$  and  $f = 10$  GHz.

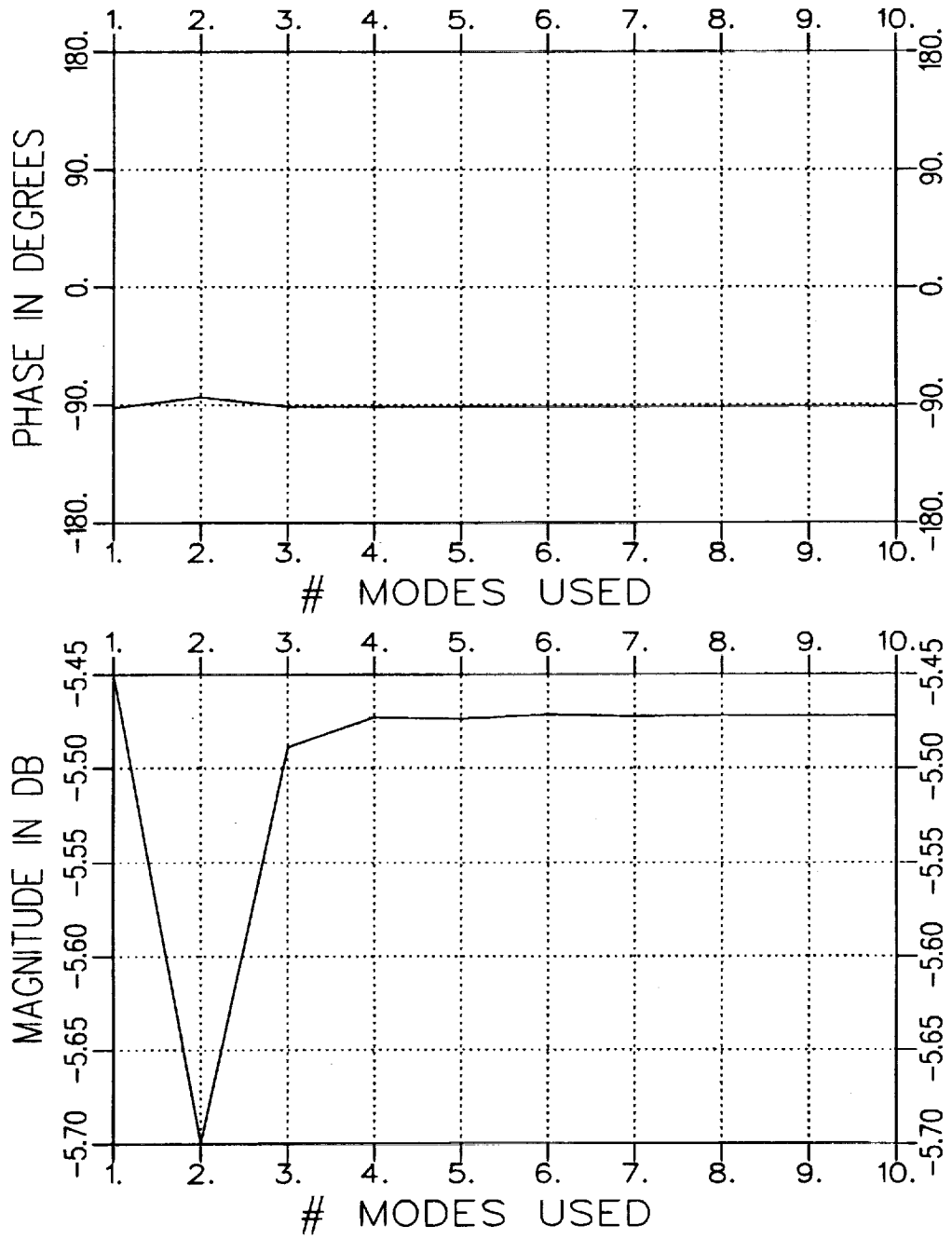


Figure D.6:  $S_{21}$  vs. number of modes used in calculations. Geometry A with  $t = .514''$ ,  $d = .3''$  and  $f = 10$  GHz.

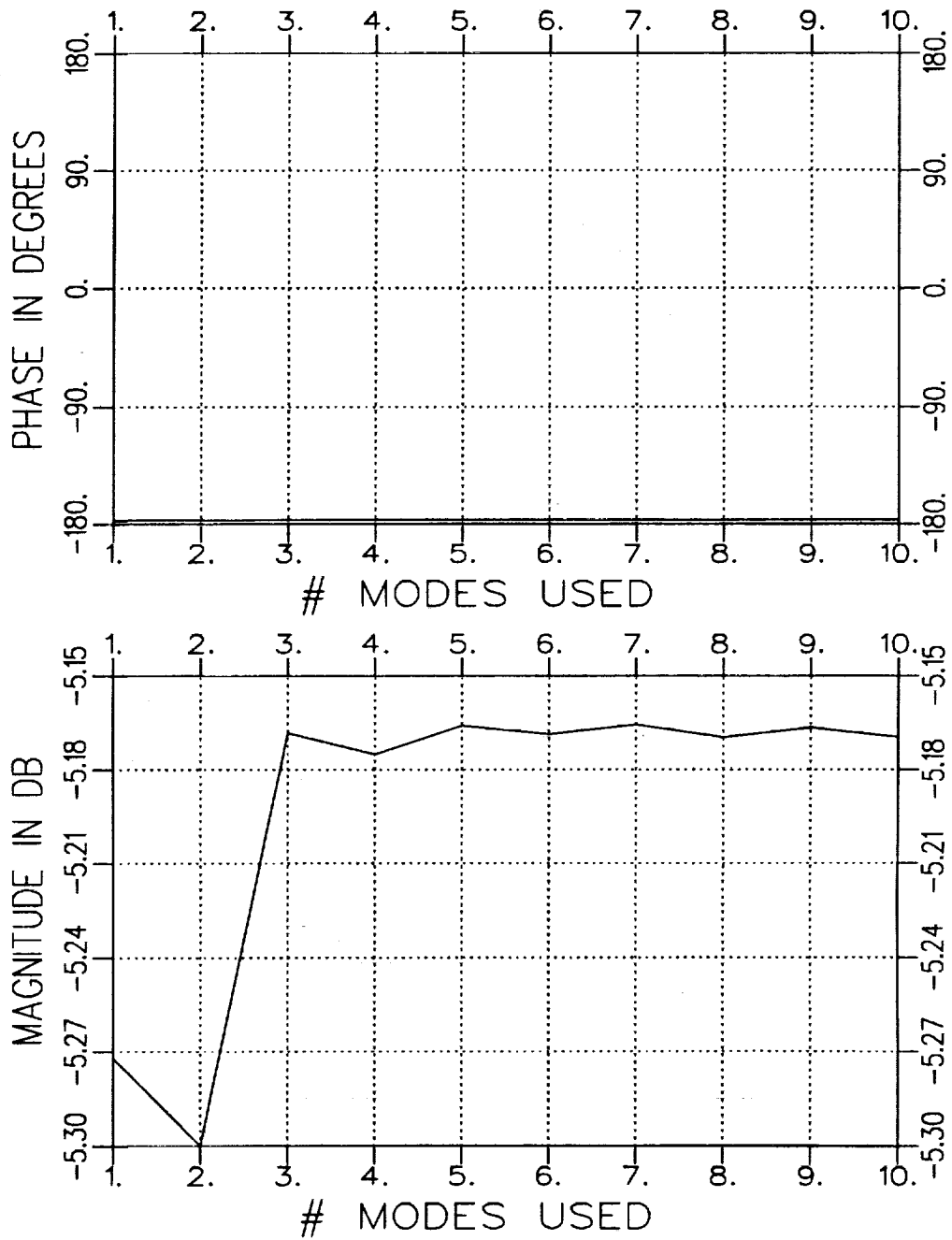


Figure D.7:  $S_{11}$  vs. number of modes used in calculations. Geometry B with  $t = .3''$ ,  $d = .3''$  and  $f = 10$  GHz.

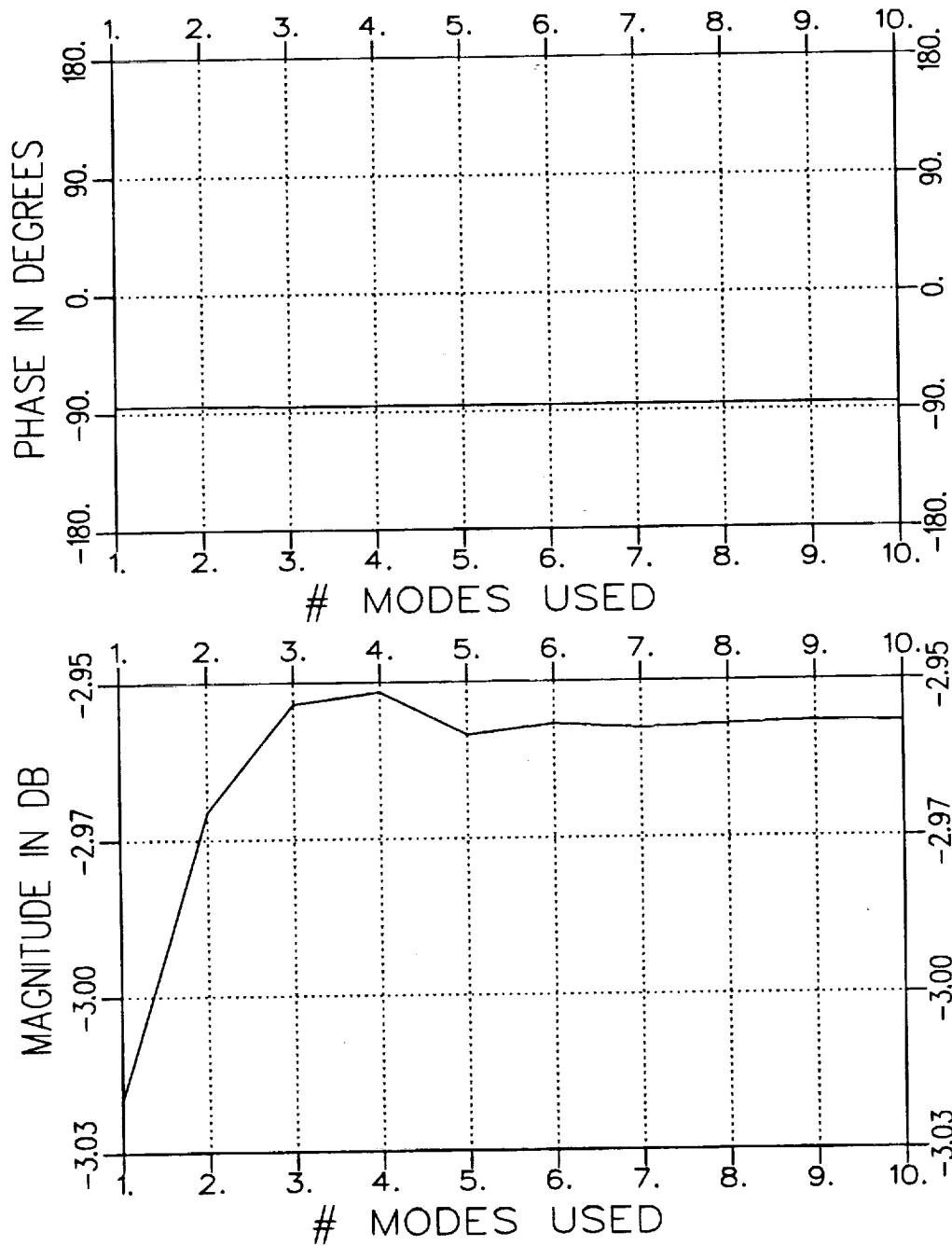


Figure D.8:  $S_{21}$  vs. number of modes used in calculations. Geometry B with  $t = .3''$ ,  $d = .3''$  and  $f = 10$  GHz.

# Bibliography

- [1] B.M. Kent, "An Automated Dual Horn-Reflector Microwave Absorber Measurement System," M.S. Thesis, The Ohio State University ElectroScience Laboratory, Department of Electrical Engineering, Columbus, Ohio, 1981.
- [2] Handbook of Microwave Measurements, edited by M. Wind and H. Rapaport, Polytechnic Institute of Brooklyn, Vol. 1, Section X, Appendix I, p. 29, 1955.
- [3] Technique of Microwave Measurements, edited by C.G. Montgomery, McGraw-Hill Book Co., New York, p. 576, 1947.
- [4] C.H. Krueger, "On the Inaccuracy of Determining Complex Dielectric Constant by the Coaxial Transmission Line Technique," M.S. Thesis, The Ohio State University, 1966.
- [5] R.F. Harrington, Time-Harmonic Electromagnetic Fields, McGraw-Hill Book Co., New York, pp. 158-163, 1961.
- [6] R.E. Collin and R.M. Vaillancourt, "Application of Rayleigh-Ritz Method to Dielectric Steps in Waveguides," *IRE Transaction on Microwave Theory and Techniques*, Vol. MTT-5, pp. 177-184, July 1957.
- [7] R.E. Collin, Theory of Guided Waves, McGraw-Hill Book Co., New York, Chapters 6 and 8, 1960.
- [8] HP Product Note 8510-3, "Measuring Dielectric Constant with the HP 8510 Network Analyzer," Hewlett-Packard Company.
- [9] J. Munk and A. Dominek, "Calibration of Automatic Network Analyzers," Report 723224-1, ElectroScience Laboratory, The Ohio State University, September 1990.

- [10] A. Altintas, P.H. Pathak and W.D. Burnside, "Electromagnetic Scattering from a Class of Open-Ended Waveguide Discontinuities," Report 716148-9, ElectroScience Laboratory, The Ohio State University, pp. 16-26, March 1986.
- [11] A.K. Dominek, L. Peters, Jr. and W.D. Burnside, "A Time Domain Technique for Mechanism Extraction," *IEEE Transactions on Antennas and Propagation*, Vol. AP-35, No. 3, March 1987.

